2012-09-20

Liquid Jet Impingement Experiments on Micro Rib and Cavity Patterned Superhydrophobic Surfaces in Both Cassie and Wenzel States

Michael G. Johnson
Brigham Young University - Provo

Liquid Jet Impingement Experiments on Micro-Rib and Cavity-Patterned Superhydrophobic Surfaces in Both Cassie and Wenzel States

Michael G. Johnson

A thesis submitted to the faculty of
Brigham Young University
in partial fulfillment of the requirements for the degree of

Master of Science

R. Daniel Maynes, Chair
Julie Crockett
Brent W. Webb

Department of Mechanical Engineering

Brigham Young University

September 2012

ABSTRACT

Liquid Jet Impingement Experiments on Micro-Rib and Cavity-Patterned Superhydrophobic Surfaces in Both Cassie and Wenzel States

Michael G. Johnson
Department of Mechanical Engineering
Master of Science

Experiments were performed to characterize hydraulic jumps that form due to liquid jet impingement on superhydrophobic surfaces with alternating micro-ribs and cavities. If the surface is unimmersed, a surface tension based transition into droplets occurs, so a known depth of water was imposed downstream from the hydraulic jump to ensure the existence of a hydraulic jump. The surfaces are characterized by the cavity fraction, which is defined as the width of a cavity divided by the combined width of a cavity and an adjoining rib. Four different surface designs were studied, with respective cavity fractions of 0 (smooth surface), 0.5, 0.8, and 0.93. Each surface was tested in its naturally hydrophilic state where water was allowed to flood the cavities, as well as with a hydrophobic coating which prevented water from entering the cavities and created a liquid-gas interface over much of the surface. The experimental data spans a Weber number range (based on the jet velocity and radius) of $3x10^2$ to $1.05x10^3$ and a corresponding Reynolds number range of $1.15x10^4$ to $2.14x10^4$. While smooth surfaces always result in circular transitions, for any rib and cavity patterned surface the flow exhibits a nearly elliptical transition from the thin film, where the major axis of the ellipse is parallel to the ribs, concomitant with greater slip in that direction. When the downstream depth is small and a superhydrophobic surface is used, the water is completely expelled from the surface, and the thin film breaks up into droplets due to surface tension interactions. When the downstream depth is large or the surface is hydrophilic a hydraulic jump exists. When the water depth downstream of the jump increases, the major and minor axis of the jump decreases due to an increase in hydrostatic force, following classical hydraulic jump behavior. The experimental results indicate that for a given cavity fraction and downstream depth, the radius of the jump increases with increasing Reynolds number. The jump radius perpendicular to the ribs is notably less than that for a smooth surface, and this radius decreases with increasing cavity fraction. When comparing flow over superhydrophobic (coated) surfaces to patterned, hydrophilic (uncoated) surfaces, a general increase is seen in the radial location of the hydraulic jump in the direction of the ribs, while no statistically significant change is seen in the direction perpendicular to the ribs.

Keywords: Michael Johnson, fluids, liquid jet impingment, superhydrophobic, Cassie, Wenzel

ACKNOWLEDGEMENTS

I would like to thank everyone who supported me throughout my graduate career. Dr Maynes, Dr Crockett, and Dr Webb have been instrumental in guiding me through this process and helped me grow as a researcher and a writer. I would also like to thank Benton Russell for helping to lay the groundwork for my thesis, Joseph Prince who assisted in the manufacture of target surfaces, and Rob Condie who assisted in the experimental measurements.

Most of all, I would like to thank my wife Tiffany, whose patience and support have been indispensable.

This research was supported by the National Science Foundation (Grant CBET-1066356).

TABLE OF CONTENTS

LIST OF TABLES vii
LIST OF FIGURES ix
NOMENCLATURE xiii
1 Introduction 1
1.1 Project Scope 1
1.2 Thesis Organization 2
2 Background 3
2.1 Surface Hydrophobicity 3
2.2 Superhydrophobic Surfaces 4
2.3 Free Surface Liquid Jet Impingement 5
2.4 Jet Impingement on Patterned Surfaces 6
2.5 Research Contributions 8
3 Experimental Method 9
3.1 Test Apparatus 9
3.2 Experimental Procedure 10
3.3 Surface Fabrication 13
4 Hydraulic Jump Due to Jet Impingement on Micro-Patterned Surfaces Exhibiting Ribs and Cavities 15
4.1 Contributing Authors and Affiliations 15
4.2 Abstract 15
4.3 Introduction 16
4.4 Experimental Method 21
4.5 Experimental Scope 24
4.6 Results 25
4.6.1 General Observations 25
4.6.2 Hydraulic Jump Location 27
4.7 Conclusions 35
5 Hydraulic Jumps Due to Jet Impingement on Superhydrophobic Surfaces Exhibiting Ribs and Cavities 37

5.1 Abstract 37
5.2 Introduction 38
5.3 Experimental Method 42
5.3.1 Surface Fabrication 45
5.4 Results 47
5.4.1 General Observations 47
5.4.2 Hydraulic Jump Location 53
5.4.3 Longitudinal-to-Transverse Radius Ratio 55
5.4.4 Comparison to Analytical Model 58
5.4.5 Total Thin-Film Area 59
5.5 Conclusion 62
6 Conclusion 65
6.1 Future Work 66
REFERENCES 69
Appendix A. Tabulated Results 73
Appendix B. Matlab Code 79
B.1 Description 79
B.2 Video Analysis Script 79
B.3 Script for Calibration and Combining Individual Experiments 123

LIST OF TABLES

Table 3-1. Cavity fraction (F_c), with the corresponding module width (w), and cavity width (w_c) of each surface tested. 14

Table 4-1. Cavity fraction (F_c), with the corresponding module width (w), and cavity width (w_c) of each surface tested. 25

Table 5-1. Cavity fraction (F_c), with the corresponding module width (w), and cavity width (w_c) of each surface tested. 47

Table A-1. Experimental results for hydraulic jumps on a smooth, uncoated surface ($F_c = 0$) 73

Table A-2. Experimental results for hydraulic jumps on an uncoated $F_c = 0.5$ surface 74

Table A-3. Experimental results for hydraulic jumps on an uncoated $F_c = 0.8$ surface 75

Table A-4. Experimental results for hydraulic jumps on an uncoated $F_c = 0.93$ surface 76

Table A-5 Experimental results for hydraulic jumps on a coated $F_c = 0.5$ surface 77

Table A-6. Experimental results for hydraulic jumps on a coated $F_c = 0.8$ surface 77

Table A-7. Experimental results for hydraulic jumps on a coated $F_c = 0.93$ surface 78

LIST OF FIGURES

Figure 2-1. Illustration of sessile water droplets on hydrophilic (left), hydrophobic (center), and superhydrophobic surfaces (right) 4

Figure 2-2. An illustration of a rib and cavity superhydrophobic surface in the Cassie state. 5

Figure 2-3. Illustrations of Type I (left) and Type II (right) hydraulic jumps 6

Figure 3-1. Schematic of experimental setup. The adjustment assembly is translated vertically to achieve a desired initial depth. 10

Figure 3-2. SEM images of F_c = 0.5 (left), 0.8 (center), and 0.93 (right) surfaces 13

Figure 4-1. Critical dimensions of the hydraulic jump on a rib and cavity patterned surface. Rib patterning is not to scale. 17

Figure 4-2. Schematic of experimental setup. The adjustment assembly is translated vertically to achieve a desired initial depth. 22

Figure 4-3. Hydraulic jumps on a F_c = 0.93 surface, at $Re = 1.15 \times 10^4$ and $\hat{H}$ = 5 (left), and at $Re = 2.14 \times 10^4$ and $\hat{H}$ = 8.3 (right). 24

Figure 4-4. SEM Images of F_c = 0.5 (left), 0.8 (center), and 0.93 (right) surfaces 25

Figure 4-5. The normalized downstream depth, $\hat{H}$ at which the hydraulic jump collapses as a function of jet Reynolds number, Re, for all surfaces considered. 27

Figure 4-6. $\hat{R}_l$ as a function of $\hat{H}$ for Re ranging from 1.15×10^4 to 2.14×10^4 for the F_c = 0.8 surface. 28

Figure 4-7. $\hat{R}_l$ (left) and $\hat{R}_t$ (right) vs $\hat{H}$ for each surface considered at Re = 16200. 29

Figure 4-8. $\hat{R}_l$ (left) and $\hat{R}_t$ (right) as a function of Re for each surface considered and at $\hat{H}$ = 8.3. 30

Figure 4-9. R_l/R_t as a function of $\hat{H}$ at Re = 16200 (left) and R_l/R_t as a function of Re at $\hat{H}$ = 8.3 (right) for F_c = 0.5, 0.8, and 0.93 surfaces. 31

Figure 4-10. $\hat{A}$ as a function of $\hat{H}$ for the F_c = 0.8 surface and for all Re explored (left), and as a function of Re for $\hat{H}$ = 8.3 and for all surfaces (right). 33

Figure 4-11. Comparison of the present experimental data to the analytical solution presented by Bush and Aristoff [20]. 35

Figure 5-1. Critical dimensions of the hydraulic jump on a rib and cavity patterned surface. Rib patterning is not to scale. 40

Figure 5-2. Schematic of experimental setup. The adjustment assembly is translated vertically to achieve a desired initial depth....43

Figure 5-3. SEM images of F_c = 0.5 (left), 0.8 (center), and 0.93 (right) surfaces 46

Figure 5-4. The height at which the hydraulic jump breaks up and collapses. Regime 2 is the regime focused on in this study....48

Figure 5-5. Images of Regime 1 transitions on superhydrophobic surfaces with F_c = 0.8 at Re = 12400 (left), and Re = 20400 (right)....49

Figure 5-6. Images showing the progression of a hydraulic jump collapsing and reforming when the downstream depth is too large for the jet momentum to maintain a stable thin film region (Regime 3). 50

Figure 5-7. Images of hydraulic jumps in Regime 2 with F_c = 0.93, $\hat{H}$ = 9.3 and Re = $1.15\text{x}10^4$ (left), and with F_c = 0.93, $\hat{H}$ = 10 and Re = $2.14\text{x}10^4$ (right) 50

Figure 5-8. Longitudinal and transverse transition radii vs $\hat{H}$ for coated and uncoated surfaces where F_c = 0.8 and Re = 18100....51

Figure 5-9. $\hat{R}_l$ and $\hat{R}_t$ as a function of Re for F_c = 0.8 surface where transition from Regime 2 to Regime 1 occurs, compared to previously acquired unimmersed transition data of Maynes et al. [9] 53

Figure 5-10. $\hat{R}_l$ and $\hat{R}_t$ vs $\hat{H}$ for wetted and unwetted cases of F_c = 0.5 where Re = 18100 54

Figure 5-11. $\hat{R}_l$ and $\hat{R}_t$ vs Re of F_c = 0.5 surfaces for wetted and unwetted cases where $\hat{H}$ = 10 in the longitudinal and transverse directions 55

Figure 5-12. Ratio of coated to uncoated hydraulic jump radii as a function of Re at $\hat{H}$ = 9.0 in the longitudinal (left) and transverse (right) directions 56

Figure 5-13. R_l/R_t as a function of $\hat{H}$ for coated surfaces at Re = 14000 (left) and Re = 18100 (right) for each F_c....57

Figure 5-14. R_l/R_t as a function of Re for coated surfaces at each F_c and $\hat{H}$ = 9 58

Figure 5-15. A comparison of analytical and experimental results of $\hat{R}_l$ (left) and $\hat{R}_t$ (right) as a function of $\hat{H}$ for F_c = 0.8 surfaces at multiple Re....59

Figure 5-16. A comparison of analytical and experimental results of R_l/R_t (right) as a function of $\hat{H}$ for F_c = 0.8 surfaces at multiple Re. 60

Figure 5-17. $\hat{A}$ vs $\hat{H}$ for coated surfaces where $F_c = 0.5$ 61

Figure 5-18. $\hat{A}$ vs $\hat{H}$ for all F_c, at $Re = 14000$ (left) and $Re = 19800$ (right).....61

Figure 5-19. A_c/A_u as a function of Re at $\hat{H} = 9$ for all F_c.....62

NOMENCLATURE

a	Jet radius
A	Thin film area
A_j	Jet area
$\hat{A}$	Thin film area normalized by Jet Area, A/A_j
A_c	Thin film area for coated surfaces
A_u	Thin film area for uncoated surfaces
F_c	Cavity Fraction, w_c/w
h	Thin film thickness
H	Downstream depth
$\hat{H}$	Normalized Downstream Depth, H/a
y	Radial coordinate in thin film region
Re	Reynolds number, $Q/\nu a$
R_{eq}	Equivalent circular jump radius, $(A_j/\pi)^{1/2}$
R_l	Longitudinal jump radius
$\hat{R}_l$	Normalized longitudinal jump radius, R_l/a
R_t	Transverse jump radius
$\hat{R}_t$	Normalized transverse jump radius, R_t/a
w	Rib and cavity module width
w_c	Width of a surface cavity
We	Weber number, $\rho V^2 a/\sigma$
V	Jet velocity
Q	Jet volume flow rate
ν	Liquid kinematic viscosity
ρ	Liquid density
σ	Liquid surface tension
θ_a	Advancing contact angle
θ_r	Receding contact angle

1 INTRODUCTION

Over the past decade, superhydrophobic surfaces have become a common area of research in the field of fluid dynamics due to their unique water repellant and drag reducing properties. Superhydrophobic surfaces are created by combining chemical hydrophobicity with micron-scale surface roughness, which results in a gas-liquid interface over a significant portion of the surface. With the advent of micro fabrication, researchers can now create and characterize surfaces with repeatable topology which enables them to more fully research the dynamics of flow over these surfaces. Experimental and computational work has been performed in a multitude of applications including droplet behavior, channel flow, and heat transfer. One emerging application of superhydrophobic surfaces is free surface, perpendicular jet impingement, which can be used for cooling, mixing or aerating in small scale engineering applications. In addition, this provides insights into multidirectional flows over anisotropic surface topologies, the effect of which is particularly strong due to thin-film flows.

1.1 Project Scope

The purpose of this research was to experimentally investigate the hydraulic jump downstream of a vertical jet impinging downward on a surface exhibiting micro-scale ribs and cavities. The radial location of the hydraulic jump was measured in the directions parallel and perpendicular to

the ribs. The experiments were performed with a single jet diameter at a fixed height above the surface. The parameters explored were surface patterning, surface hydrophobicity, flow rate, and downstream depth. Four patterns were studied, including a smooth surface and three different rib-patterned surfaces. Each pattern was investigated with hydrophobic and hydrophilic surface conditions to compare the varying dynamics associated wetting and non-wetting surfaces. Experiments were performed at six different flow rates in the Reynolds number range of $1.15x10^4$ to $2.14x10^4$, and the corresponding Weber number range of $3x10^2$ to $1.05x10^3$. Each combination of Reynolds number and surface patterning was studied at all downstream depths at which a stable hydraulic jump appears.

1.2 Thesis Organization

Chapter 2 provides background for the present research, including the motivation for this work and a literature review of superhydrophobic surfaces and jet impingement. Chapter 3 describes the experimental apparatus and the method used to acquire the presented data. Chapter 4 presents a stand-alone paper which was submitted to the American Society of Mechanical Engineers, for publication in conjunction with a conference presentation. The content of this paper focuses on jet impingement on hydrophilic, patterned surfaces and illuminates the effect that surface patterning has on the location of the hydraulic jump. Chapter 5 also presents a paper that will be submitted independently for publication, which investigates the effect of hydrophobicity on patterned surfaces. Chapter 6 presents conclusions and offers recommendations for future work.

2 BACKGROUND

2.1 Surface Hydrophobicity

The hydrophobicity of a surface is measured by the contact angle which is defined as the interior angle between a single droplet of water and the surface in question. Surfaces are divided into three categories describing their hydrophobicity, illustrations of which are shown in Figure 2-1. Hydrophilic surfaces are defined as any surface which, when a sessile droplet is placed upon it, the contact angle is less than 90 degrees. When such a droplet is placed on a moderately inclined surface, the droplet will likely remain stationary. Hydrophobic surfaces result in contact angles greater than 90 degrees, and roll off of inclined surfaces more easily. The maximum contact angle that a smooth surface can achieve by coating alone is nominally 120 degrees. Therefore, any surface which achieves contact angles in excess of 120 degrees is defined as superhydrophobic. Droplets placed on these surfaces require very small angles of inclination in order to remain stationary.

Another measure of hydrophobicity is the degree of contact angle hysteresis of a moving droplet, or the difference between the contact angles on the droplet's advancing and receding sides. As a droplet rolls along a surface, the contact angle on the advancing side of the surface, θ_a, increases compared to the contact angle of the static droplet. Conversely, the contact angle on the receding side of the surface, θ_r, decreases. The surface tension that results from this disparity

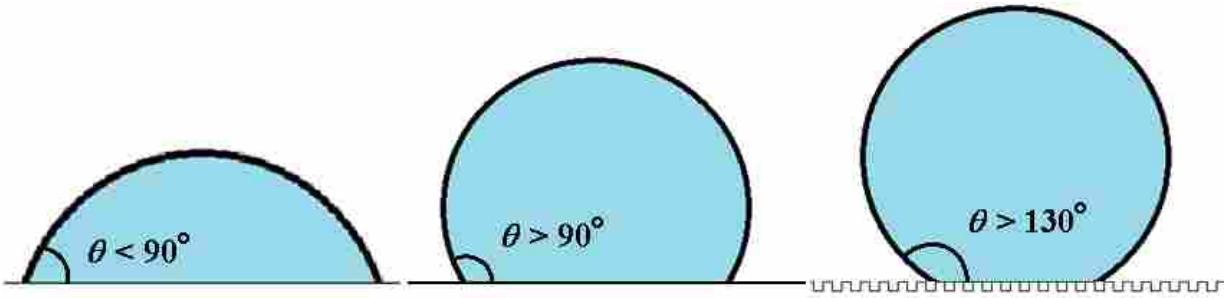

Figure 2-1. Illustration of sessile water droplets on hydrophilic (left), hydrophobic (center), and superhydrophobic surfaces (right)

in advancing and receding contact angles provides resistance to the rolling droplet, so the smaller the hysteresis, the more hydrophobic a surface is.

2.2 Superhydrophobic Surfaces

Superhydrophobic surfaces are created by combining micro-scale topology with hydrophobic surface chemistry. When a liquid comes in contact with such a surface, the surface tension of the liquid prevents it from flooding the cavities, thus creating a liquid-gas interface on a large portion of the surface. When air is trapped in the cavities of a superhydrophobic surface, the surface is said to be in the Cassie state. In this state, the velocity of the fluid at that interface is non-zero which results in an effective slip over superhydrophobic surfaces, thus reducing frictional resistance over the surface. If water is allowed to flood the cavities, the surface is in the Wenzel state which results in the classical no-slip situation [1]. A pattern which has been commonly used in fabricating superhydrophobic surfaces is a series of alternating micro-ribs and cavities. Figure 2-2 is an illustrated cross-section of water flowing over a rib and cavity superhydrophobic surface. These surfaces are characterized by the cavity fraction, which is defined as the width of a cavity, w_c, divided by the module width, w, or the combined width of a cavity and adjoining rib ($F_c = w_c/w$). Many studies have focused on flow over these surfaces with

the intent of investigating drag reduction [1-9]. These studies have reported that greater drag reduction is observed when the flow runs parallel to the ribs than when the flow runs perpendicular to them [2,3].

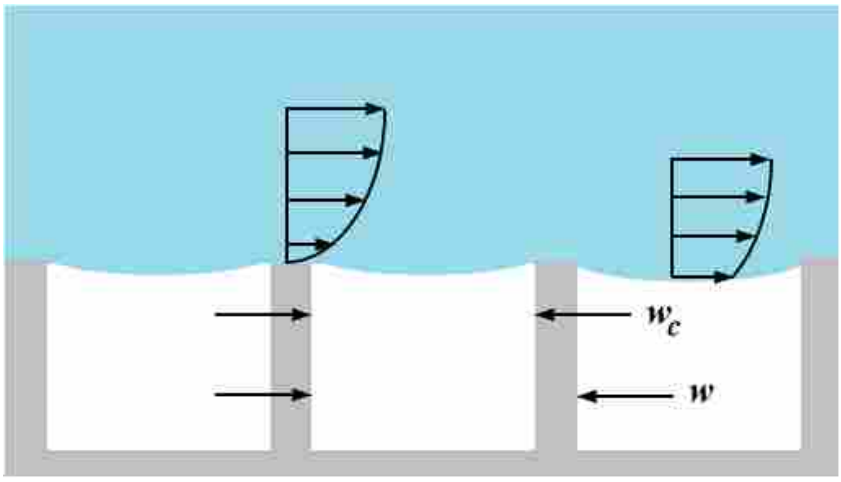

Figure 2-2. An illustration of a rib and cavity superhydrophobic surface in the Cassie state.

2.3 Free Surface Liquid Jet Impingement

When a vertical liquid jet impinges upon a smooth horizontal surface, the liquid subsequently spreads radially in a circular thin film until a hydraulic jump occurs. The thickness of the film typically increases by greater than an order of magnitude, and the velocity of the liquid decreases to satisfy continuity. This jump balances the momentum of the fluid with the hydrostatic force of the liquid downstream from the thin film region. In Watson's seminal paper, a model was introduced to predict the location of the hydraulic jump for laminar and turbulent flows in terms of jet velocity, jet diameter, and downstream liquid depth [14]. Many experimental studies have been performed and compared to Watson's analysis, with varying agreement [15-22]. Bush & Aristoff have more recently updated Watson's model to account for azimuthal surface tension in the jump, which has improved agreement with experimental results

[20]. Many experimental studies have reported secondary flow structures downstream of the jump. These structures directly affect the momentum of the fluid downstream of the jump and consequently its radial location. Ellegaard et al. [18] classified these flow structures into two types which are illustrated in Figure 2-3. Type I jumps are described as a smooth, S-shaped jump where the surface flow remains unidirectional and a long circulation eddy forms along the solid surface beyond the jump. Type II jumps develop as the downstream depth increases, where the jump becomes more abrupt, and a second eddy develops along the surface of the jump. Liu & Leinhard [19] observed that while Watson's model is generally accurate for Type I jumps, it overpredicts the jump radius for Type II jumps. This is, in part, because Type II jumps occur when the jump radius is relatively small, in which case surface tension becomes significant and reduces the diameter of the jet.

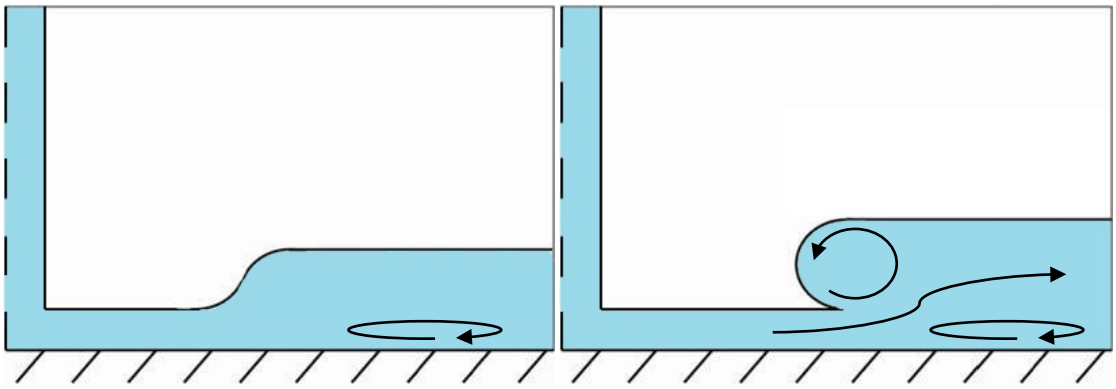

Figure 2-3. Illustrations of Type I (left) and Type II (right) hydraulic jumps

2.4 Jet Impingement on Patterned Surfaces

Recently, the influence of surface patterning and superhydrophobic surfaces on the impingement thin-film flow physics and associated hydraulic jump transitions has been investigated [10-13]. Dressaire et al. investigated experimentally the influence of post arrays on

the location and shape of the hydraulic jump [11, 12]. The posts were fabricated using standard micro-fabrication methods and were 100 μm in diameter and ranged from 200 to 400 μm in height. Their study used hydrophilic surfaces, so the data focused on Wenzel state flow. Their results showed that surfaces patterned with posts result in polygonal and star-shaped hydraulic jumps. Different shapes were achieved depending on the distribution pattern of the posts on the surface. The average jump radius compared well to the analytical model provided by Bush & Aristoff [20]. In addition, they presented an analytical model in terms of an anisotropic effective surface slip that was determined based on their measured results. This surface slip is due to flow in the wetted cavities below the tops of the posts. While Dressaire clearly demonstrated that imposing anisotropic surface roughness directly affects the location of the hydraulic jump, the principal directions where the maximum and minimum slip lengths were exhibited were separated by a maximum of 22.5 degrees, corresponding to the separation between the directions along posts and in between all posts. The result is that the flow had a relatively small degree of anisotropy, and surface tension played a significant role in defining the shape of the hydraulic jump. The effect of anisotropic roughness is more effectively highlighted as the angular separation between the minimum and maximum slip lengths is increased.

Kibar et al. studied the dynamics of an inclined jet impinging on a randomly patterned vertical surface with a jet Weber number ranging from 5 to 650 [10]. The jet initially spreads into a thin sheet upon impact, but the slowing due to friction and the high degree of hydrophobicity causes the sheet to rejoin into a jet and jump off of the surface. They reported a 40% drag reduction as the contact angle increased from 145° to 167°.

Maynes et al. studied jet impingement on surfaces with alternating micro-ribs and cavities patterned onto the surfaces [9]. This study considered both the Wenzel and Cassie states.

The width of the cavities in this study ranged from 32 – 37 μm and the cavity depth was nominally 15 μm. For these experiments a downstream water depth was not imposed. This resulted in noteworthy differences in transition types. Impingement on the Cassie state surfaces caused an elliptical transition and instead of the classical hydraulic jump, the film broke into filaments or droplets due to surface tension at a specific radial location. The Wenzel state surfaces yielded an elliptical hydraulic jump. However, the downstream depth was neither imposed nor measured, therefore the hydraulic jump measurements could not be compared to findings from previous experimental studies or analytical solutions.

2.5 Research Contributions

The purpose of this research is to expand upon the work performed by Maynes et al. [9] to include data where a downstream depth is imposed. With this downstream depth, a hydraulic jump can be forced on the superhydrophobic surfaces, and this flow can be compared to flows over hydrophilic surfaces at the same conditions. The downstream depth also provides the necessary information to compare the experimental data to the analytical model of Bush and Aristoff. This research sheds light on the complex flow dynamics that result from multidirectional flow over anisotropically patterned surfaces.

3 EXPERIMENTAL METHOD

3.1 Test Apparatus

The test apparatus consisted of a vertically oriented nozzle of radius a = 0.6 mm located 20 mm above the horizontal test surface of interest. The surface was placed on an aluminum plate 20 cm in diameter that was suspended in a 1 m diameter reservoir filled with deionized water. The elevation of the plate relative to the water surface level was adjustable, and thus the downstream water depth, H, was easily varied. The downstream water depth was measured using a needle micrometer stage, with a measurement uncertainty of $\pm 4 \times 10^{-5}$ m. Two CCD video cameras were aligned to capture the jump diameter in the longitudinal and transverse directions, respectively. The camera used to measure the jump diameter in the longitudinal direction was a high-speed camera capable of 1040x1040 pixel resolution, and operated at 60 frames per second during data acquisition. The camera used to measure the diameter in the transverse direction was a CCD camera with 640x480 pixel resolution and captured data at 30 frames per second. Since neither camera was aligned orthogonally with respect to the plate, the only diameter they accurately measured was the direction in which it was aligned. Therefore, the only radii acquired were those along the major and minor axes of the elliptically shaped transition. The nozzle was fed by a 4 liter plenum filled with water which is connected by a 2 meter long section of 6.35 mm tubing. The plenum was pressurized to maintain a constant flow rate over the duration of a

test. The uncertainty for velocity measurements was acquired by measuring the volume flow rate in small increments over the typical duration of a test, applying a linear curve fit, and determining the variance from the fit. This was performed several times at various Reynolds numbers. The resulting velocity uncertainty was ±1.2%, with a corresponding Reynolds number uncertainty of ±3.6%.

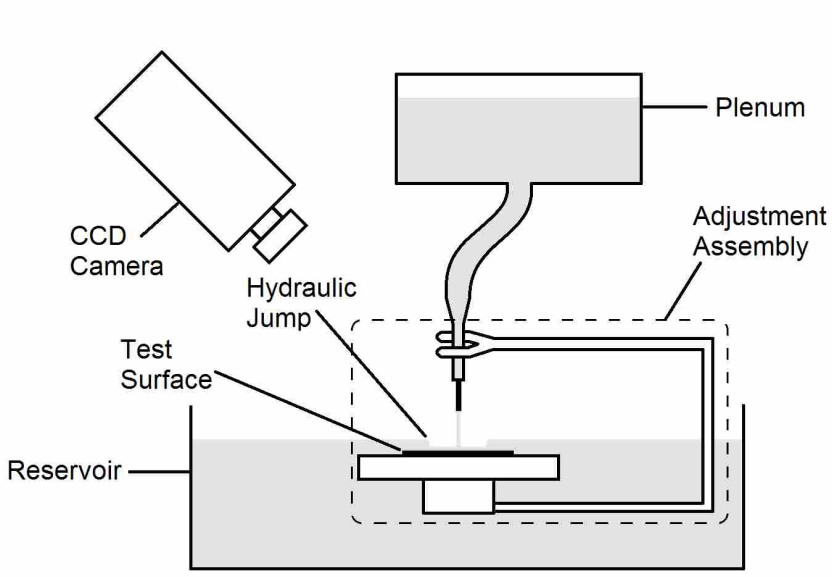

Figure 3-1. Schematic of experimental setup. The adjustment assembly is translated vertically to achieve a desired initial depth.

3.2 Experimental Procedure

Three replicate experiments were performed on each combination of jet velocity and surface type, and the radial jump locations from the three replicates were then averaged. The procedure was as follows. The jet velocity was adjusted by changing the pressure in the plenum and determined by measuring the time required to collect a known volume of water. For wetting surfaces, the water depth on the surface was adjusted to a nominal value of 2.8 mm prior to initiating the flow. Non-wetting surfaces exhibited a minimum depth required to maintain a

hydraulic jump. The minimum depth was determined prior to testing each Weber number, and the initial depth was adjusted accordingly. When the flow began, the large (essentially constant diameter) reservoir collected the water, and thereby the downstream depth increased linearly with time at rates ranging from 3.2×10^{-5} to 6×10^{-5} m/s. The video cameras were started before the impingement process began and ended after the jet had been turned off so that the timing of the initial jet impingement and the end of the flow could be recorded. The test was conducted until the downstream depth became too large and the hydraulic jump collapsed inward on the incoming water jet. The water was immediately turned off, and a final downstream depth was measured.

A computer program was developed that identifies and tracks the radial position of the hydraulic jump for each frame of the video using an edge-detection algorithm. Software limitations prevented the algorithm from analyzing more than 2000 frames in a test, so the videos were trimmed to between 6 and 30 frames per second. The edge detection algorithm used the brightness values in a window centered on the average jump location of the 5 previous frames, or about 0.167 to 1 second prior to the frame being analyzed. The lighting was set up such that a nominally dark shadow of nominal width of 8 pixels occurred at the hydraulic jump. The location of this jump was determined by taking the derivative of the brightness values and finding the maximum change of this derivative from light to dark in the jump region. The uncertainty associated with identifying the radial position of the hydraulic jump was ±4 pixels, based on the average width of the dark region associated with the hydraulic jump. The pixel measurement was then mapped to physical length scales by calibrating the videos based on an image taken of a reference scale after each test. This resulted in a nominal uncertainty of each

instantaneous radial measurement of ±3%. The algorithms used to measure the jump radius and calibrate can be found in Appendix B.

The downstream depth for each frame was then determined by a linear interpolation between the depths measured at the first and last frames when the jet was seen to be impinging on the surface. The validity of this method was verified experimentally by running the water at regular intervals, allowing the reservoir to fill to a fraction of the level taken during an actual test, and measuring the change in height to confirm that it was still linear. The test resulted in a linear trend to within ±1% uncertainty.

Six jet velocities were explored for each surface, yielding a jet Weber number ($We = \rho V^2 a/\sigma$) range of $3\text{x}10^2$ to $1.05\text{x}10^3$ where ρ and σ are the liquid density and surface tension, respectively, V is the velocity and a is the radius of the jet. The corresponding Reynolds number ($Re = Q/\nu a$) range is given as $1.15\text{x}10^4$ to $2.14\text{x}10^4$ where Q is the volume flow rate of the jet, and ν is the kinematic viscosity of the fluid.

In addition to the experiments performed above, a number of images have been captured using a high speed camera for visualization purposes. These images were captured at a wide range of Reynolds numbers and downstream depths. The images are illuminated by a light source with a diffuser, and the images are taken at a frame rate of 500 frames per second.

An important analysis of these experiments involved determining the area of the thin-film region prior to the hydraulic jump. This area was approximated by assuming an elliptically shaped jump. The area of the ellipse was calculated by assuming the longitudinal and transverse jump radii to be the semi-major and semi-minor axes, respectively. The validity of this assumed shape was tested by integrating the area of several sample images at several flow conditions, and

comparing the results with the elliptical approximation. This analysis resulted in an average uncertainty of ± 0.8% for the total thin-film area.

3.3 Surface Fabrication

Test surfaces were fabricated using 101.6 mm diameter silicon wafers using standard photolithographic processes. Since silicon is natively hydrophilic, these patterned surfaces were used to test the Wenzel state. To achieve the Cassie state, the surfaces were subsequently coated with a thin layer of chromium and Teflon. Three surfaces were used with cavity fractions of F_c = 0.5, 0.8, and 0.93. Representative SEM images of the surfaces used are shown in Figure 3-2. The rib height was nominally 15 μm for each surface. Polished silicon wafers were used for the smooth surfaces.

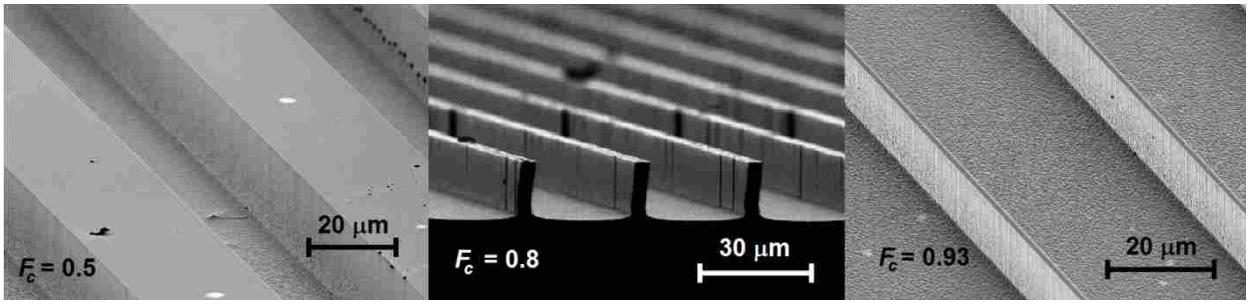

Figure 3-2. SEM images of F_c = 0.5 (left), 0.8 (center), and 0.93 (right) surfaces

Table 3-1 shows the dimensions and corresponding cavity fraction of each surface used, as well as the receding (θ_r) and advancing (θ_a) contact angles for the hydrophilic (uncoated) and superhydrophobic (coated) cases. The advancing contact angles are acquired by placing a droplet on the surface with a needle continually adding volume to the droplet until the boundary of the droplet expands along the surface. The angle between the surface and the edge of the droplet is

then measured while the droplet grows. Receding contact angles are measured by drawing the liquid in the droplet back into the needle until the edge of the droplet recedes along the surface and measuring the angle. All of the coated surfaces maintain hydrophobic contact angles, with all patterned surfaces resulting in contact angles in excess of 120°, thereby characterizing them as superhydrophobic. The advancing contact angles in the transverse direction are larger than those in the longitudinal direction. Conversely, the receding transverse contact angles are smaller than the receding contact angles in the longitudinal direction. As F_c increases, θ increases in concordance with Cassie's law. In the hydrophilic, wetting cases, the advancing contact angles are less than 90° as expected. These angles are much smaller in the longitudinal direction than in the transverse direction. This is because as a droplet is placed on the surface, the water wicks into the channels, pulling the droplet in the longitudinal direction. When the water in the droplet is drawn back into the needle to measure the receding contact angle, the water in the channels is not drawn out, and the droplet does not recede. Thus, each hydrophilic receding contact angle is measured as 0°.

Table 3-1. Cavity fraction (F_c), with the corresponding module width (w), and cavity width (w_c) of each surface tested.

F_c	w (mm)	w_c (mm)	Coated (Non-Wetting)		Uncoated (Wetting)	
			θ_a (°) Long/Trans	θ_r (°) Long/Trans	θ_a (°) Long/Trans	θ_r (°) Long/Trans
0	None	None	125	109	87	49
0.5	60	30	140/168	127/121	10/81	0/0
0.8	40	32	150/168	140/133	15/43	0/0
0.93	40	37.2	158/168	146/144	13/62	0/0

4 HYDRAULIC JUMP DUE TO JET IMPINGEMENT ON MICRO-PATTERNED SURFACES EXHIBITING RIBS AND CAVITIES

This chapter is a paper which was submitted for the ASME 2012 International Mechanical Engineering Congress and Exposition. As such, the literature review and experimental method previously described are summarized in this chapter. The formatting of the paper has been modified to fit the stylistic requirements of this thesis.

4.1 Contributing Authors and Affiliations

M. Johnson, D. Maynes, J.C. Vanderhoff, and B.W. Webb

Department of Mechanical Engineering, Brigham Young University, Provo, Utah, United States

4.2 Abstract

This paper reports experimental results characterizing the hydraulic jumps that form due to liquid jet impingement on micro-patterned surfaces with alternating micro-ribs and cavities. The surfaces are characterized by the cavity fraction, which is defined as the width of a cavity divided by the combined width of a cavity and an adjoining rib. The surfaces are all hydrophilic and thus the cavity regions are wetted during the impingement process. Four different surface designs were studied, with respective cavity fractions of 0 (smooth surface), 0.5, 0.8, and 0.93. The experimental data spans a Weber number range (based on the jet velocity and radius) of

$3x10^2$ to $1.05x10^3$ and a corresponding Reynolds number range of $1.15x10^4$ to $2.14x10^4$. As with jet impingement on a smooth surface, when a liquid jet strikes a ribbed surface it then moves radially outward in a thin film and eventually experiences a hydraulic jump, where the thickness of the film increases by an order of magnitude, and the velocity decreases accordingly. However, the anisotropy of the patterned surface causes a disparity in frictional resistance dependent upon the direction of the flow relative to the orientation of the ribs. This results in a hydraulic jump which is elliptical rather than circular in shape, where the major axis of the ellipse is aligned parallel to the ribs, concomitant with the frictional resistance being smallest parallel to the ribs and greatest perpendicular to the ribs. When the water depth downstream of the jump was imposed at a predetermined value, the major and minor axis of the jump decreased with increasing water depth, following classical hydraulic jump behavior. The experimental results indicate that for a given cavity fraction and downstream depth, the radius of the jump increases with increasing Reynolds number. At a specified Reynolds number and downstream depth, the hydraulic jump radius in the direction parallel to the ribs of a patterned surface is nominally equal to the jump radius for a smooth surface, regardless of cavity fraction. The jump radius perpendicular to the ribs is notably less than that for a smooth surface, and this radius decreases with increasing cavity fraction.

4.3 Introduction

When a vertical liquid jet strikes a smooth horizontal surface, the liquid subsequently spreads radially in a circular thin film as illustrated in Figure 4-1 and described by Watson in his seminal paper [14]. Initially, a boundary layer begins to develop along the plate, starting from the stagnation point, while outside of the boundary layer the jet velocity remains equal to that of the

impinging jet. The film thickness, *h*, decreases with increasing radial coordinate, *r*, until the boundary layer reaches the surface of the film. The film surface velocity then begins to decrease with increasing *r* and the film thickness begins to gradually increase. This behavior continues until a hydraulic jump occurs, which is characterized by a sudden large increase in liquid depth and corresponding decrease in the average velocity of the fluid.

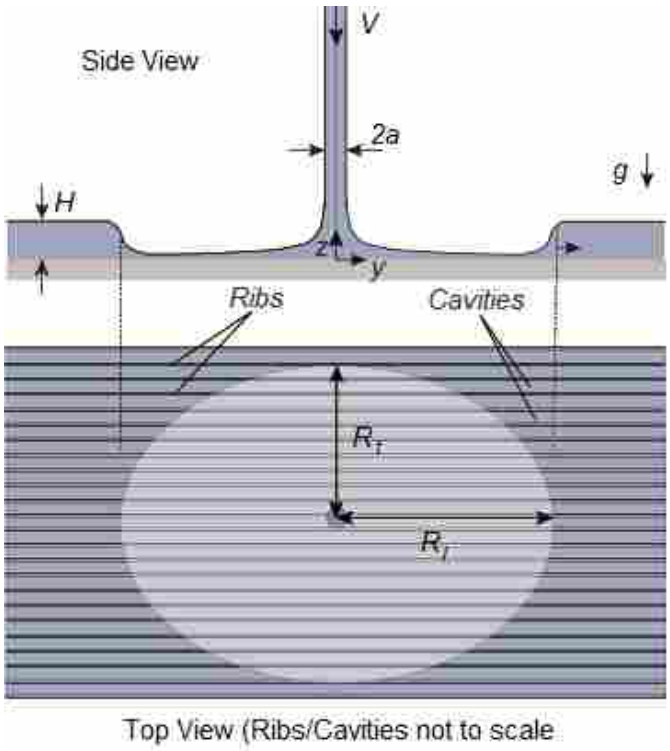

Figure 4-1. Critical dimensions of the hydraulic jump on a rib and cavity patterned surface. Rib patterning is not to scale.

Experimental and analytical investigations into free-surface liquid jet impingement on smooth surfaces have been extensively performed [14-22]. Watson developed a model based on conservation of mass and momentum which accounted for the boundary layer in the film region and thus the viscous influences throughout the thin film region [14]. Many experimental studies have been performed and compared to Watson's analysis, with varying agreement dependent on

flow dynamics within the jump. Experiments have found various jump shapes and flow structures immediately downstream of the jump [14-22]. Ellegaard et al. [18] classified these flow structures into two types. Type I jumps are described as a smooth, S-shaped jump where the surface flow remains unidirectional and a long circulation eddy forms along the solid surface beyond the jump. Type II jumps develop as H increases, where the jump becomes more abrupt, and a second eddy develops along the surface of the jump. Liu & Leinhard [19] observed that while Watson's model is generally accurate for Type I jumps, it over predicts the jump radius for Type II jumps. This is, in part, because Type II jumps occur when R_j is relatively small, in which case surface tension becomes significant and reduces the diameter of the jet. Bush & Aristoff updated Watson's laminar model to account for the surface tension force caused by curvature of the free surface at the jump location [20]. This reduced the shortcoming in Watson's original model where H is large and R_j is small and resulted in better agreement with experimental data.

Jet impingement may be used as a method of cooling, mixing or aerating in small scale engineering applications [24]. While a general understanding of the fluid dynamics of general flow over surfaces has been explored, further study into many specific instances have yet to be studied. One such application is impingement on surfaces with anisotropic roughness. When a jet impinges on a surface that exhibits spatial variation such as roughness or surface texturing of a regular form, the thin film dynamics and shape of the hydraulic jump can be significantly altered from the smooth surface scenario. For roughness or surface texturing that exhibits anisotropy, the boundary layer thickness, film thickness, and film surface velocity will all exhibit spatial variation in the tangential coordinate and the dynamics are no longer symmetric. Since the location at which the hydraulic jump occurs depends on a local balance between fluid

momentum and the hydrostatic and surface tension forces, variations in the surface roughness or texturing will directly affect the shape and location of the hydraulic jump

Recent studies have been performed to explore the influence of variations in surface topology on the impingement thin-film flow physics and associated hydraulic jump transitions [9-12]. Dressaire et al. investigated experimentally the influence of post arrays on the location and shape of the hydraulic jump [11, 12]. The posts were fabricated using standard micro-fabrication methods and were 100 μm in diameter and ranged from 200 to 400 μm in height. The surfaces were hydrophilic so that water completely wet the region between posts. Their results showed that surfaces patterned with posts result in polygonal and star shaped hydraulic jumps. Different shapes were achieved depending on the distribution pattern of the posts on the surface. The average jump radius compared well to the analytical model provided by Bush & Aristoff [20]. In addition they presented an analytical model in terms of an anisotropic effective surface slip that was determined based on their measured results. This surface slip is due to flow in the wetted cavities below the tops of the posts. While Dressaire clearly demonstrated that imposing anisotropic surface roughness directly affects the location of the hydraulic jump, the principal directions where the maximum and minimum slip lengths were exhibited were separated by a maximum of 22.5 degrees, corresponding to the separation between along posts and in between all posts. The result is that the flow had a relatively small degree of anisotropy, and surface tension played a significant role in defining the shape of the hydraulic jump. The effect of anisotropic roughness is more effectively highlighted as the angular separation between the minimum and maximum slip lengths is increased.

Maynes et al. studied jet impingement on surfaces with alternating micro-scale ribs and cavities patterned onto the surfaces [9]. This study considered cases where the surfaces were

hydrophilic (uncoated) and water flooded the cavities (Wenzel state), and cases where the surface was coated with a hydrophobic coating (i.e., superhydrophobic surfaces), which caused the water to sit above the cavities, resulting in a vapor-liquid interface over the majority of the surface (Cassie-Baxter state). The width of the cavities in this study ranged from 32 – 37 μm and the cavity depth was nominally 15 μm. For these experiments a downstream water depth was not imposed. This resulted in noteworthy differences in transition types. Impingement on the Cassie state surfaces caused an elliptical transition and instead of the classical hydraulic jump, the film broke into filaments or droplets due to surface tension at a specific radial location. The Wenzel state surfaces yielded an elliptical hydraulic jump. However, the downstream depth was neither imposed nor measured, therefore the hydraulic jump measurements could not be compared to findings from previous experimental studies or analytical solutions.

This paper reports experimental results characterizing the hydraulic jumps that form due to liquid jet impingement on micro-patterned surfaces, specifically alternating micro-ribs and cavities as can be seen in the bottom portion of Figure 4-1. The use of ribs and cavities provides a significant difference in slip between the directions parallel and perpendicular to the ribs, respectively. This contributes to the general application of flows in multiple directions with anisotropic slip lengths. The surfaces are characterized by the cavity fraction, which is defined as the width of a cavity divided by the combined width of a cavity and adjoining rib ($F_c = w_c/w$). They are fabricated using standard photolithographic processes and are all hydrophilic. Consequently, the cavity regions are wetted during the impingement process. Four different surface designs were studied, with respective cavity fractions of $F_c = 0$ (smooth surface), 0.5, 0.8, and 0.93. The experimental data spans a Weber number range (based on the jet velocity and radius) of $We = \rho V^2 a/\sigma = 3\text{x}10^2$ to $1.05\text{x}10^3$ and a corresponding Reynolds number range of $Re =$

$Q/a\nu = 1.15\text{x}10^4$ to $2.14\text{x}10^4$. Impingement on such surfaces results in an elliptical transition where the major axis is aligned with the longitudinal direction (parallel to the ribs), and the minor axis is aligned in the transverse direction (perpendicular to the ribs). The radial jump locations in the longitudinal and transverse directions are presented for the above surfaces and Reynolds numbers and for imposed downstream depths ranging from $H/a = \hat{H} = 5$ to 12.5. The effect of the micro-scale rib/cavity structures is examined by comparing the jump radius to data obtained for a smooth surface at the same flow and downstream depth conditions. The influence of the anisotropic nature of the surface is analyzed by comparing the measured jump length in the longitudinal and transverse directions. The total area encompassed by the thin film region is also calculated and the micro-scale patterned surfaces and the smooth surface data are compared.

4.4 Experimental Method

The test apparatus, a schematic of which is shown in Figure 4-2, consisted of a vertically oriented nozzle of radius $a = 0.6$ mm located 20 mm above the horizontal test surface of interest. The height of the nozzle was chosen to avoid jet break up prior to impingement on the surface. The surface was placed on an aluminum plate 20 cm in diameter that was suspended in a 1 m diameter reservoir filled with water. The elevation of the plate relative to the water surface level was adjustable, and thus the downstream water depth, H, was easily varied. The downstream water depth was measured using a needle micrometer stage, with a measurement uncertainty of $\pm 4\text{x}10^{-5}$ m. Two CCD video cameras were aligned to capture the jump diameter in the longitudinal and transverse directions respectively. Since neither camera was aligned orthogonally with respect to the plate, the only diameter they accurately measured was the direction in which it was aligned. Therefore, the only radii acquired were those along the major

and minor axes. The nozzle was fed by a plenum filled with deionized water with an adjustable pressure to achieve the desired flow rate.

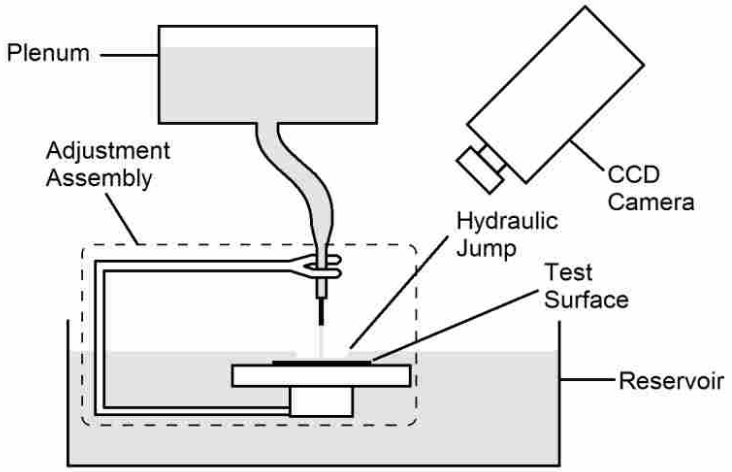

Figure 4-2. Schematic of experimental setup. The adjustment assembly is translated vertically to achieve a desired initial depth.

Three replicate experiments were performed on each combination of jet velocity and surface type using the following procedure, and the results from the three replicates were then averaged. The jet velocity was determined by measuring the time required to collect a known volume of water. The average uncertainty for velocity measurements was 1.2%, which resulted in a Reynolds number uncertainty of 3.6%. The water depth on the surface was adjusted to a nominal value of 2.8 mm prior to initiating the flow. When the flow began, the large (essentially constant diameter) reservoir collected the water, and thereby the downstream depth increased linearly with time at a relatively slow rate. The video cameras were started before the impingement process began and ended after the jet had been turned off so that the timing of the initial jet impingement and the end of the flow could be recorded. The test was conducted until the downstream depth became too large, and the hydraulic jump collapsed inward on the

incoming water jet. The water was immediately turned off, and a final downstream depth was measured.

A computer program was developed that identifies and tracks the radial position of the hydraulic jump for each frame of the video using an edge-detection algorithm. This algorithm used the brightness values in a window centered on the average jump location of the five previous frames. Figure 4-3 shows two examples typical images acquired from these experiments. The lighting was set up such that a dark shadow occurs at the hydraulic jump. The location of this jump was determined by taking the derivative of the brightness values and finding the maximum change of this derivative from light to dark in the jump region. The uncertainty associated with identifying the radial position of the hydraulic jump was ± 4 pixels. The pixel measurement was then mapped to physical length scales by calibrating the videos based on an image taken of a reference scale after each test. This resulted in a nominal uncertainty of each instantaneous radial measurement of ± 3%. The downstream depth for each frame was then determined by a linear interpolation between the depths measured at the first and last frames when the jet was seen to be impinging on the surface. The validity of this method was verified experimentally by running the water at regular intervals, allowing the reservoir to fill to a fraction of the level taken during an actual test, and measuring the change in height to confirm that it was still linear. The test resulted in a linear trend to within 1% uncertainty.

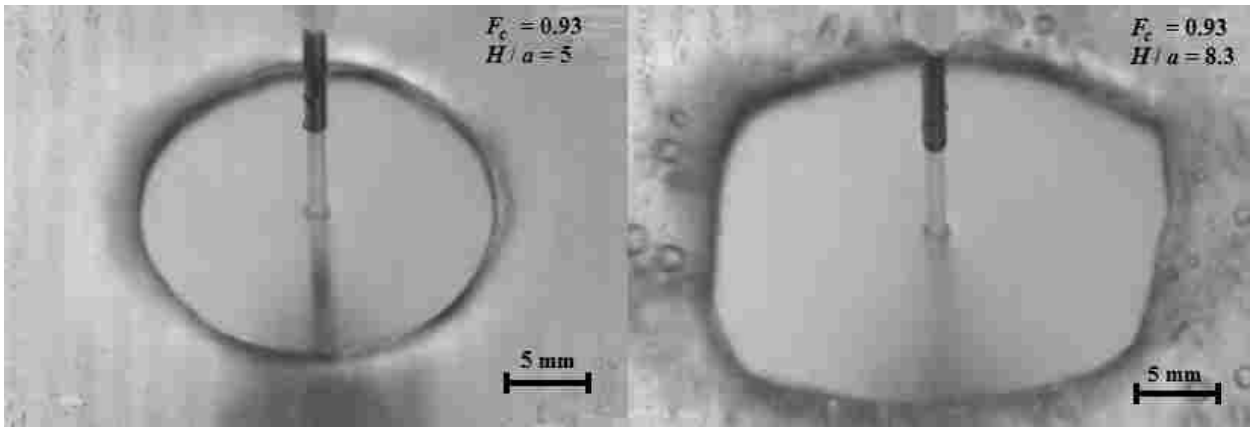

Figure 4-3. Hydraulic jumps on a F_c = 0.93 surface, at Re = 1.15x10^4 and $\hat{H}$ = 5 (left), and at Re = 2.14x10^4 and $\hat{H}$ = 8.3 (right).

4.5 Experimental Scope

Test surfaces were fabricated using 101.6 mm diameter silicon wafers using standard photolithographic processes. Three surfaces were used with cavity fractions of F_c = 0.5, 0.8, and 0.93. SEM images of the surfaces used are shown in Figure 4-4. The rib height was nominally 15 μm for each surface. Polished silicon wafers were used for the smooth surfaces. Table 4-1 shows the dimensions and corresponding cavity fraction of each surface used. Six jet velocities were explored for each surface, yielding a jet Weber number ($We = \rho V^2 a/\sigma$) range of 3x10^2 to 1.05x10^3 where ρ and σ are the liquid density and surface tension respectively, V is the velocity and a is the radius of the jet. The surface tension was determined based on temperature measurements of the water. The corresponding Reynolds number ($Re = Q/\nu a$) range is given as 1.15x10^4 to 2.14x10^4 where Q is the volume flow rate of the jet, and ν is the kinematic viscosity of the fluid. Within this range of Re, the jet is fully turbulent, as the threshold at which turbulence is reached is Re = 4500. Aside from the opacity associated with this turbulence, no surface instabilities were observed with respect to the jet. The turbulence intensity is likely to

dampen upon impingement due to the strong adverse pressure gradient associated with stagnation, somewhat laminarizing the flow in the thin-film region [25].

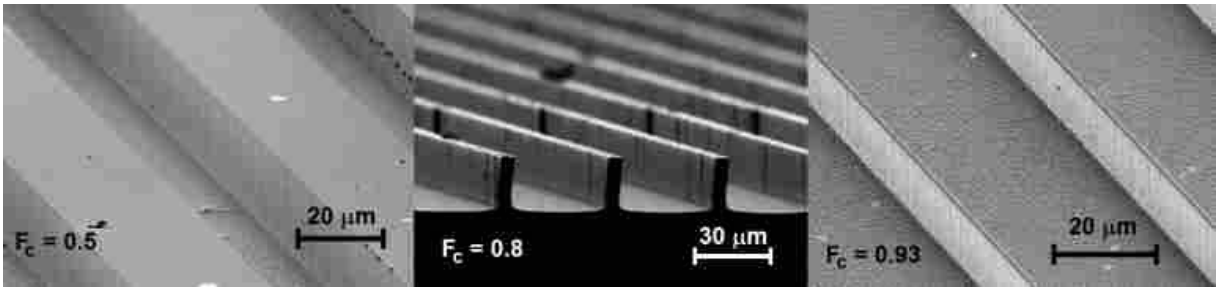

Figure 4-4. SEM Images of F_c = 0.5 (left), 0.8 (center), and 0.93 (right) surfaces

Table 4-1. Cavity fraction (F_c), with the corresponding module width (w), and cavity width (w_c) of each surface tested.

F_c	w (μm)	w_c (μm)
0	None	none
0.5	60	30
0.8	40	32
0.93	40	37.2

4.6 Results

4.6.1 General Observations

For all cases when a vertical jet strikes a horizontal surface, the radius of the hydraulic jump is dependent upon *Re* and $\hat{H}$. As *Re* increases while $\hat{H}$ is held constant, the jump radius increases, and if *Re* is held constant, the jump location decreases as $\hat{H}$ increases. Figure 4-3 shows two examples of the shapes of the various jump transitions observed. While smooth (F_c = 0) surfaces result in circular jumps, for the structured F_c = 0.5 and 0.8 surfaces the transition is elliptical (not shown here) where the major axis runs in the longitudinal direction (along the ribs). For F_c = 0.93, a third transition shape is observed at large downstream depths and

Reynolds numbers. When $Re \leq 14000$, the jump shape is elliptical (as seen in the left image of Figure 4.3), however, for $Re > 16200$, the jump appears elliptical at low downstream depths, but as the depth increases, the ellipse truncates in the longitudinal direction, and exhibits more of a rectangular or polygonal shape. This can be seen in the right image of Figure 4-3. During the course of each experimental run, the downstream depth increased steadily until the jump became unstable and collapsed inward on the jet. When this happened, the behavior was pulsatile with the hydraulic jump formation and subsequent collapse occurring in a periodic manner. The data shows that this critical water depth where the jump collapsed and oscillated was greater for smooth surfaces ($F_c = 0$) than for patterned surfaces. The patterned surfaces showed no consistent trend in the critical $\hat{H}$ with regard to F_c. An increase in the critical depth was observed with increasing Re. The critical depth is plotted vs. Re in Figure 4-5 for all surfaces considered. A possible reason for the pulsatile nature of the collapse is due to surface waves that reflect off the boundary of the reservoir. Even though the reservoir is very large compared to the jet, surface waves reflect and move inward toward the jump location, and the downstream depth fluctuates a very small amount. At the critical depth, the momentum of the thin film is momentarily insufficient to sustain the downstream depth, causing the jump to collapse. This phenomenon has not been reported in previous studies. This may be because most prior experimental work performed has used significantly larger jets with hydraulic jumps at much smaller H and larger R_j values where the jump is more stable.

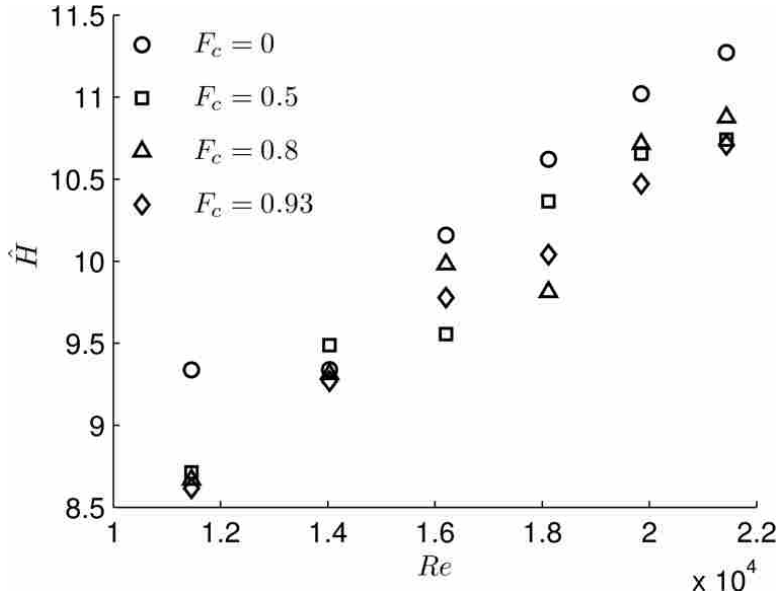

Figure 4-5. The normalized downstream depth, $\hat{H}$ at which the hydraulic jump collapses as a function of jet Reynolds number, *Re*, for all surfaces considered.

4.6.2 Hydraulic Jump Location

This section of the paper considers the radial location of the hydraulic jump in the two primary spreading directions. The normalized radial location of the hydraulic jump in the longitudinal and transverse directions are $\hat{R}_l$, and $\hat{R}_t$ respectively. At a given *Re* they exhibit a very nearly linear decrease with increasing $\hat{H}$. This is demonstrated in Figure 4-6, which shows $\hat{R}_l$ as a function of $\hat{H}$ for each *Re* explored for the F_c = 0.8 surface. This linear dependency between the hydraulic jump radial position and $\hat{H}$ prevails for all *Re.* Consequently, in subsequent figures, linear curve fits to the acquired data are shown.

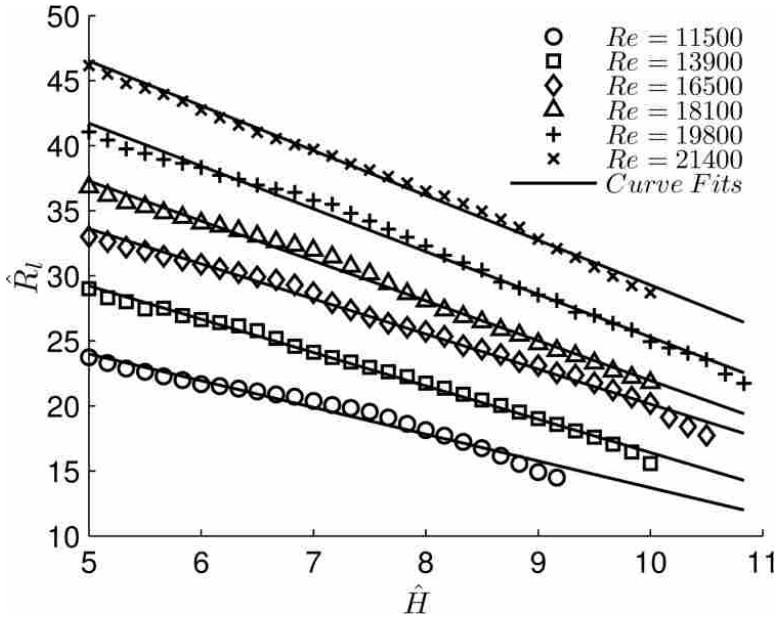

Figure 4-6. $\hat{R}_l$ as a function of $\hat{H}$ for *Re* ranging from 1.15x10^4 to 2.14x10^4 for the F_c = 0.8 surface.

Figure 4-7 shows linear curve fits of the $\hat{R}_l$ (left panel) and $\hat{R}_t$ (right panel) vs. $\hat{H}$ data for each surface considered (F_c = 0, 0.5, 0.8, and 0.93) at *Re* = 16200. The data of Figure 4-7 illustrates several important points. First, the radial location of the hydraulic jump in the longitudinal direction ($\hat{R}_l$) is nominally the same for both the smooth and structured surfaces and appears to be independent of F_c. While some modest departure from the smooth surface data exists at increasing $\hat{H}$, the deviation is slight. In general, the deviation is towards increasing $\hat{R}_l$ with increasing F_c at a given *Re* and $\hat{H}$. The $\hat{R}_l$ radial location coincides with the rib direction and thus the data reveal that the ribs exert only small influence on the longitudinal jump location. Second, the radial location of the hydraulic jump in the transverse direction ($\hat{R}_t$) on the structured surfaces is considerably smaller than the smooth surface at the same *Re* and $\hat{H}$. This behavior occurs presumably due to the increased friction associated with the interaction with each rib as the spreading thin film moves perpendicular to them. The flow in the transverse

direction is analogous to flow over coherent roughness elements. The data of Figure 4-7 further show that the radial location of the jump in the transverse direction is smaller for surfaces of increasing cavity fraction. This occurs because as the ribs spread out and the area on the tops of the ribs decreases, the flow in the cavity region of the surface becomes more pronounced, and the obstruction of the flow provided by the ribs increases. The behavior described above agrees qualitatively with results of Dressaire et al. [11], who showed that flow over surfaces with hydrophilic post structures resulted in smaller jump diameters than predicted by the expression of Bush or Watson at a given imposed downstream depth [14, 20].

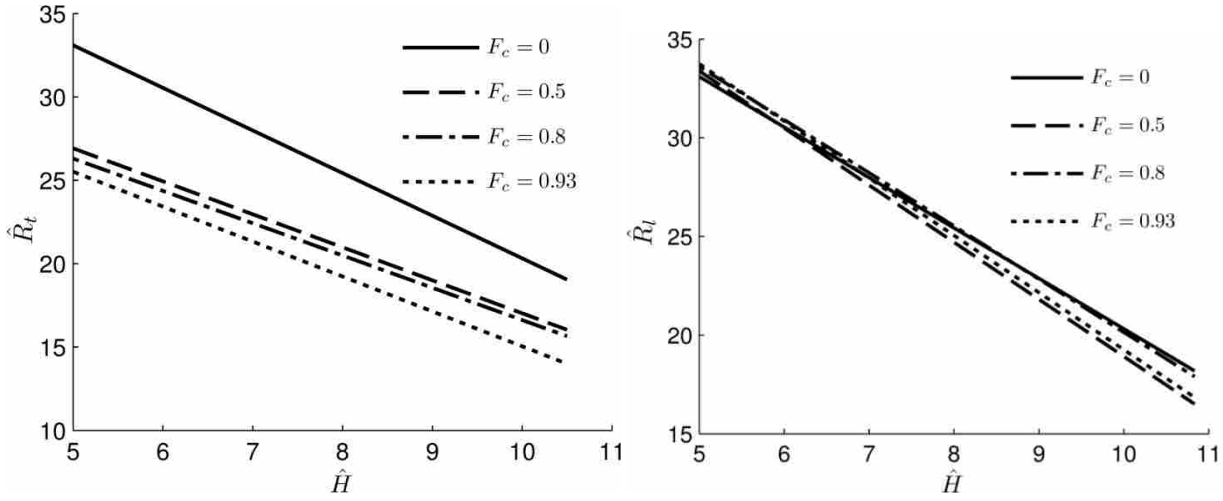

Figure 4-7. $\hat{R}_l$ (left) and $\hat{R}_t$ (right) vs $\hat{H}$ for each surface considered at *Re* = 16200.

Whereas the data of Figure 4-7 explored the influence of $\hat{H}$ on $\hat{R}_l$ and $\hat{R}_t$ at a fixed *Re*, now the influence *Re* exerts on the two hydraulic jump radii is explored. Figure 4-8 presents $\hat{R}_l$ (left panel) and $\hat{R}_t$ (right panel) as a function of *Re* for all surfaces considered in this study and at a constant normalized imposed depth of $\hat{H}$ = 8.3. For all surfaces, $\hat{R}_l$ and $\hat{R}_t$ increase with increasing *Re* as expected. The data also reveal similar behavior to that described regarding the

data of Figure 4-7. Namely, the hydraulic jump radius in the longitudinal direction displays only small dependency on the cavity fraction. At low *Re* the $\hat{R}_l$ data for all surfaces are nearly identical. At increasing *Re*, however, a small amount of spread in $\hat{R}_l$ becomes evident, with increasing F_c leading to an increase in $\hat{R}_l$. In the transverse spread direction the hydraulic jump radius for all patterned surfaces deviates (all smaller) from the smooth surface case for all *Re.* This deviation increases modestly with increasing F_c, showing the general importance of friction in the transverse direction, but that the relative spacing of the ribs and cavities has very little effect.

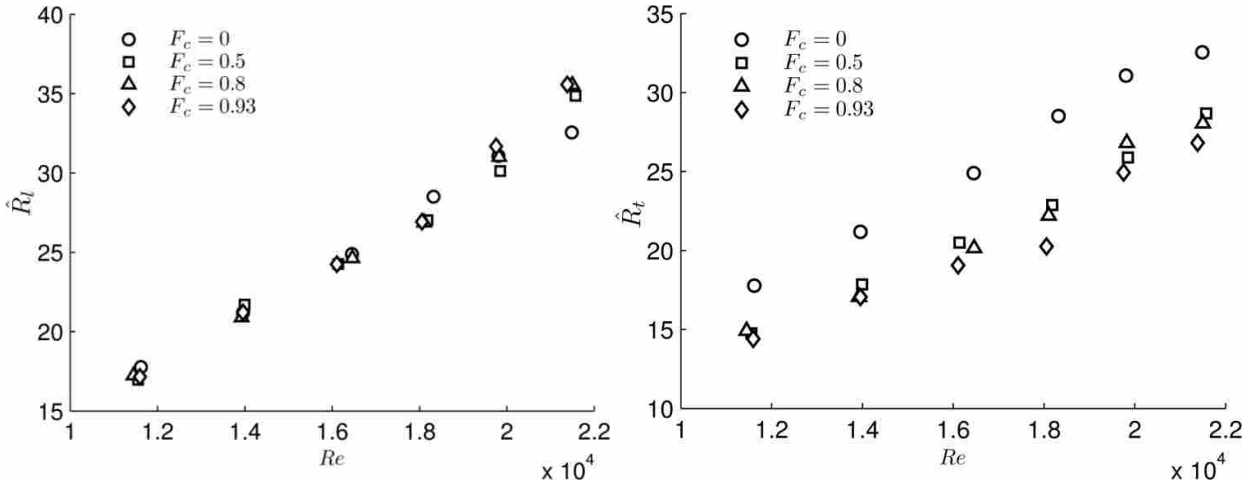

Figure 4-8. $\hat{R}_l$ (left) and $\hat{R}_t$ (right) as a function of *Re* for each surface considered and at $\hat{H}$ = 8.3.

Based on the $\hat{R}_l$ and $\hat{R}_t$ data of Figures 4-7 and 4-8, the eccentricity of the elliptical shaped hydraulic jump that results due to the patterned surfaces increases with increasing cavity fraction. This is indicative of a disparity in effective slip dependent upon the direction of the flow, which can be expected for flow over surfaces with anisotropic roughness. This is further demonstrated in Figure 4-9, where the ratio of the spread radii in the longitudinal and transverse

directions, R_l/R_t, is shown. The left panel provides R_l/R_t, as a function of $\hat{H}$ at a fixed Reynolds number, Re = 16200, and the right panel provides the same ratio as a function of Re at $\hat{H}$ = 8.3. In addition to increasing with F_c, the ratio R_l/R_t decreases with increasing $\hat{H}$. This observation is a result of the fact that as $\hat{H}$ increases, the radial location of the hydraulic jump decreases in both the longitudinal and transverse directions due to the greater downstream imposed depth which must be balanced by the momentum of the thin film. Consequently, for increasing $\hat{H}$ there is less area over which the thin film interacts with the surface and consequently, the influence of the disparity in surface resistance to the thin film motion in the two primary spreading directions is less pronounced. The behavior is more manifest for the F_c = 0.5 surface.The decrease in R_l/R_t becomes less dramatic as F_c increases because as the surface becomes less smooth, the influence of the ribs becomes greater, leading to larger R_l/R_t. As illustrated by the data of the right panel of Figure 4-9, increases in Re yields an increase in R_l/R_t. This behavior is a result of the same physical reasoning discussed above, namely increasing Re leads to a larger hydraulic jump radius and thus an increase in area over which the difference in friction in the longitudinal and transverse spread directions exerts greater influence.

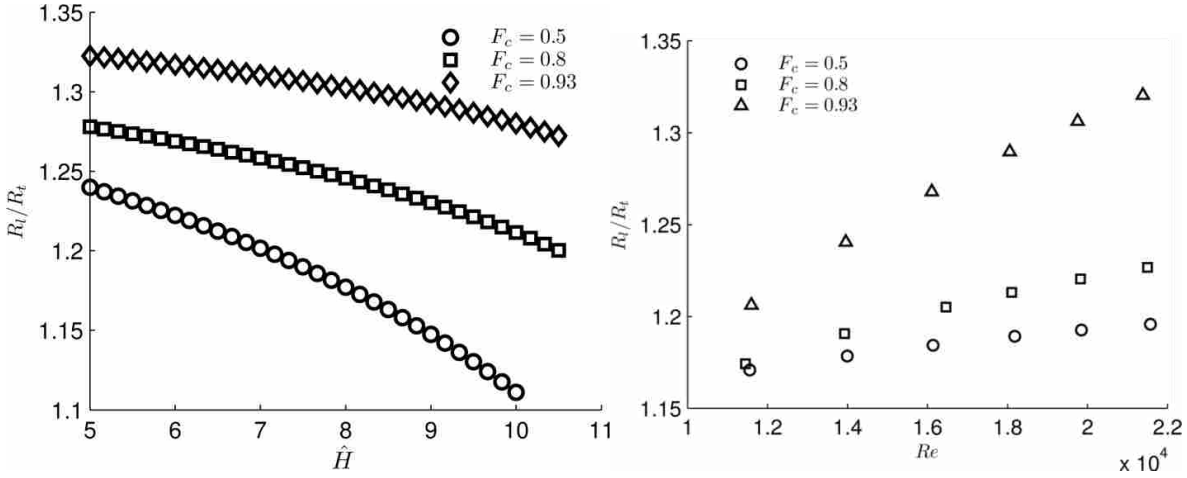

Figure 4-9. R_l/R_t as a function of $\hat{H}$ at Re = 16200 (left) and R_l/R_t as a function of Re at $\hat{H}$ = 8.3 (right) for F_c = 0.5, 0.8, and 0.93 surfaces.

We now consider the total area encompassed by the film region and its dependence on Re, $\hat{H}$, and F_c in order to better understand the overall effect surface patterning has on friction. This area was defined by assuming an elliptical shape for the $F_c = 0.5$ and 0.8 surfaces, yielding the ratio of the film region, A, to the area of the incoming jet, A_j, to be $\hat{A} = R_l R_t / a^2$. Due to the deviation from elliptical behavior for the $F_c = 0.93$ surface at $Re \geq 16200$, a different area was calculated for these cases. The distance in the transverse direction between the jet and the corner where the ellipse is truncated was measured for each frame. This distance along with the measured hydraulic jump location in the longitudinal and transverse directions is sufficient to calculate the area if the truncation in the longitudinal direction is assumed to be linear. Shown in the left panel of Figure 4-10 is $\hat{A}$ as a function of $\hat{H}$ for all Re explored and for $F_c = 0.8$. The right panel of the figure provides the same ratio as a function of Re at a fixed $\hat{H} = 8.3$ and for all surfaces considered. A / A_j for smooth surfaces is shown to be modestly larger than for patterned surfaces. This is to be expected, since R_l for patterned and smooth surfaces are nominally the same, yet R_t for patterned surfaces is notably smaller than for the corresponding smooth surface at the same conditions. For $F_c = 0.5$ and 0.8, where the transitions are elliptical, $\hat{A}$ appears to be independent of cavity fraction. This is probably due to the fact that the marginal increase in R_l with increasing F_c compensates for the decrease in R_t. For $F_c = 0.93$, the $\hat{A}$ data also appears to be nominally the same as the $F_c = 0.5$ and 0.8 data, However, at $Re \geq 18000$, as the shape of the ellipse changes for the $F_c = 0.93$ surface, the area ratio data begins to show departure from the other two patterned surfaces.

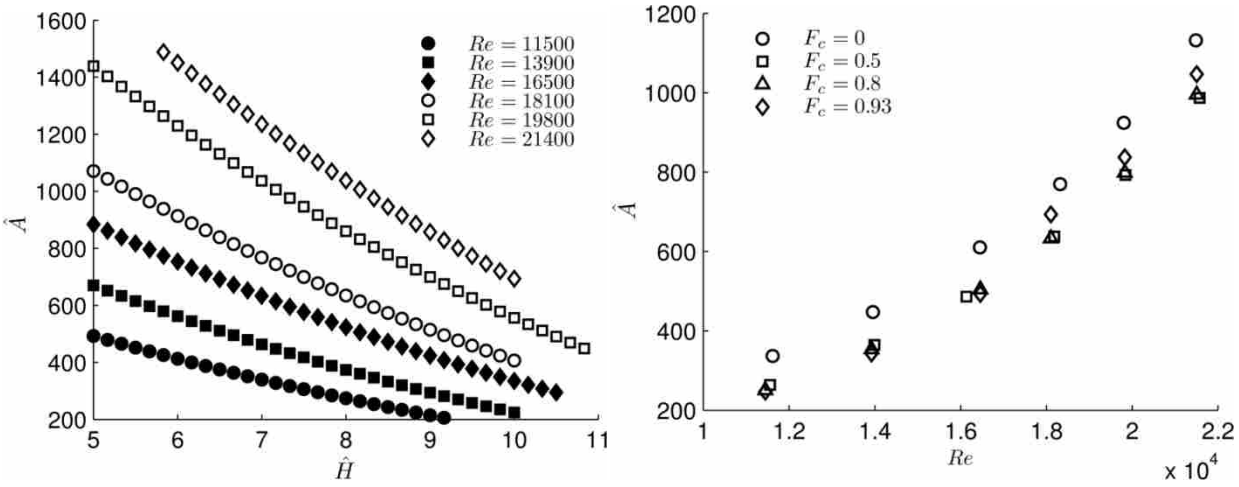

Figure 4-10. $\hat{A}$ as a function of $\hat{H}$ for the F_c = 0.8 surface and for all *Re* explored (left), and as a function of *Re* for $\hat{H}$ = 8.3 and for all surfaces (right).

From the $\hat{A}$ data, an equivalent jump radius, $R_{eq} = (A_j/\pi)^{1/2}$ was determined assuming the hydraulic jump was circular, rather than elliptical. In this manner the data can be compared to a previously presented analytical model that predicts the jump radius as a function of the jet parameters. The equivalent radius was then non-dimensionalized in the manner proposed by Watson and compared to Bush and Aristoff's analytical prediction [14, 20]. This non-dimensionalization is a result of the derived analytical solution, in which the hydrostatic force ($R_{eq}gH^2a^2/Q^2$), surface tension force ($2R_{eq}gH^2a^2/B_oQ^2$), and downstream momentum ($a^2/2\pi^2R_{eq}H$) are balanced with the momentum upstream of the hydraulic jump ($(R_{eq}/a)^3Re^{-1}$). The resulting comparison is provided in Figure 4-11, where the hydrostatic and surface tension, and downstream momentum terms are shown on the y-axis, and the upstream momentum is shown on the x-axis. It should be noted that an increase in H is manifested as an increase in the non-dimensional variable along the y-axis, and an increase in R_{eq} corresponds to an increase in the variable along the x-axis. Therefore, if a point lies to the right of the Bush model in the plot, R_{eq} is larger than the predicted value at a given downstream depth. The left panel shows data for F_c = 0.5, 0.8, and 0.93 at Re = 1.15x10^4 and 2.14x10^4. This demonstrates that there is no

significant dependence on F_c at low *Re*. While we see no noticeable difference between $F_c = 0.5$ and 0.8 surfaces at higher *Re* values, an increase is seen in R_{eq} for the $F_c = 0.93$ surface which reflects the increase in A_j observed in those cases. The right panel of Figure 4-11 shows each *Re* considered for the $F_c = 0.8$ surface. We find that for $Re \leq 18100$, the data follow the analytical prediction quite well at small expected jump radii. However, as the jump radii continue to decrease, the necessary downstream depth to produce such radii is much less than the Bush and Aristoff model predicts. This deviation occurs earlier and is more pronounced with increasing *Re*. A possible explanation for this deviation is that the jet is transitioning from a Type I to a Type II jump. Both Watson and Bush's correlations are based on Type I jumps, yet at increased downstream depths a Type II jump, which includes secondary eddy development at the jump, is expected. The height necessary to sustain a Type II jump should be less since some of the thin film momentum is balanced by this secondary recirculation region within the jump. In Bush's comparison to experimental data, this deviation from theory is seen, although it is less pronounced [20]. The more exaggerated departure from the model as compared to other studies may be due to the fact that the jet Data are shown for $F_c = 0.5$, 0.8, and 0.93 at $Re = 1.15\text{x}10^4$ and $2.14\text{x}10^4$ (left) and for all *Re* considered for $F_c = 0.8$ (right).radius, *a*, used in the current set of experiments was an order of magnitude smaller than many of the experiments reported by Bush. When this smaller *a* is factored into the non-dimensionalized momentum term, $(R_{eq}/a)^3 Re^{-1}$, the result is that the R_{eq} values in the current plot are much smaller than those found in Bush & Aristoff at similar values along the x-axis. Therefore, Type II jumps would not be expected until reaching smaller values along the x-axis of the current plot. For $Re > 18100$, the results diverge from Bush's model by indicating a larger R_{eq} than predicted at small *H*. This may be due to a transition to turbulence, and thus increased local momentum within the thin film at this *Re* range.

Because Watson's original model was based on a laminar boundary layer, the model is inadequate for predicting the jump location in the turbulent regime.

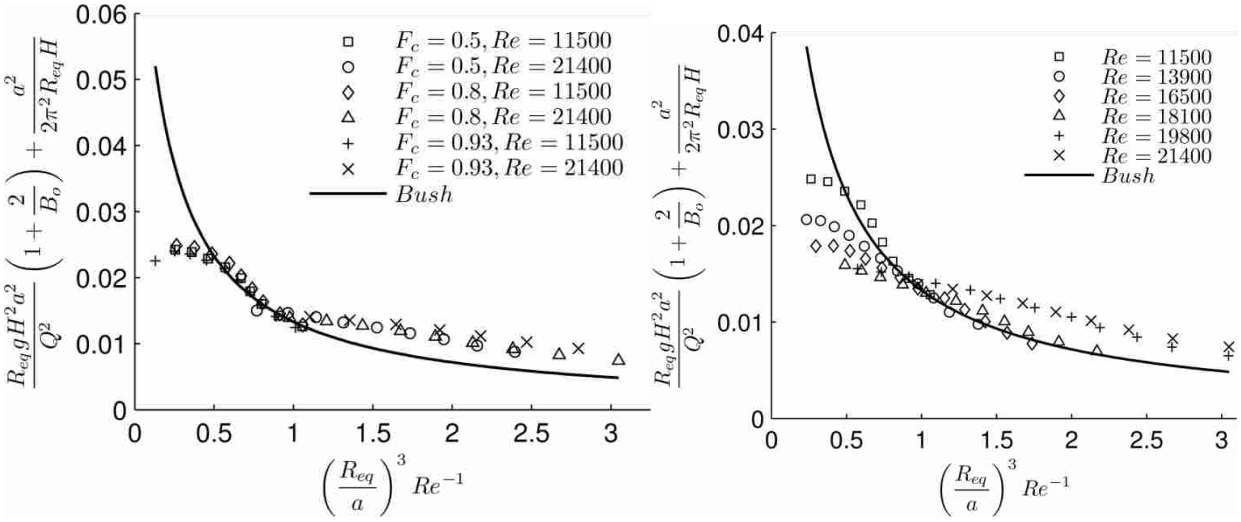

Figure 4-11. Comparison of the present experimental data to the analytical solution presented by Bush and Aristoff [20].

4.7 Conclusions

The circular hydraulic jump that results from jet impingement on smooth surfaces is well studied in the laminar flow regime, however, virtually no prior work has addressed similar phenomena on micro-scale patterned anisotropic surfaces. This paper has shown that when a liquid jet impinges on a surface with anisotropic surface patterning, the radial location and the shape of the hydraulic jump is significantly affected. In the case of a rib-and-cavity patterned surface, the resulting shape is elliptical, with the major axis running in the longitudinal direction, and the minor axis in the transverse direction. As the surface cavity fraction increases, the hydraulic jump increases slightly in the longitudinal direction and decreases in the transverse direction. Further, the eccentricity of the elliptical hydraulic jump increases with increasing Reynolds number, surface cavity fraction, and decreasing imposed downstream water depth.

Further, the total area of the supercritical thin-film region internal to the hydraulic jump is smaller for patterned surfaces as compared to smooth surfaces at similar conditions. This is due to the increased friction in the perpendicular rib-cavity direction. As the area of the thin-film region increases due to increasing *Re* or decreasing *H*, the eccentricity of the ellipse increases because the disparity in friction in the two primary spreading directions increases and exerts greater influence. The present data were compared to a previously described analytical model using equivalent radii based on thin-film area. The data shows good agreement with the model at small downstream depths and low Reynolds numbers. However, at higher Reynolds numbers the data shows significant deviation from the model predictions. Also, at large relative downstream depths the present data show large departure from the model prediction, with the departure increasing with Reynolds number.

5 HYDRAULIC JUMPS DUE TO JET IMPINGEMENT ON SUPERHYDROPHOBIC SURFACES EXHIBITING RIBS AND CAVITIES

This chapter is a manuscript which can be submitted for publication in a journal. As such, the relevant aspects of the literature review and experimental method discussed in Chapters 2 and 3 are summarized in this chapter. The paper has been formatted to fit the stylistic requirements of this thesis.

5.1 Abstract

This paper reports experimental results characterizing hydraulic jumps that result from liquid jet impingement on superhydrophobic surfaces patterned with alternating micro-ribs and cavities at known flow rates and downstream depths. The surfaces are characterized by the cavity fraction, which is defined as the width of a cavity divided by the combined width of a cavity and an adjoining rib. Four different surface designs were studied, with respective cavity fractions of 0 (smooth surface), 0.5, 0.8, and 0.93. Each surface design was studied in its natively hydrophilic state resulting in the cavities being flooded, as well as with a hydrophobic coating, which minimizes the amount of water entering the cavities and results in a superhydrophobic condition. The experimental data spans a Reynolds number range (based on the volume flow rate and jet radius) of 1.15×10^4 to 2.14×10^4 and a corresponding Weber number range of 3×10^2 to 1.05×10^3. As with impingement on smooth hydrophilic surfaces, the flow begins by moving outward from

the jet in a thin film. While smooth surfaces always result in circular transitions, for any patterned surface the flow exhibits an elliptical transition from the thin film, where the major axis of the ellipse is parallel to the ribs. Two mutually exclusive transitions occur which are dependent on Reynolds number, downstream depth, surface patterning and hydrophobicity. When the downstream depth is small and a superhydrophobic surface is used, the water is completely expelled from the surface, and the thin film breaks up into droplets due to surface tension interactions. When the downstream depth is large or the surface is hydrophilic a hydraulic jump exists. When comparing flow over superhydrophobic (coated) surfaces to patterned, hydrophilic (uncoated) surfaces, a general increase is seen in the radial location of the hydraulic jump in the direction of the ribs, while the change in location in the transverse direction appears to decrease with increasing Reynolds number.

5.2 Introduction

Superhydrophobic surfaces are created by combining micro-scale surface patterning with a hydrophobic coating. When water is placed on such a surface, the surface tension causes the the water resist flooding the cavities of the surface, thus creating a water-air interface over portions of the surface. When water flows over these surfaces, the result is an interaction with alternating no-slip interfaces over the solid surface, and virtually shear-free interfaces over the air trapped in the cavities. When air is trapped in the cavities of a superhydrophobic surface, the surface is said to be in the Cassie state. Consequently, the water flows over the surface with an effective slip at the macro-scale, thus reducing drag over the surface. When the cavities are flooded, it is said to be in the Wenzel state, which results in little or no drag reduction [1].

With the advent of micro-fabrication, many studies have been performed which study the flow of liquids over repeatably patterned superhydrophobic surfaces [1-9]. One pattern which has been commonly studied, both in laminar and turbulent cases, is alternating micro-ribs and cavities. These surfaces are characterized by the cavity fraction, which is defined as the width of a cavity, divided by the combined width of a cavity and adjoining rib ($F_c = w_c/w$). Studies in channel flow have found reduction in drag for both laminar and turbulent flow conditions over rib and cavity superhydrophobic surfaces. Greater reductions have been found with increasing F_c. The degree of drag reduction is also dependent on the direction of the flow with respect to the ribs and cavities. Flow in the longitudinal direction (parallel to the ribs) demonstrates less drag than that in the transverse direction (perpendicular to the ribs) [2, 3].

While channel flow and droplet behavior on superhydrophobic surfaces have been heavily studied [1-8], relatively little jet impingement research has been performed on superhydrophobic surfaces [9-10]. Therefore, the purpose of this study is to explore the dynamics of a liquid jet impinging on a superhydrophobic surface. When a vertical liquid jet strikes a smooth horizontal surface, the liquid subsequently spreads radially in a circular thin film as illustrated in Figure 5-1 and described by Watson in his seminal paper [14]. This continues until a hydraulic jump occurs, which is characterized by a sudden increase in liquid depth and corresponding decrease in average velocity of the fluid.

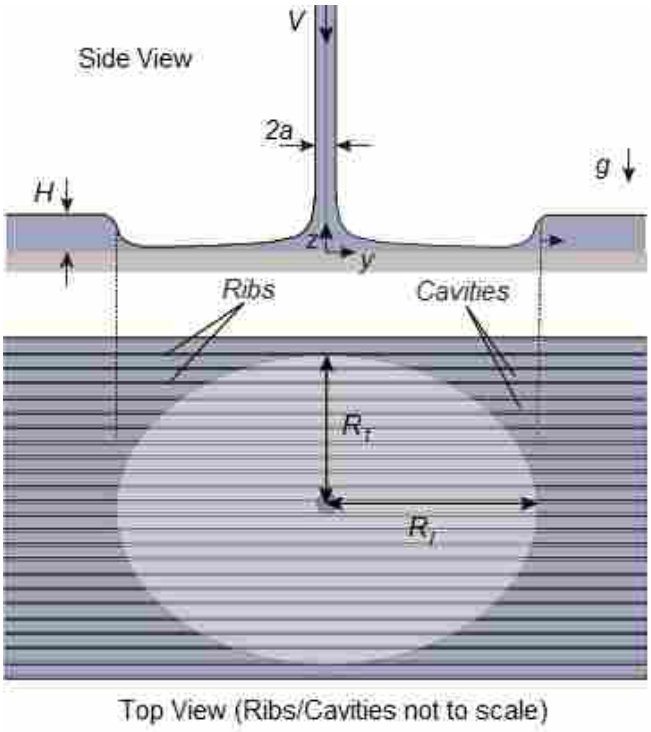

Figure 5-1. Critical dimensions of the hydraulic jump on a rib and cavity patterned surface. Rib patterning is not to scale.

Jet impingement on a rib and cavity superhydrophobic surface behaves differently than on a smooth surface, due to the strong anisotropy and introduction of slip over the surface. For a surface that exhibits anisotropy, the boundary layer thickness, film thickness, and film surface velocity all exhibit spatial variation in the tangential coordinate and the jump dynamics are no longer symmetric. Since the location at which the hydraulic jump occurs depends on a local balance between fluid momentum and the hydrostatic and surface tension forces, frictional variations due to surface roughness or texturing will directly affect the shape and location of the hydraulic jump. As a result, impingement on rib and cavity surfaces results in an elliptical transition where the major axis is aligned with the longitudinal direction, concomitant with lower friction in that direction. Maynes et al. studied jet impingement on surfaces with alternating micro-scale ribs and cavities patterned onto the surfaces [9]. This study considered Wenzel and

Cassie states. The width of the cavities in this study ranged from 32 – 37 μm and the cavity depth was nominally 15 μm. For these experiments a downstream water depth was not imposed. This resulted in noteworthy differences in transition types. Impingement on the Cassie state surfaces caused an elliptical transition and instead of the classical hydraulic jump, the film broke into filaments or droplets due to surface tension at a specific radial location. Analysis of the data found that this transition occurred where the local Weber number, $We_s = \rho u h/\sigma$, was near unity, where u and h were the local average film velocity and thickness, respectively. This was similar to the findings of Lin and Jiang [13], where an absolute instability occurred at a $We_s = 1$ for a radially expanding liquid sheet. An elliptical hydraulic jump also occurred on Wenzel state surfaces. The Cassie state surface resulted in a transition dominated by surface tension, the dynamics of which differs substantially from the hydraulic jumps associated with the Wenzel state. Therefore, the Cassie state and Wenzel state transitions could not be compared to quantitatively determine drag reduction.

Dressaire et al. investigated experimentally the influence of post arrays on the location and shape of the hydraulic jump in the Wenzel state [11, 12]. The posts were fabricated using standard micro-fabrication methods and were 100 μm in diameter and ranged from 200 to 400 μm in height. The surfaces were hydrophilic so that water completely wet the region between posts. Their results showed that surfaces patterned with posts result in polygonal and star shaped hydraulic jumps. Different shapes were achieved depending on the distribution pattern of the posts on the surface. Kibar et al. studied the dynamics of an inclined jet impinging on a randomly patterned vertical surface with a jet Weber number ranging from 5 to 650 [10]. As a result of the high degree of hydrophobicity, the jet reflects and subsequently jumps off of the surface. They reported a 40% drag reduction as the contact angle increased from 145° to 167°.

This paper reports experimental results characterizing hydraulic jumps that form due to perpendicular liquid jet impingement on rib and cavity superhydrophobic surfaces when a downstream depth is imposed. To the authors' knowledge this is the first paper to report on this scenario. Surfaces are fabricated using standard photolithographic processes and the Cassie-state surfaces are subsequently coated with Teflon while the Wenzel-state surfaces are natively hydrophilic silicon. Four different surface designs were studied, with respective cavity fractions of $F_c = 0$ (smooth surface), 0.5, 0.8, and 0.93. The radial jump locations in the longitudinal and transverse directions are presented for the above surfaces and for imposed downstream depths ranging from $H/a = \hat{H} = 5$ to 12.5, where H is the depth of water downstream of the hydraulic jump. The Reynolds number ($Re = Q/\nu a$) range explored was 1.15×10^4 to 2.14×10^4, where Q is the volume flow rate, ν is the kinematic viscosity of the fluid, and a is the jet radius. A companion paper (Chapter 4) has discussed the effect of the flooded micro-scale rib/cavity structures by comparing the jump radius to data obtained for a smooth surface at the same flow and downstream depth conditions [23]. This paper compares the location of the hydraulic jump for non-wetting surfaces to the wetting surfaces at similar conditions. The total area encompassed by the thin film region is also calculated and the micro-scale patterned surfaces and the smooth surface data are compared.

5.3 Experimental Method

The test apparatus, a schematic of which is shown in Figure 5-2, consisted of a vertically oriented nozzle of radius $a = 0.6$ mm located 20 mm above the horizontal test surface of interest. The surface was placed on an aluminum plate 20 cm in diameter that was suspended in a 1 m diameter reservoir filled with deionized water. The elevation of the plate relative to the water

surface level was adjustable, and thus H, was easily varied. The downstream water depth was measured using a needle micrometer stage, with a measurement uncertainty of $\pm 4 \times 10^{-5}$ m. Two CCD video cameras were aligned to capture the jump diameter in the longitudinal and transverse directions respectively. Since neither camera was aligned orthogonally with respect to the plate, the only diameter they accurately measured was the direction in which it was aligned. Therefore, the only radii acquired were those along the major and minor axes of the elliptically shaped transition. The nozzle was fed by a water filled plenum with an adjustable pressure to achieve the desired flow rate.

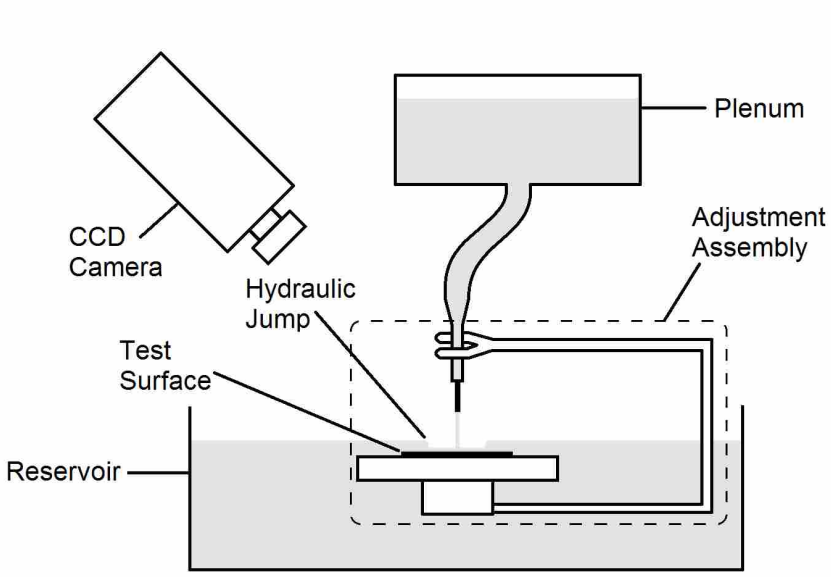

Figure 5-2. Schematic of experimental setup. The adjustment assembly is translated vertically to achieve a desired initial depth.

Three replicate experiments were performed on each combination of jet velocity and surface type, and the radial jump locations from the three replicates were then averaged. The procedure was as follows. The jet velocity was determined by measuring the time required to collect a known volume of water. The average uncertainty for velocity measurements was

±1.2%, which resulted in a Reynolds number uncertainty of ±3.6%. For wetting surfaces, the water depth on the surface was adjusted to a nominal value of 2.8 mm prior to initiating the flow. Non-wetting surfaces exhibited a minimum depth required to maintain a hydraulic jump. The minimum depth was determined prior to testing each Weber number, and the initial depth was adjusted accordingly. When the flow began, the large (essentially constant diameter) reservoir collected the water, and thereby the downstream depth increased linearly with time at a relatively slow rate. The video cameras were started before the impingement process began and ended after the jet had been turned off so that the timing of the initial jet impingement and the end of the flow could be recorded. The test was conducted until the downstream depth became too large, and the hydraulic jump collapsed inward on the incoming water jet. The water was immediately turned off, and a final downstream depth was measured.

A computer program was developed that identifies and tracks the radial position of the hydraulic jump for each frame of the video using an edge-detection algorithm, which used the brightness values in a window centered on the average jump location of the five previous frames. The lighting was set up such that a dark shadow occurs at the hydraulic jump, as can be seen in Figure 5-7. The location of this jump was determined by taking the derivative of the brightness values and finding the maximum change of this derivative from light to dark in the jump region. The uncertainty associated with identifying the radial position of the hydraulic jump was ±4 pixels, based on the average width of the dark region associated with the hydraulic jump. The pixel measurement was then mapped to physical length scales by calibrating the videos based on an image taken of a reference scale after each test. This resulted in a nominal uncertainty of each instantaneous radial measurement of ±3%.

The downstream depth for each frame was then determined by a linear interpolation between the depths measured at the first and last frames when the jet was seen to be impinging on the surface. The validity of this method was verified experimentally by running the water at regular intervals, allowing the reservoir to fill to a fraction of the level taken during an actual test, and measuring the change in height to confirm that it was still linear. The test resulted in a linear trend to within ±1% uncertainty.

Six jet velocities were explored for each surface, yielding a jet Weber number ($We = \rho V^2 a/\sigma$) range of $3\text{x}10^2$ to $1.05\text{x}10^3$ where ρ and σ are the liquid density and surface tension respectively, V is the velocity and a is the radius of the jet. The corresponding Reynolds number ($Re = Q/\nu a$) range is given as $1.15\text{x}10^4$-$2.14\text{x}10^4$ where Q is the volume flow rate of the jet, and ν is the kinematic viscosity of the fluid.

In addition to the experiments performed above, a number of images have been captured using a high speed camera for visualization purposes. These images were captured at a wide range of Reynolds numbers and downstream depths. The images are illuminated by a light source with a diffuser, and the images are taken at a frame rate of 500 frames per second.

5.3.1 Surface Fabrication

Test surfaces were fabricated using 101.6 mm diameter silicon wafers using standard photolithographic processes. Since silicon is natively hydrophilic, these patterned surfaces were used to test the Wenzel state. To achieve the Cassie state, the surfaces were subsequently coated with a thin layer of chromium and Teflon. Three surfaces were used with cavity fractions of F_c = 0.5, 0.8, and 0.93. Representative SEM images of the surfaces used are shown in Figure 5-3. The

rib height was nominally 15 μm, for each surface. Polished silicon wafers were used for the smooth surfaces.

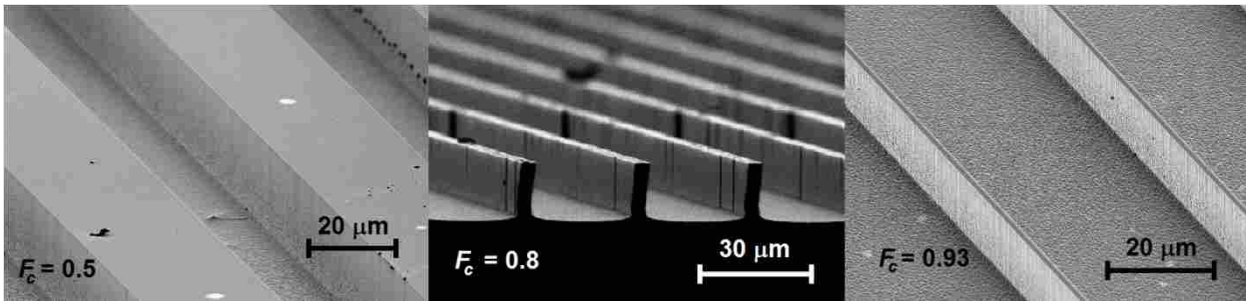

Figure 5-3. SEM images of F_c = 0.5 (left), 0.8 (center), and 0.93 (right) surfaces

Table 5-1 shows the dimensions and corresponding cavity fraction of each surface used, as well as the receding (θ_r) and advancing (θ_a) contact angles for the hydrophilic (uncoated) and superhydrophobic (coated) cases. The advancing contact angles are acquired by placing a droplet on the surface with a needle continually adding volume to the droplet until the boundary of the droplet expands along the surface. The angle between the surface and the edge of the droplet is then measured while the droplet grows. Receding contact angles are measured by drawing the liquid in the droplet back into the needle until the edge of the droplet recedes along the surface and measuring the angle. All of the coated surfaces maintain hydrophobic contact angles, with all patterned surfaces resulting in contact angles in excess of 120°, thereby characterizing them as superhydrophobic. The advancing contact angles in the transverse direction are larger than those in the longitudinal direction. Conversely, the receding transverse contact angles are smaller than the receding contact angles in the longitudinal direction. As F_c increases, θ increases in concordance with Cassie's law. In the hydrophilic, wetting cases, the advancing contact angles were less than 90° as expected. These angles are much smaller in the in the longitudinal direction than in the transverse direction. This is because as a droplet is placed on the surface, the water

wicks into the channels, pulling the droplet in the longitudinal direction. When the water in the droplet is drawn back into the needle to measure the receding contact angle, the water in the channels is not drawn out, and the droplet does not recede. Thus, each hydrophilic receding contact angle is measured as 0°.

Table 5-1. Cavity fraction (F_c), with the corresponding module width (w), and cavity width (w_c) of each surface tested.

F_c	w (mm)	w_c (mm)	Coated (Non-Wetting)		Uncoated (Wetting)	
			θ_a (°) Long/Trans	θ_r (°) Long/Trans	θ_a (°) Long/Trans	θ_r (°) Long/Trans
0	None	None	125	109	87	49
0.5	60	30	140/168	127/121	10/81	0/0
0.8	40	32	150/168	140/133	15/43	0/0
0.93	40	37.2	158/168	146/144	13/62	0/0

5.4 Results

5.4.1 General Observations

Unless otherwise indicated, all results correspond to jet impingement on coated hydrophobic or superhydrophobic surfaces. During the impingement process, three flow regimes are possible with the extremes corresponding to the imposed downstream water depth being either too shallow or too deep. At shallow water depth, when the jet impinges on the surface the resulting momentum exchange expels all water from the surface. This occurs due to the pull of surface tension and is aided by the superhydrophobic properties of the surface and the shallowness of the water layer. This results in surface tension based transitions where the downstream water depth vanishes and the thin film breaks up into droplets. This is the regime that has been explored previously by Maynes et al. [9], and the dynamics are essentially identical

to those of jet impingement on an unimmersed superhydrophobic surface. The critical height where this occurs is shown in Figure 5-4 as a function of the jet Reynolds number for the F_c = 0.5, 0.8 and 0.93 surfaces, where the solid symbols correspond to this shallow water limit. The critical height for all three cavity fractions is nominally the same, and in general increases linearly with increasing jet Reynolds number.

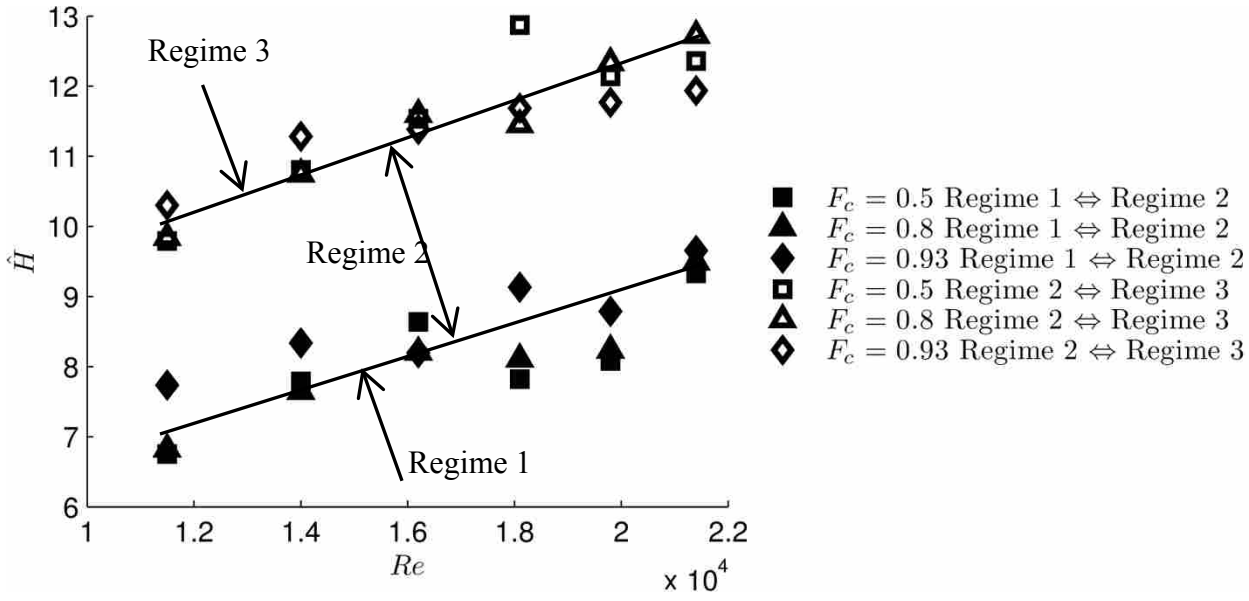

Figure 5-4. The height at which the hydraulic jump breaks up and collapses. Regime 2 is the regime focused on in this study.

Within Regime 1, there are several *Re*-dependent transition types. Qualitative high speed images of these transitions can be seen in Figure 5-5. The left panel depicts a low-*Re* situation where an elliptical transition occurs, and the thin film breaks into a filament in which the water moves preferentially along the edge of the ellipse in the longitudinal direction. Once the filaments meet at the location of the major axis, the water then moves off the surface along the ribs. At high *Re,* the film breaks into droplets and continues to move radially outward, which can be seen in the right panel of Figure 5-5. It should be noted that while the dynamics between these

cases are different, no downstream depth is apparent for any *Re*. A more detailed description of these transitions was given by Maynes et al. [9].

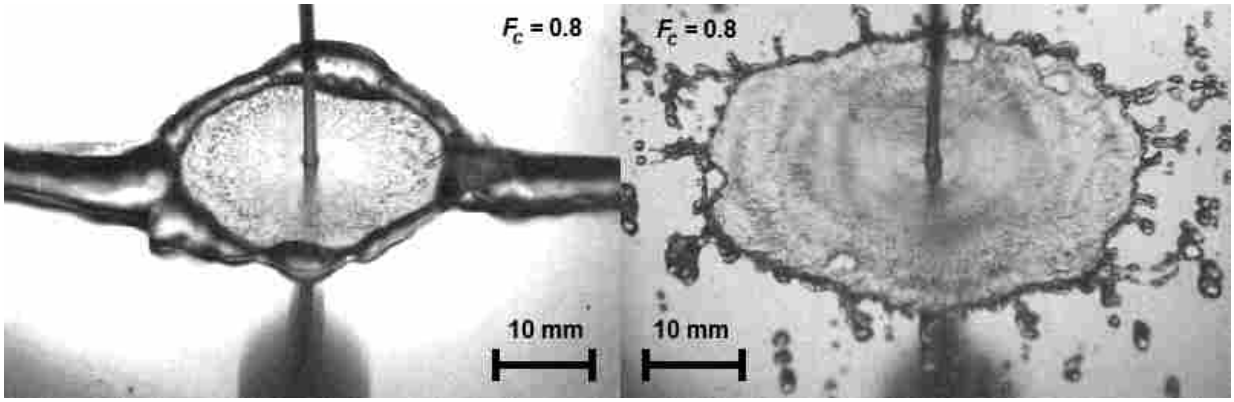

Figure 5-5. Images of Regime 1 transitions on superhydrophobic surfaces with F_c = 0.8 at *Re* = 12400 (left), and *Re* = 20400 (right)

At larger water depths (Regime 3), the hydrostatic force is too great and momentum of the jet is insufficient to maintain a stable thin film region. As a result, a hydraulic jump repeatedly forms and collapses into the jet in a pulsatile fashion due to surface waves. Figure 5-6 shows six images which illustrate one period in the pulsatile progression of Regime 3 flow. The non-dimensional downstream depth at which Regime 3 occurs can be seen in Figure 5-4, and is demarcated by the open symbols. If the depth of the water is allowed to increase further, the thin film eventually fails to form, and the jet plunges into the deep water, entraining air.

Regime 2 occurs at intermediate downstream depths as seen in Figure 5-4. Within this $\hat{H}$ range, the jet initially forces the water off the surface, but the depth of the downstream water is sufficient to immediately collapse back to where equilibrium is met and a stable hydraulic jump eventually forms. Regime 2 is the primary focus of this paper, wherein a thin film exists and the radius of the hydraulic jump is dependent upon *Re* and $\hat{H}$. Figure 5-7 shows two examples of the shapes of the various jump transitions observed. The structured F_c = 0.5 and 0.8 surfaces

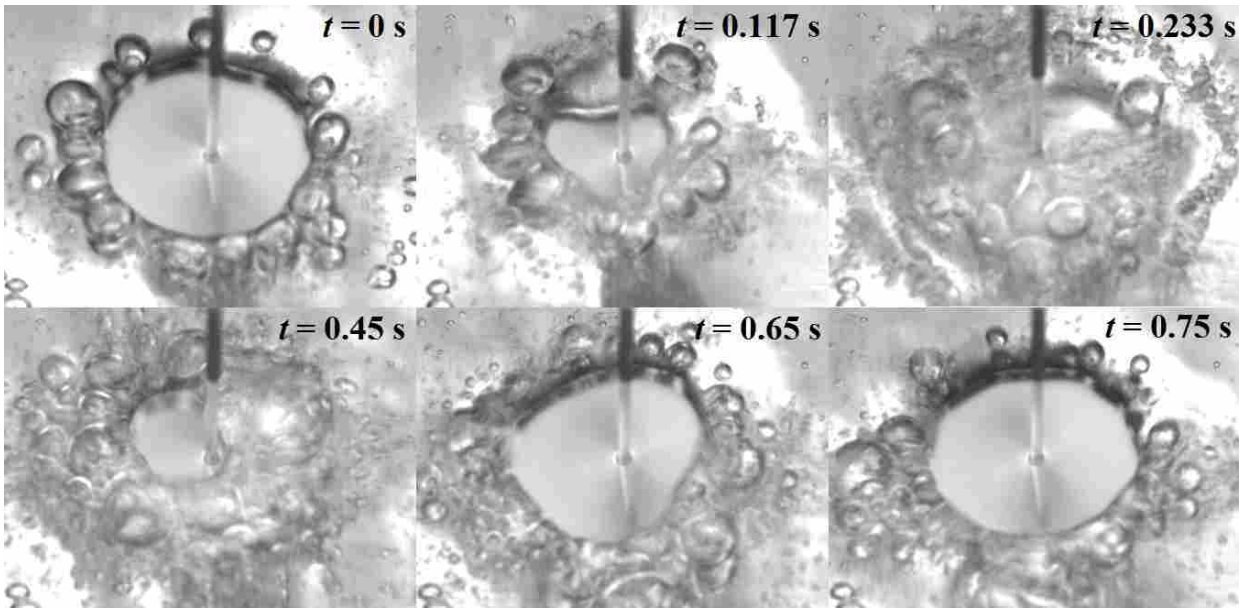

Figure 5-6. Images showing the progression of a hydraulic jump collapsing and reforming when the downstream depth is too large for the jet momentum to maintain a stable thin film region (Regime 3).

demonstrate nominally elliptical transitions like that shown in the left panel of Figure 5-7, where the major axis runs in the longitudinal direction (along the ribs). For $F_c = 0.93$, an alternate transition shape is observed at large downstream depths and Reynolds numbers. When $Re \leq 1.4\text{x}10^4$, the jump shape is still elliptical. However, for $Re > 1.62\text{x}10^4$, the ellipse truncates in the longitudinal direction, and exhibits more of a rectangular or polygonal shape, as can be seen in the right image of Figure 5-7.

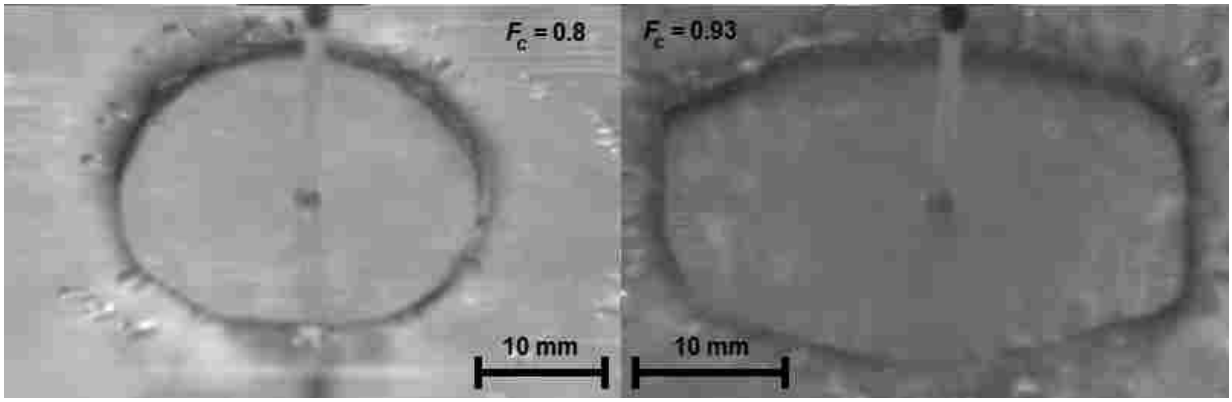

Figure 5-7. Images of hydraulic jumps in Regime 2 with $F_c = 0.93$, $\hat{H} = 9.3$ and $Re = 1.15\text{x}10^4$ (left), and with $F_c = 0.93$, $\hat{H} = 10$ and $Re = 2.14\text{x}10^4$ (right)

Figure 5-8 shows the longitudinal (along the ribs) and transverse (perpendicular to the ribs) hydraulic jump radius data as a function of $\hat{H}$ for a Fc = 0.8 surface where Re = 18100. Results are shown for Regime 1, which is demarcated with lines, while the open symbols show measurements of the hydraulic jump radius for experiments that began in Regime 2. For these experiments the downstream depth was allowed to increase. If an experiment begins as a Regime 2 flow with a stable hydraulic jump, and the downstream depth is decreased instead, the hydraulic jump radius increases and the local We_s at the hydraulic jump decreases until it approaches unity. Near this critical downstream depth, the instability described by Maynes et al. [9] occurs and the film begins to break up into droplets. At this point, the surface tension causes the water to pull off of the surface, and the film transition is independent of $\hat{H}$ at all downstream depths lower than this critical point.

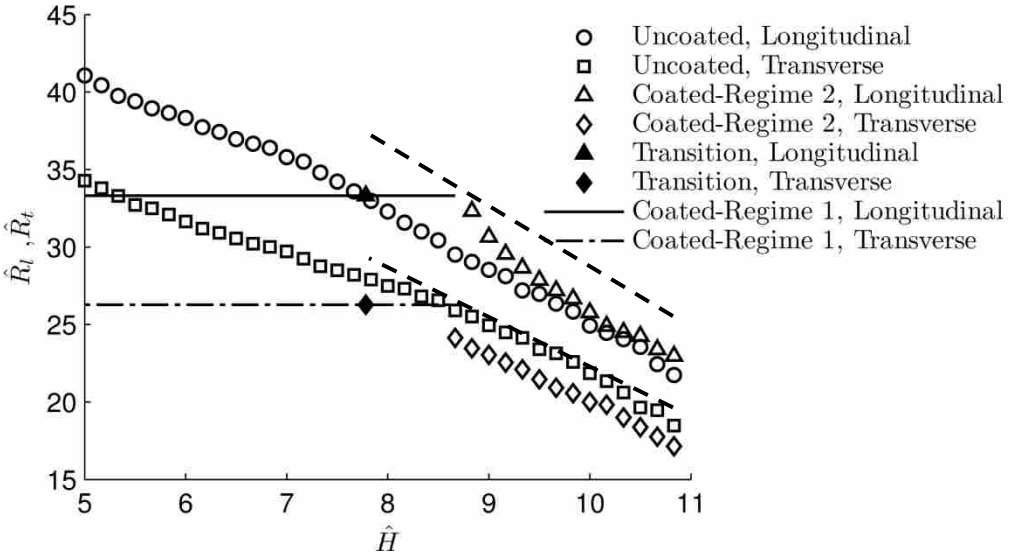

Figure 5-8. Longitudinal and transverse transition radii vs $\hat{H}$ for coated and uncoated surfaces where F_c = 0.8 and Re = 18100.

The transition point from Regime 2 to Regime 1 is also shown in Figure 5-8, demarcated as solid symbols. These were acquired by starting the flow at a downstream depth that resulted in

Regime 2 flow and decreasing the downstream depth until the water wicked off the surface, signifying transition to Regime 1. At this point, the jet flow was immediately suspended and the downstream depth was measured. The instantaneous depth measurements were unattainable while the jet was impinging. Thus, as the downstream depth was decreased the exact value was unknown. Since the initial momentum of the jet as impingement begins provides a transient instability, the minimum depth at which Regime 2 can begin is larger than the minimum depth at which it can be maintained. Therefore, a gap exists between the data collected for the Regime 2 data for coated surfaces, and the transition points from Regime 2 to Regime 1. The dashed lines running through the Regime 2 results show that if the trends are extrapolated, the transitions fall reasonably close to the approximate location where the Regime 2 and Regime 1 trends would meet. Also shown in Figure 5-8 are the hydraulic jump radii for uncoated surfaces. Since the flow over these surfaces remains in the Wenzel state, transitions do not experience Regime 1 type of behavior at any $\hat{H}$.

Figure 5-9 displays the non-dimensional hydraulic jump radius in the longitudinal ($R_l/a = \hat{R}_l$) and transverse ($R_t/a = \hat{R}_t$) directions at which transition from Regime 2 to Regime 1 occurs as a function of Re for a $F_c = 0.8$ surface. This data is demarcated with open symbols, and is compared to the $\hat{R}_l$ and $\hat{R}_t$ values for unimmersed surface tension transitions (Regime 1) as performed by Maynes et al. [9]. In general, $\hat{R}_l$ for the transition data is nominally the same as the data provided by Maynes, while $\hat{R}_t$ is slightly greater than for the unimmersed data. This difference may be due to a slight difference in the fabrication of the surfaces used. Both surfaces are coated with Teflon, but the surfaces used by Maynes et al. [9] used aluminum as a base for the Teflon, whereas the presently used surfaces are coated with chromium. Chromium has repeatedly resulted in better adhesion of the Teflon, and increased hydrophobicity. General

agreement with Maynes et al. [9] is expected because the transition observed when Regime 1 is reached is a result of surface tension, and the dynamics are identical.

5.4.2 Hydraulic Jump Location

Figure 5-10 presents the hydraulic jump locations of both coated and uncoated surfaces as a function of $\hat{H}$ at a fixed Reynolds number of Re = 16200. As expected, the jump radius decreases with increasing $\hat{H}$ due to increasing hydrostatic force. An increase in $\hat{R}_l$, and to a lesser extent $\hat{R}_t$ is observed for the coated surfaces as compared to the uncoated surfaces. This will be considered in greater depth at a later point in the paper.

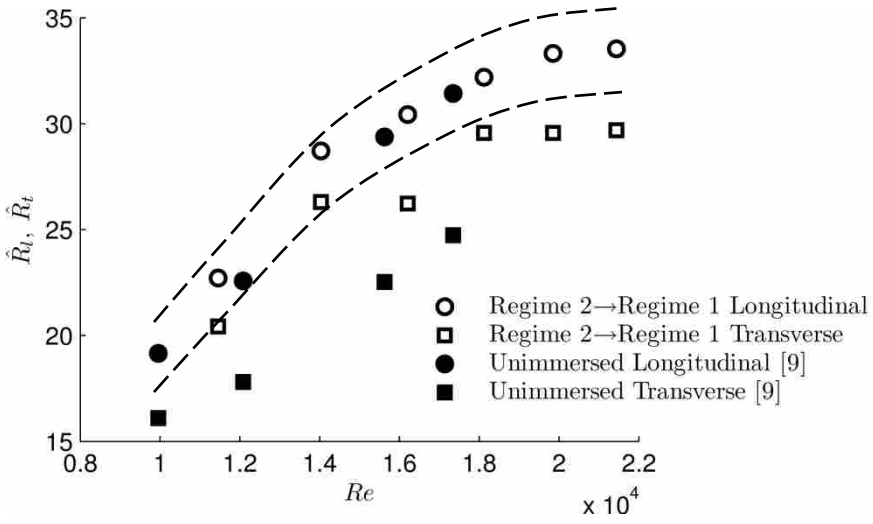

Figure 5-9. $\hat{R}_l$ and $\hat{R}_t$ as a function of *Re* for F_c = 0.8 surface where transition from Regime 2 to Regime 1 occurs, compared to previously acquired unimmersed transition data of Maynes et al. [9]

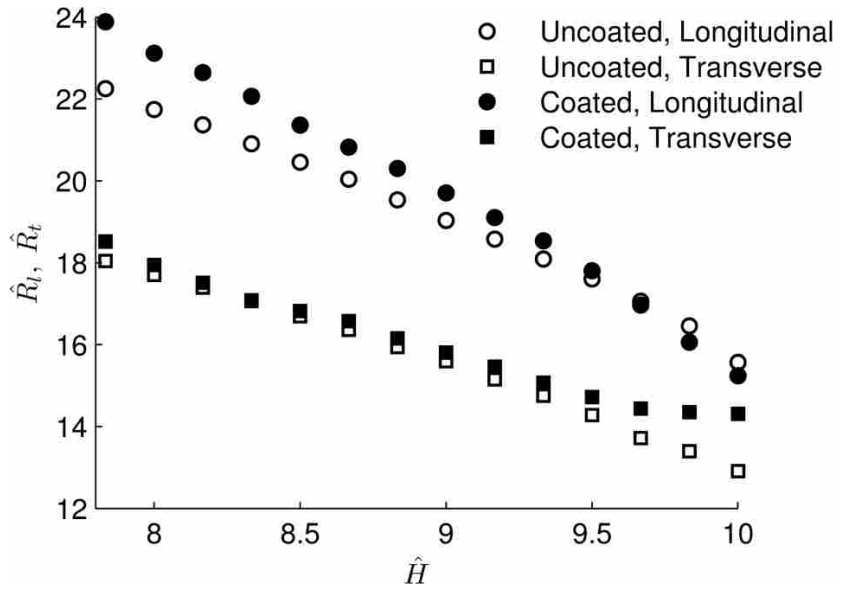

Figure 5-10. $\hat{R}_l$ and $\hat{R}_t$ vs $\hat{H}$ for wetted and unwetted cases of F_c = 0.5 where *Re* = 18100

Figure 5-11 features $\hat{R}_l$ and $\hat{R}_t$ as a function of *Re* at a fixed $\hat{H}$ value of 10. The jump radius increases as the momentum increases (increasing *Re*), as would be expected. This figure also shows that for increasing *Re*, an increase in $\hat{R}_l$ and $\hat{R}_t$ is observed due to the increase in the momentum of the thin film. Also, for all cases $\hat{R}_l$ is greater than $\hat{R}_t$ due to increased slip in the longitudinal direction. At similar $\hat{H}$ and *Re*, $\hat{R}_l$ for the coated surfaces is larger than for uncoated surfaces. However, there is no significant trend in the difference in $\hat{R}_t$ for the coated and uncoated surfaces. The increase in $\hat{R}_l$ indicates that slip in the longitudinal direction increases when the surface is superhydrophobic. While it is possible that slip increases in the transverse direction, there is no indication of it in the $\hat{R}_t$ data. This is possibly due to the loss of momentum that likely occurs due to redirection of flow associated with longer slip lengths in the longitudinal direction. The trends found in Figures 5-10 and 5-11 are representative of all cavity fractions and

flow rates explored in this study. While data for F_c = 0.8 and 0.93 are shown here, comprehensive results for all scenarios considered are tabled in Appendix A.

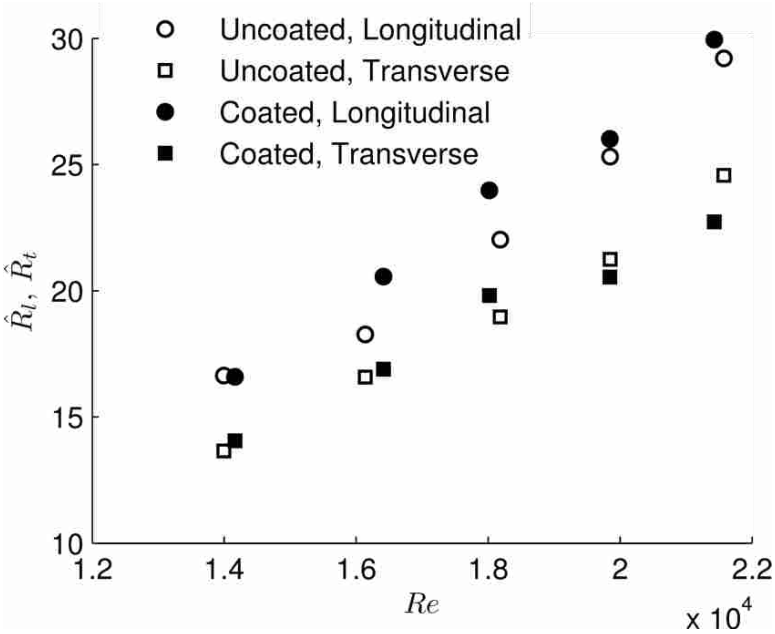

Figure 5-11. $\hat{R}_l$ and $\hat{R}_t$ vs *Re* of F_c = 0.5 surfaces for wetted and unwetted cases where $\hat{H}$ = 10 in the longitudinal and transverse directions

5.4.3 Longitudinal-to-Transverse Radius Ratio

In Figure 5-12, we investigate the ratio of the coated vs. uncoated jump radii as a function of *Re* in the longitudinal and transverse directions This is done at corresponding cavity fractions and at a fixed $\hat{H}$ value of 9.0. In the longitudinal direction, R_l is consistently greater for coated surfaces than for uncoated surfaces. There is no apparent trend in $R_{l,coated}/R_{l,uncoated}$ as *Re* increases, but the transverse results show a decrease with increasing *Re* to the extent that $R_{t,c}/R_{t,u}$ < 1 at high *Re*. Also, while the results in Figure 5-12 are inconsistent with respect to F_c in the longitudinal direction, $R_{t,c}/R_{t,u}$ appears to decrease as F_c increases. This would seem to indicate a transition to turbulence at higher *Re* and F_c. Studies have been performed to investigate turbulent

flow over rib-and-cavity superhydrophobic surfaces, and have found that while drag reduction is achieved in the longitudinal direction, the transverse direction exhibits an increase in drag [4, 6, 8]. This is presumably due to the fact that for transverse flow, the ribs would enhance spanwise turbulent mixing, and thereby increase the drag. Transition to turbulence may also explain the decrease in $R_{t,c}/R_{t,u}$ with increasing F_c explained by transition to turbulence. Since increasing F_c would increase slip lengths and may trip the flow to turbulence earlier than it otherwise would.

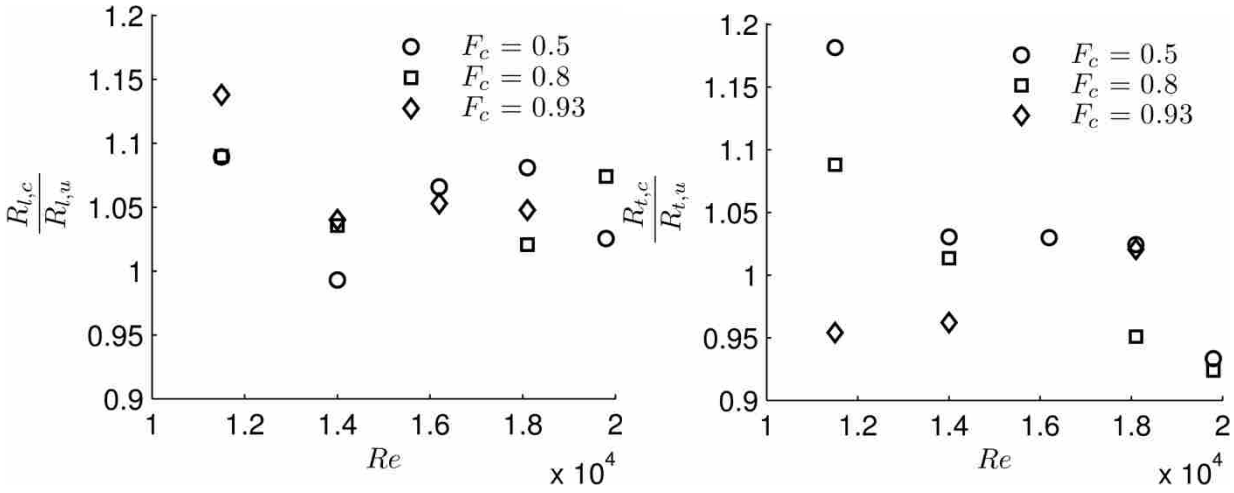

Figure 5-12. Ratio of coated to uncoated hydraulic jump radii as a function of *Re* at $\hat{H}$ = 9.0 in the longitudinal (left) and transverse (right) directions

An important factor to consider with anisotropic patterning is the difference in the flow interaction between directions of varying slip lengths. A representative measure of this difference is the ratio between the radial locations of the longitudinal and transverse jumps, R_l/R_t. Figure 5-13 shows an example of R_l/R_t as it relates to $\hat{H}$ for Re = 14000 (left) and Re = 18100 (right). For all F_c, a gradual decrease was observed in R_l/R_t with increasing $\hat{H}$. This decrease was more pronounced for the F_c = 0.93 surface. This was expected because as $\hat{H}$ increases, the overall jump radius decreases, and therefore the area of the thin film decreases.

Since this is the area over which friction affects the flow, the disparity in velocity between the longitudinal and transverse directions decreases.

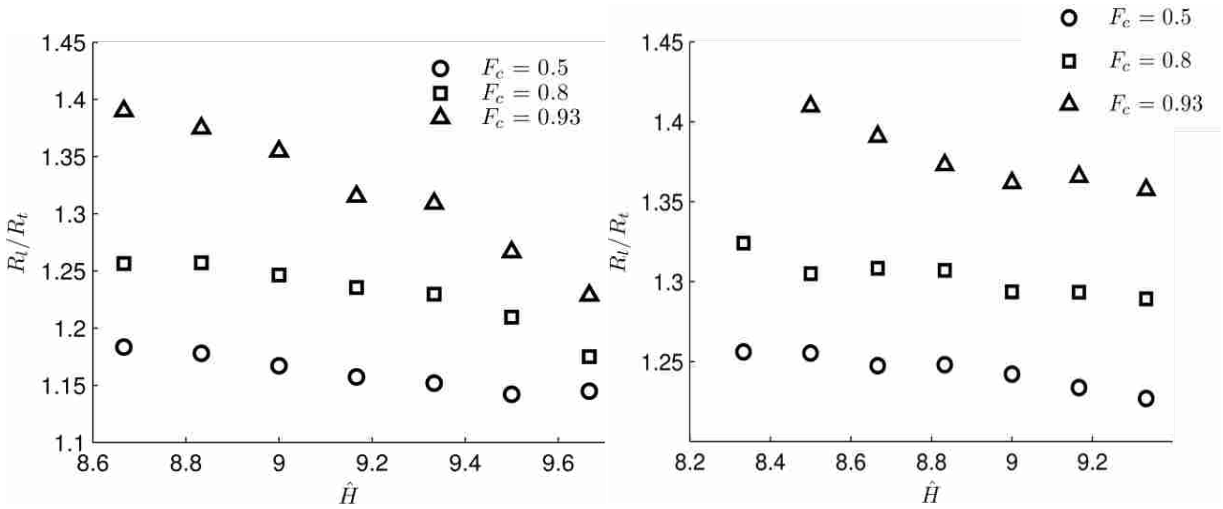

Figure 5-13. R_l/R_t as a function of $\hat{H}$ for coated surfaces at Re = 14000 (left) and Re = 18100 (right) for each F_c

Figure 5-14 displays R_l/R_t as a function of Re at $\hat{H} = 9$, for each F_c. When analyzing R_l/R_t across Re, it was seen that the results were dependent upon F_c. For F_c = 0.5 and 0.8, R_l/R_t increases steadily as Re increases, which was to be expected because as Re increases the area over which the slip gradient can act increases, although the overall slip is minimal. With greater slip effects achieved by $F_c = 0.93$, there is noticeable variation in the individual points and there is no consistent trend with respect to Re. This may be due to the development of turbulence associated with the increased momentum over the slip surface. Despite non-uniform changes as related to each Re, R_l/R_t increases with increasing F_c, due to larger relative slip in the longitudinal direction compared to the transverse direction for larger F_c.

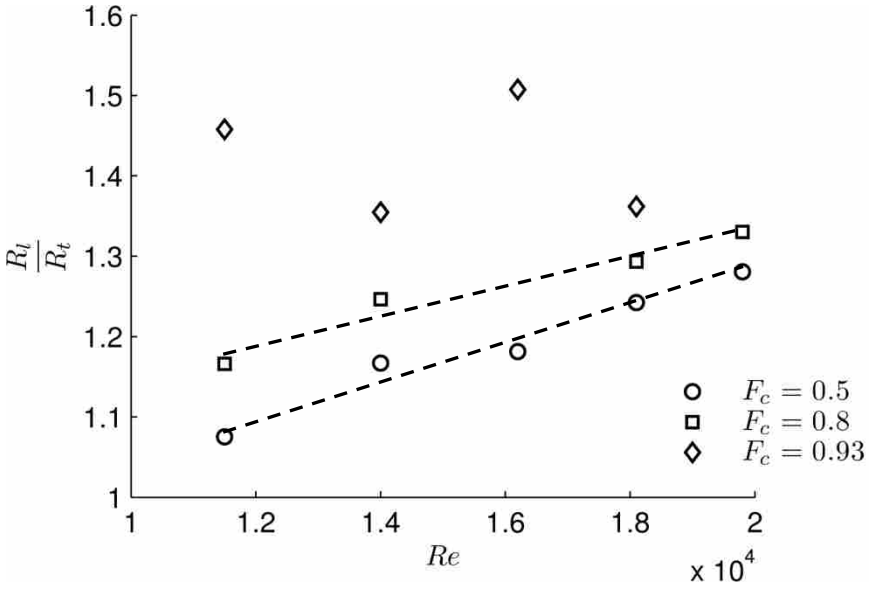

Figure 5-14. R_l/R_t as a function of *Re* for coated surfaces at each F_c and $\hat{H} = 9$

5.4.4 Comparison to Analytical Model

In order to validate the assumption that these trends occur as a result of slip in the longitudinal and transverse directions, a comparison was made to an analytical model, which has been has expanded the analysis of Bush and Aristoff [20] to account for slip [26]. The slip lengths used in this model were based on Stokes flow, and were dependent on direction with respect to the ribs. Figure 5-15 shows $\hat{R}_l$ (left) and $\hat{R}_t$ (right) vs $\hat{H}$, comparing experimental results to the analytical model for an $F_c = 0.8$ surface at varying *Re*. The resulting plot indicates that for *Re* = 11500, the prediction for jump location is accurate, but for all higher *Re,* the model predicts that the jump will occur at a larger radius. The experiments also manifest a larger decrease in radius with increasing $\hat{H}$, indicating a greater sensitivity to hydrostatic force.

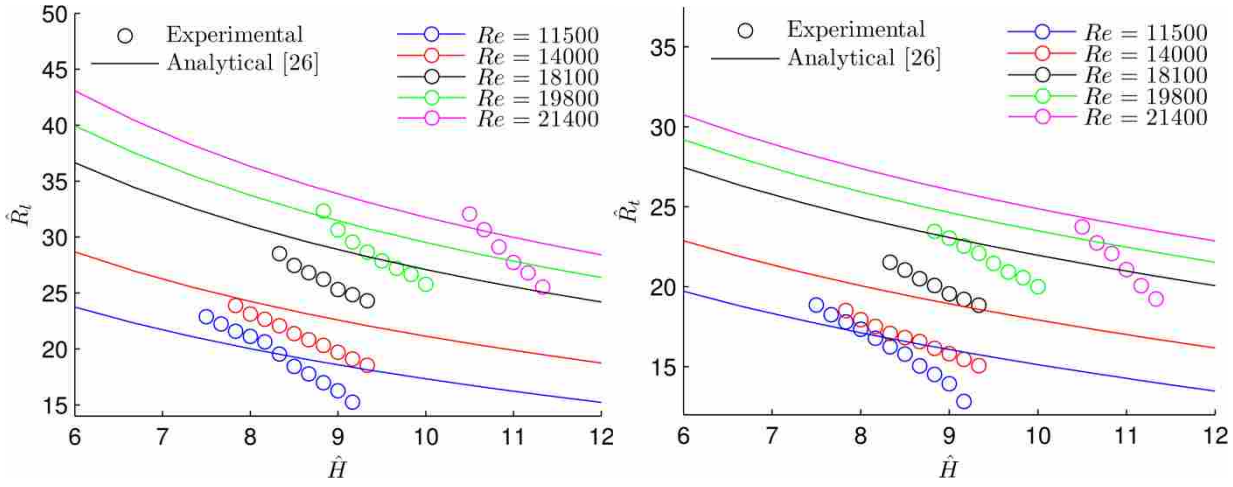

Figure 5-15. A comparison of analytical and experimental results of $\hat{R}_l$ (left) and $\hat{R}_t$ (right) as a function of $\hat{H}$ for F_c = 0.8 surfaces at multiple *Re*.

Figure 5-16 also compares the experimental results to the analytical model, focusing on R_l/R_t vs $\hat{H}$ at for an F_c = 0.8 surface at various *Re*. The analytical model under-predicted R_l/R_t by approximately 5%, when compared to the experimental results. The change in R_l/R_t as $\hat{H}$ and *Re* increased was also consistent between the model and the experimental results. This indicates that the direction-dependent slip interactions found in this analytical model are consistent with the experimental results.

5.4.5 Total Thin-Film Area

We now consider the difference in the total area encompassed by the thin film region prior to the hydraulic jump, specifically with regards to how this area varies with $\hat{H}$, *Re*, and F_c. For the F_c = 0.5 and 0.8 surfaces, this area was defined by assuming an elliptical shape with the major and minor axes aligned in the longitudinal and transverse directions, respectively. This assumption yielding the ratio of the film region, A, to the area of the incoming jet, A_j, to be $\hat{A} = R_l R_t/a^2$. The area of the film region for F_c = 0.93 was determined differently due to the

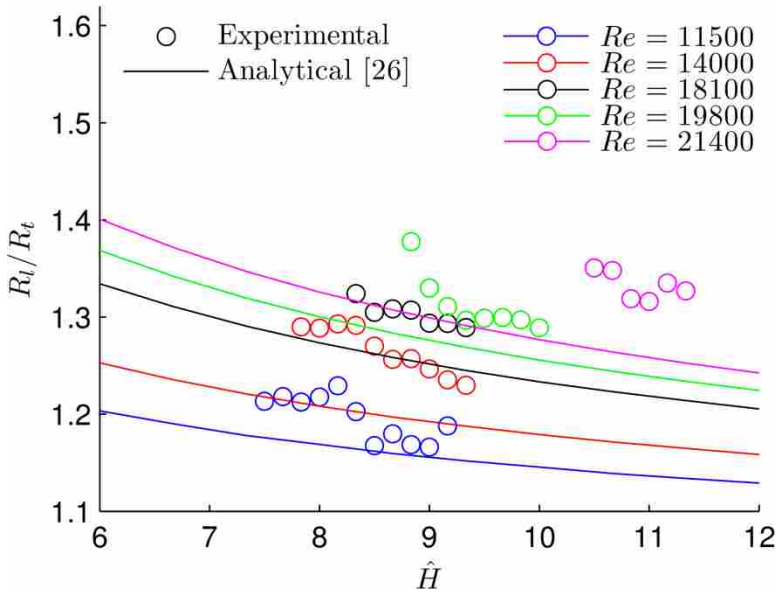

Figure 5-16. A comparison of analytical and experimental results of R_l/R_t (right) as a function of $\hat{H}$ for F_c = 0.8 surfaces at multiple *Re*.

deviation from elliptical behavior in these cases, which can be seen in the right panel of Figure 5-7. The distance in the transverse direction between the jet and the corner where the ellipse is truncated was measured for each frame. This distance along with the measured hydraulic jump location in the longitudinal and transverse directions was sufficient to calculate the area if the truncation in the longitudinal direction was assumed to be linear.

Shown in Figure 5-17 is $\hat{A}$ vs $\hat{H}$ for the F_c = 0.5 surface and for all *Re*. As expected, $\hat{A}$ increases with increasing *Re.* As the momentum of the jet increases, more area will be required to dissipate that momentum, to reach a balance with the hydrostatic force downstream of the hydraulic jump. Similarly, $\hat{A}$ decreases with increasing $\hat{H}$ due to the increased hydrostatic force. This behavior is consistent for each F_c, as can be seen in Figure 5-18 which plots $\hat{A}$ as a function of $\hat{H}$ for all F_c for *Re* = 14000 in the left panel and *Re* = 19800 on the right. This figure also demonstrates that while some variation exists, a general increase in F_c results in a decrease in $\hat{A}$.

This decrease occurs as a result of a decrease in $\hat{R}_t$ and no significant change in $\hat{R}_l$ as F_c increases.

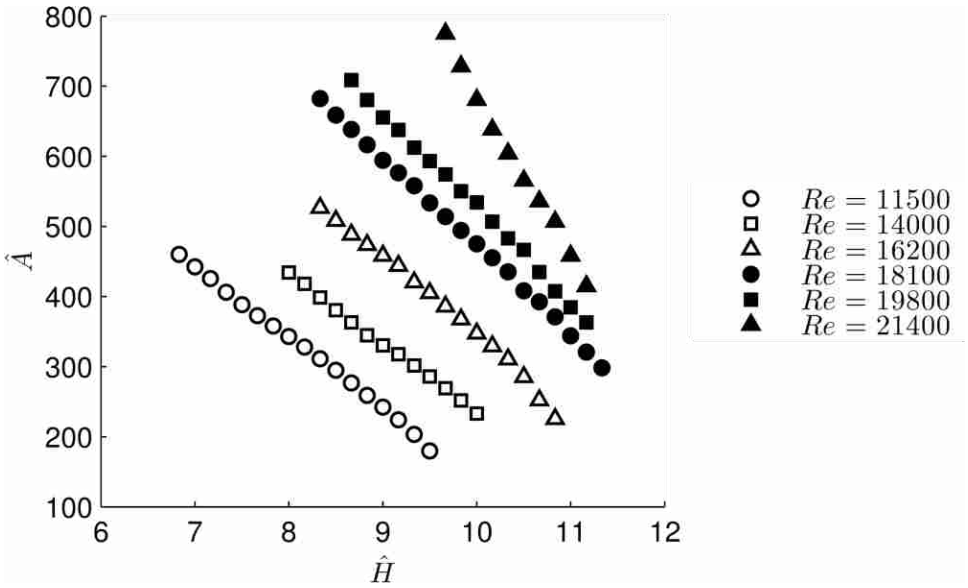

Figure 5-17. $\hat{A}$ vs $\hat{H}$ for coated surfaces where F_c = 0.5

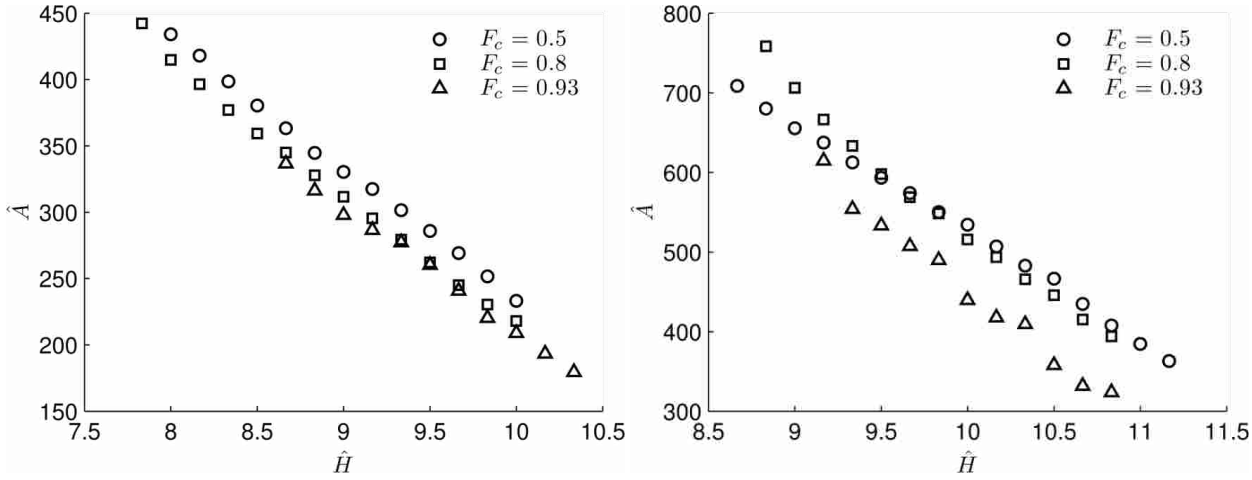

Figure 5-18. $\hat{A}$ vs $\hat{H}$ for all F_c, at *Re* = 14000 (left) and *Re* = 19800 (right)

A general trend is found when comparing the thin-film area of coated surfaces (A_c) and uncoated surfaces (A_c), which can be seen in Figure 5-19. As *Re* increases, A_c/A_u decreases and approaches unity. One large factor in this behavior may be the transition to turbulence discussed

in conjunction with Figure 5-12. Another probable cause for this behavior may be that at large *Re*, the flow is operating more in the Wenzel state. For small *Re*, there is some drag reduction on coated surfaces, most likely associated with the flow achieving Cassie state. However, as *Re* increases, the cavities likely begin to flood over larger portions of the surface (Wenzel state), and the coated surfaces begin to behave increasingly like the uncoated surfaces. This may be in part due to the fact that coated surfaces wet in the vicinity of the impingement point due to the stagnation pressure of the jet. At low *Re* the water is likely able to escape from the cavities and restore the Cassie state. However, as the momentum increases, the radius at which the fluid can escape from the cavities increases.

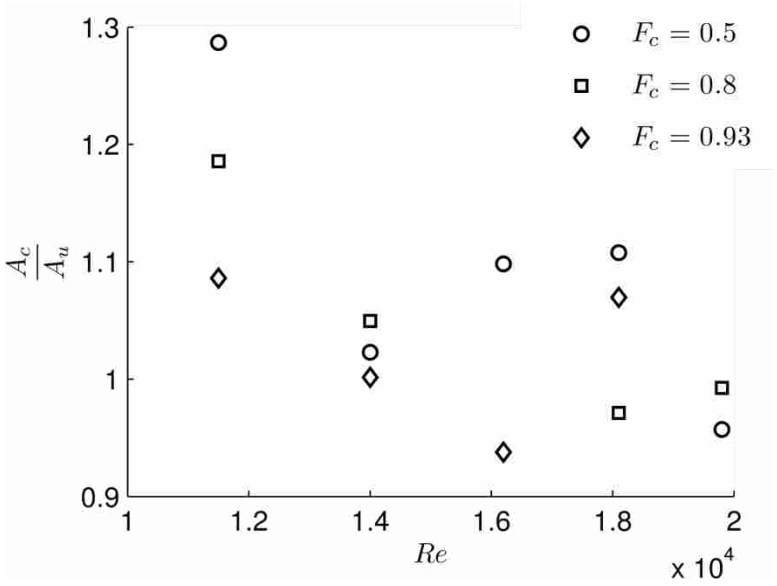

Figure 5-19. A_c/A_u as a function of *Re* at $\hat{H}$ = 9 for all F_c

5.5 Conclusion

When a jet of water impinges normally on an anisotropically patterned surface, a complex flow will occur based on the disparity in frictional resistance between the directions of

the flow. In the case of ribs and cavities, this generally results in an elliptical transition. For patterned surfaces where water is allowed to fill the cavities of the pattern (Wenzel state), a hydraulic jump occurs. When the surface is superhydrophobic (Cassie state), the type of transition is heavily dependent on the downstream fluid depth. For small downstream depths, a surface tension based transition occurs, where the flow breaks up into filaments or droplets, and moves off of the surface preferentially in the direction parallel to the ribs. When the downstream depth is increased a hydraulic jump occurs, the radial location of which is dependent on Reynolds number, downstream fluid depth and cavity fraction. When comparing hydraulic jumps in Cassie state flow with Wenzel state flow at the same conditions, a consistent increase in longitudinal jump radius is seen, while the increase in the transverse jump radius is dependent on Reynolds number and cavity fraction. As the Reynolds number and cavity fraction increase, the increase in jump radius is reduced and eventually disappears. The most likely explanation for this is that a transition to turbulence is increasing the frictional resistance in the transverse direction. The area of the thin film is greater for coated surfaces than for uncoated, but this increase loses effect as the Reynolds number increases. This is likely due to a combination of transition to turbulence and an increasing fraction of the flow in the Wenzel state.

6 CONCLUSION

Perpendicular jet impingement can be very useful in characterizing flow over superhydrophobic surfaces due to the thin film and multidirectional nature of the flow, particularly when using surfaces with high anisotropy. Impingement on rib and cavity patterned surfaces results in elliptical transitions. When water over the surface is in the Wenzel state as described in Chapter 4, the location of the hydraulic jump in the longitudinal direction increases slightly compared to the circular hydraulic jump on smooth surfaces. In the transverse direction, the hydraulic jump radius decreases, due to the obstruction of the flow provided by the ribs. As the cavity fraction increases, a minor increase is observed in the longitudinal jump radius, and a modest decrease is seen in the transverse radius. Also, the eccentricity of the elliptical hydraulic jump increases with increasing Reynolds number, surface cavity fraction, and decreasing imposed downstream water depth. Further, the total area of the supercritical thin-film region internal to the hydraulic jump is smaller for patterned surfaces as compared to smooth surfaces at similar conditions. This is due to the increased friction in the perpendicular rib-cavity direction. As the area of the thin-film region increases due to increasing Re or decreasing H, the eccentricity of the ellipse increases because the disparity in friction in the two primary spreading directions increases and exerts greater influence.

When the fluid over the surfaces is in the Cassie state, which was discussed in Chapter 5, three regimes are observed. In the first regime, which occurs when the downstream depth is small, the momentum of the initial jet impingement combined with the surface tension interaction forces the water off of the surface, and the thin film on the surface breaks up into droplets. The regime that results from large downstream depths exhibits a pulsatile behavior where a hydraulic jump repeatedly forms and collapses. The regime which occurs at intermediate downstream depths results in a stable thin film and hydraulic jump comparable to flows in the Wenzel state. The longitudinal jump radius for coated surfaces is larger than for flow over uncoated surfaces at similar flow conditions due to an increase in slip in that direction. The change in transverse jump radius is dependent on Reynolds number, where the hydraulic jump occurs at a larger radius for coated surfaces than for uncoated, but as Reynolds number increases, this improvement diminishes. This is most likely because the flow begins to transition to turbulence and the Cassie state begins to break down at higher Weber numbers.

6.1 Future Work

The scope of this thesis is subject to some limitations and weaknesses which future work can address to further illuminate the physics of jet impingement on superhydrophobic surfaces. One such limitation is that the present research focuses exclusively on highly anisotropic surface patterning, and isotropic patterning would provide valuable information about the friction reducing properties of superhydrophobic surfaces. A valuable next step will be to manufacture and study jet impingement over a post-patterned surface, which results in a pattern that is much more isotropic. Also, the Reynolds number range used is relatively high and results in a transition to turbulence which adds an undesirable degree of uncertainty. Since the majority of

experimental studies have focused on laminar flow, it would be beneficial to focus on lower Reynolds numbers in the future. Similarly, the current experimental configuration often causes recirculation eddies downstream of the hydraulic jump, which nearly all of the experimental research performed has avoided. This could be avoided by using a larger nozzle which would increase the thickness of the film and decrease the velocity of the flow. This may be problematic because this would cause the location of the jump to increase, and there are limitations to the size of the surfaces that can be created. However, if the Reynolds number is decreased, a larger nozzle may be feasible. The final limitation to this research has been that the stagnation pressure at the impingement point is large enough that the water floods the cavities and must be expelled from them before the effects of the Cassie state can be observed. This limitation can be compensated for by creating a target on the surface to prevent the water from flooding cavities. This should increase the area over which Cassie state flow exists appreciably.

REFERENCES

[1] Lafuma, A., and Quere, D., 2003, "Superhydrophobic States", Nature Mater, **2**, pp. 457-460.

[2] Lauga, E., and Stone, H., 2003, "Effective Slip in Pressure-Driven Stokes Flow", J. Fluid Mech., **489**, pp. 55-77.

[3] Davies, J., Maynes, D., Webb, B.W., and Woolford, B., "Laminar Flow in a Microchannel With Super-Hydrophobic Walls Exhibiting Transverse Ribs", Phys. Fluids, **18**, 087110.

[4] Woolford, B., Maynes,D., and Webb, B.W., 2009, "Liquid Flow through microchannels with grooved walls under wetting and superhydrophobic conditions", Microfluid. Nanofluid., **7**, pp. 121-135.

[5] Ou, J., and Rothstein, J.P., 2005, "Direct Velocity Measurements of the Flow Past Drag-Reducing Ultrahydrophobic Surfaces", Phys. Fluids, **17**, pp.103606.

[6] Daniello, R., Waterhouse, N.E., and Rothstein, J.P., 2009, "Turbulent Drag Reduction Using Superhydrophobic Surfaces", Phys. Fluids, **21**, 085103.

[7] Ybert, C., Barentin, C., Cottin-Bizonne, C., Joseph, P., and Bocquet, L., 2007, "Achieving Large Slip with Superhydrophobic Surfaces: Scaling Laws for Generic Geometries", Phys. Fluids, **19**, 123601.

[8] Jeffs, K., Maynes, D., Webb, B.W., 2010, "Prediction of Turbulent Channel Flow with Superhydrophobic Walls Consisting of Micro-Ribs and Cavities Oriented Parallel to the Flow Direction", Int. J. Heat Mass Transfer, **53**, 786.

[9] Maynes, D., Johnson, M., and Webb, B.W., 2011, "Free-Surface Liquid Jet Impingement on Rib Patterned Superhydrophobic Surfaces," Phys. Fluids, **23**, 052104.

[10] Kibar, A., Karabay, H., Yigit, K.S., Ucar, O.U., and Erbil, H.Y., 2010, "Experimental Investigation of Inclined Liquid Water Jet Flow onto Vertically Located Superhydrophobic Surfaces", Exp. Fluids, **49**(5), pp. 1135-1145.

[11] Dressaire, E., Courbin, L., Crest, J., and Stone, H., 2009, "Thin-Film Fluid Flows Over Microdecorated Surfaces: Observation of Polygonal Hydraulic Jumps," Phys. Rev. Lett., **102**, 194503.

[12] Dressaire, E., Courbin, L., Crest, J., and Stone, H., 2010, "Inertia Dominated Thin-Film Flows Over Microdecorated Surfaces," Phys. Fluids, **22**, 073602.

[13] Lin, S.P., and Jiang, W.Y., 2003, "Absolute and Convective Instability of a Radially Expanding Liquid Sheet", Phys. Fluids, **15**, pp. 1745.

[14] Watson, E.J., 1964, "The Radial Spread of a Liquid Jet Over a Horizontal Plane," J. Fluid Mech., **20**, pp. 481-499.

[15] S. Ishigai., Nakanishi, S., Mizuno, M., and Imamura, T., 1977, "Heat Transfer of the Impinging Round Water Jet in the Interference Zone of Film Flow along the Wall," Bull. JSME, **20** (139), pp. 85-92.

[16] Nakoryakov, V.E., Pokusaev, B.G., and Troyan, E.N., 1978, "Impingement of an Axisymmetric Liquid Jet on a Barrier," Int. J. Heat Mass Transfer, **21**, pp. 1175-1184.

[17] Craik, A.D.D., Latham, R.C, Fawkes, M.J., and Gribbon, P.W.F., 1981, "The Circular Hydraulic Jump," J. Fluid Mech., **112**, pp. 347-362.

[18] Ellegaard, C., Hansen, A.E., Haaning, A., and Bohr, T., 1996, "Experimental Results on Flow Separation and Transitions in the Circular Hydraulic Jump," Phys. Scr., **T67**, pp. 105-110.

[19] Liu, X., and Leinhard V, J.H., 1993, "The Hydraulic Jump in Circular Jet Impingement and in Other Thin Liquid Films," Exp. Fluids, **15**, pp. 108-116.

[20] Bush, J.W.M., and Aristoff, J.M., 2003, "The Influence of Surface Tension on the Circular Hydraulic Jump," J Fluid Mech., **489**, pp. 229-238.

[21] Bush, J.W.M., Aristoff, J.M., and Hosof, A.E., 2006, "An Experimental Investigation of the Stability of the Circular Hydraulic Jump", J. Fluid Mech., **558**, pp. 33-52.

[22] Bohr, T., Dimon, P., and Putkaradze, V., 1993, "Shallow-water approach to the circular hydraulic jump", J. Fluid Mech., **254**, pp. 635-648.

[23] Johnson, M., Maynes, D., Vanderhoff, J.C., 2012, "Hydraulic Jump Due to Jet Impingement on Micro-Patterned Surfaces Exhibiting Ribs and Cavities", International Mechanical Engineering Congress and Exposition, American Society of Mechanical Engineers, Houston

[24] Wolf, D.H., Viskanta, R., and Incropera, F.P., 1995, "Turbulence Dissipation in a Free-Surface Jet of Water and Its Effect on Local Impingement Heat Transfer From a Heated Surface: Part 1—Flow Structure", J. Heat Transfer, **86**, pp. 85-94

[25] Brechet, Y., and Neda, Z., 1998, “On the Circular Jump”, Am. J. Phys., **67**, pp. 723-731

[26] Prince, J., Private Correspondence, Sept 17th, 2012

APPENDIX A. TABULATED RESULTS

Table A-1. Experimental results for hydraulic jumps on a smooth, uncoated surface ($F_c = 0$)

Re = 11500		*Re* = 14000		*Re* = 16200		*Re* = 18100		*Re* = 19800		*Re* = 21400	
H/a	*R/a*	*H/a*	*R/a*	*H/a*	*R/a*	*H/a*	*R/a*	*H/a*	*R/a*	*H/a*	*R/a*
5.00	24.09	5.00	29.13	5.00	32.91	6.67	32.52	5.00	39.87	6.17	38.14
5.17	23.77	5.17	28.50	5.17	32.62	6.83	32.10	5.17	39.26	6.33	37.68
5.33	23.44	5.33	27.98	5.33	32.07	7.00	31.63	5.33	38.62	6.50	37.15
5.50	23.05	5.50	27.39	5.50	31.74	7.17	31.20	5.50	38.06	6.67	36.69
5.67	22.61	5.67	26.97	5.67	31.20	7.33	30.88	5.67	37.49	6.83	36.30
5.83	22.22	5.83	26.63	5.83	30.74	7.50	30.46	5.83	36.92	7.00	35.80
6.00	21.89	6.00	26.14	6.00	30.31	7.67	30.02	6.00	36.43	7.17	35.48
6.17	21.58	6.17	25.77	6.17	29.90	7.83	29.57	6.17	35.96	7.33	34.85
6.33	21.30	6.33	25.38	6.33	29.48	8.00	29.20	6.33	35.47	7.50	34.58
6.50	21.01	6.50	25.06	6.50	29.10	8.17	28.83	6.50	35.06	7.67	34.13
6.67	20.80	6.67	24.82	6.67	28.71	8.33	28.51	6.67	34.65	7.83	33.75
6.83	20.59	6.83	24.51	6.83	28.39	8.50	28.12	6.83	34.27	8.00	33.36
7.00	20.41	7.00	24.17	7.00	27.99	8.67	27.52	7.00	33.91	8.17	32.98
7.17	20.14	7.17	23.85	7.17	27.58	8.83	27.14	7.17	33.53	8.33	32.55
7.33	19.86	7.33	23.48	7.33	27.25	9.00	26.64	7.33	33.21	8.50	32.18
7.50	19.60	7.50	23.17	7.50	26.91	9.17	26.15	7.50	32.89	8.67	31.79
7.67	19.34	7.67	22.85	7.67	26.54	9.33	25.83	7.67	32.52	8.83	31.43
7.83	19.02	7.83	22.47	7.83	26.18	9.50	25.45	7.83	32.21	9.00	30.94
8.00	18.64	8.00	22.03	8.00	25.71	9.67	24.89	8.00	31.85	9.17	30.58
8.17	18.26	8.17	21.66	8.17	25.28	9.83	24.43	8.17	31.46	9.33	30.02
8.33	17.77	8.33	21.19	8.33	24.90	10.00	24.01	8.33	31.07	9.50	29.66
8.50	17.38	8.50	20.79	8.50	24.41	10.17	23.65	8.50	30.66	9.67	29.25
8.67	16.91	8.67	20.34	8.67	24.02	10.33	23.33	8.67	30.17	9.83	28.73
8.83	16.34	8.83	19.99	8.83	23.64	10.50	22.74	8.83	29.69	10.00	28.28
9.00	15.98	9.00	19.52	9.00	23.22	10.67	22.15	9.00	29.29	10.17	27.72
9.17	15.39	9.17	19.10	9.17	22.81	10.83	21.76	9.17	28.76	10.33	27.21
9.33	14.72	9.33	18.57	9.33	22.30	11.00	21.21	9.33	28.29	10.50	26.73
9.50	14.12	9.50	18.13	9.50	21.91	11.17	20.74	9.50	27.80	10.67	26.24
		9.67	17.60	9.67	21.43	11.33	20.06	9.67	27.32	10.83	25.69
		9.83	17.06	9.83	20.80	11.50	19.53	9.83	26.85	11.00	25.19
		10.00	16.61	10.00	20.43	11.67	18.81	10.00	26.34	11.17	24.54
				10.17	19.84			10.17	25.84	11.33	24.12
				10.33	19.19			10.33	25.30	11.50	23.54
				10.50	18.57			10.50	24.78	11.67	22.71
				10.67	17.93			10.67	24.19	11.83	22.14
				10.83	17.17			10.83	23.55	12.00	21.38
								11.00	23.03	12.17	20.82
								11.17	22.45		
								11.33	21.85		
								11.50	21.09		
								11.67	20.66		

Table A-2. Experimental results for hydraulic jumps on an uncoated $F_c = 0.5$ surface

Re = 11500			Re = 14000			Re = 16200			Re = 18100			Re = 19800			Re = 21400		
H/a	R_l/a	R_t/a	H/a	R_l/a	R_t/a	H/a	R_l/a	R_t/a	H/a	R_l/a	R_t/a	H/a	R_l/a	R_t/a	H/a	R_l/a	R_t/a
5.00	23.89	20.30	5.00	29.39	23.54	5.00	33.24	26.85	5.00	35.96	29.41	5.50	38.24	32.17	6.67	39.75	31.91
5.17	23.37	19.96	5.17	29.02	23.29	5.17	32.62	26.46	5.17	35.41	28.99	5.67	37.71	31.63	6.83	39.31	31.62
5.33	22.99	19.62	5.33	28.37	22.99	5.33	32.29	26.15	5.33	34.97	28.58	5.83	37.13	31.20	7.00	38.83	31.14
5.50	22.66	19.32	5.50	27.94	22.69	5.50	32.01	25.83	5.50	34.60	28.29	6.00	36.59	30.73	7.17	38.35	30.85
5.67	22.31	19.01	5.67	27.52	22.38	5.67	31.31	25.52	5.67	34.35	27.89	6.17	36.07	30.38	7.33	37.86	30.89
5.83	22.02	18.74	5.83	27.05	22.03	5.83	30.82	25.17	5.83	33.75	27.63	6.33	35.63	29.94	7.50	37.20	30.46
6.00	21.77	18.48	6.00	26.69	21.71	6.00	30.37	24.85	6.00	33.61	27.29	6.50	35.20	29.67	7.67	36.75	30.07
6.17	21.56	18.25	6.17	26.33	21.45	6.17	29.91	24.54	6.17	33.27	27.00	6.67	34.75	29.27	7.83	36.19	29.71
6.33	21.37	18.04	6.33	26.03	21.14	6.33	29.61	24.22	6.33	32.97	26.72	6.83	34.29	28.88	8.00	35.69	29.33
6.50	21.20	17.84	6.50	25.79	20.81	6.50	29.16	23.97	6.50	32.46	26.43	7.00	33.91	28.52	8.17	35.31	28.97
6.67	21.01	17.65	6.67	25.56	20.54	6.67	28.46	23.70	6.67	32.28	26.12	7.17	33.36	28.20	8.33	34.86	28.67
6.83	20.87	17.54	6.83	25.18	20.31	6.83	27.92	23.42	6.83	31.71	25.90	7.33	32.99	27.90	8.50	34.34	28.23
7.00	20.51	17.43	7.00	24.73	20.04	7.00	27.46	23.09	7.00	31.50	25.54	7.50	32.45	27.62	8.67	33.69	27.87
7.17	20.17	17.23	7.17	24.45	19.77	7.17	27.04	22.62	7.17	31.06	25.30	7.67	32.00	27.32	8.83	33.07	27.56
7.33	19.73	16.95	7.33	24.11	19.52	7.33	26.75	22.32	7.33	30.29	25.05	7.83	31.51	27.01	9.00	32.29	27.11
7.50	19.34	16.64	7.50	23.80	19.25	7.50	26.32	21.98	7.50	29.73	24.84	8.00	31.08	26.65	9.17	31.85	26.71
7.67	18.96	16.32	7.67	23.39	19.03	7.67	25.90	21.77	7.67	28.81	24.53	8.17	30.59	26.31	9.33	31.43	26.21
7.83	18.46	15.94	7.83	22.94	18.82	7.83	25.57	21.50	7.83	28.10	24.08	8.33	30.13	25.89	9.50	30.81	25.77
8.00	17.97	15.55	8.00	22.56	18.56	8.00	25.08	21.21	8.00	27.74	23.64	8.50	29.64	25.45	9.67	30.42	25.45
8.17	17.47	15.12	8.17	22.14	18.21	8.17	24.62	20.92	8.17	27.31	23.25	8.67	29.13	25.05	9.83	29.78	24.97
8.33	16.97	14.75	8.33	21.71	17.85	8.33	24.26	20.50	8.33	27.03	22.87	8.83	28.72	24.63	10.00	29.20	24.57
8.50	16.47	14.35	8.50	21.19	17.51	8.50	23.65	20.23	8.50	26.42	22.51	9.00	28.25	24.24	10.17	28.74	24.08
8.67	15.94	13.85	8.67	20.81	17.06	8.67	23.08	19.91	8.67	26.15	22.19	9.17	27.88	23.69	10.33	28.10	23.40
8.83	15.34	13.38	8.83	20.34	16.72	8.83	22.54	19.54	8.83	25.55	21.78	9.33	27.45	23.47	10.50	27.34	22.87
9.00	14.81	12.70	9.00	19.77	16.33	9.00	21.83	19.13	9.00	25.13	21.35	9.50	26.86	22.90	10.67	26.61	22.36
9.17	14.57	12.26	9.17	19.23	15.96	9.17	21.22	18.75	9.17	24.66	21.08	9.67	26.45	22.50	10.83	26.16	21.66
			9.33	18.80	15.58	9.33	20.68	18.31	9.33	24.06	20.60	9.83	25.89	21.89			
			9.50	18.40	15.15	9.50	20.21	17.81	9.50	23.50	20.28	10.00	25.31	21.25			
			9.67	17.80	14.74	9.67	19.61	17.45	9.67	23.36	19.77	10.17	24.75	20.69			
			9.83	17.42	14.21	9.83	18.92	17.01	9.83	22.75	19.31	10.33	24.12	20.43			
			10.00	16.64	13.65	10.00	18.27	16.58	10.00	22.02	18.97	10.50	23.33	20.18			
									10.17	21.36	18.29	10.67	23.04	19.48			
									10.33	20.77	17.52	10.83	21.97	18.96			
									10.50	19.93	17.25	11.00	21.36	18.55			
									10.67	19.10	16.52	11.17	20.95	17.79			
									10.83	18.59	15.90	11.33	19.68	17.13			
												11.50	18.74	16.30			

Table A-3. Experimental results for hydraulic jumps on an uncoated $F_c = 0.8$ surface

Re = 11500			Re = 14000			Re = 16200			Re = 18100			Re = 19800			Re = 21400		
H/a	R_l/a	R_t/a	H/a	R_l/a	R_t/a	H/a	R_l/a	R_t/a	H/a	R_l/a	R_t/a	H/a	R_l/a	R_t/a	H/a	R_l/a	R_t/a
5.00	23.75	20.31	5.00	29.02	22.57	5.00	33.01	25.90	5.00	36.84	28.68	5.00	41.06	34.28	5.83	43.43	34.24
5.17	23.30	19.96	5.17	28.33	22.29	5.17	32.63	25.61	5.17	36.18	28.30	5.17	40.44	33.79	6.00	42.75	33.73
5.33	22.88	19.65	5.33	28.02	22.04	5.33	32.21	25.39	5.33	35.62	27.89	5.33	39.76	33.30	6.17	42.16	33.22
5.50	22.62	19.37	5.50	27.45	21.60	5.50	31.89	25.07	5.50	35.31	27.54	5.50	39.40	32.72	6.33	41.58	32.77
5.67	22.27	19.09	5.67	27.51	21.55	5.67	31.51	24.78	5.67	34.84	27.09	5.67	38.95	32.49	6.50	41.04	32.31
5.83	21.99	18.84	5.83	26.96	21.22	5.83	31.20	24.50	5.83	34.51	26.80	5.83	38.66	32.10	6.67	40.55	31.94
6.00	21.67	18.62	6.00	26.64	20.93	6.00	30.90	24.25	6.00	34.07	26.49	6.00	38.33	31.65	6.83	40.08	31.47
6.17	21.51	18.41	6.17	26.40	20.65	6.17	30.56	23.96	6.17	33.83	26.24	6.17	37.73	31.19	7.00	39.72	31.04
6.33	21.34	18.21	6.33	26.16	20.37	6.33	30.25	23.71	6.33	33.47	25.85	6.33	37.42	30.91	7.17	39.22	30.63
6.50	21.11	18.02	6.50	25.80	20.18	6.50	29.93	23.42	6.50	33.05	25.59	6.50	36.97	30.55	7.33	38.60	30.32
6.67	20.89	17.78	6.67	25.19	19.97	6.67	29.70	23.20	6.67	32.62	25.34	6.67	36.66	30.22	7.50	38.14	29.84
6.83	20.70	17.63	6.83	24.60	19.76	6.83	29.30	22.89	6.83	32.36	25.07	6.83	36.41	30.01	7.67	37.63	29.55
7.00	20.38	17.47	7.00	24.13	19.53	7.00	28.72	22.68	7.00	31.97	24.76	7.00	35.80	29.71	7.83	37.12	29.16
7.17	20.06	17.31	7.17	23.73	19.25	7.17	27.93	22.45	7.17	31.46	24.55	7.17	35.51	29.25	8.00	36.50	28.73
7.33	19.85	17.07	7.33	23.38	18.92	7.33	27.37	22.05	7.33	30.73	24.25	7.33	34.81	28.77	8.17	36.12	28.48
7.50	19.55	16.84	7.50	22.96	18.64	7.50	26.84	21.69	7.50	30.16	24.00	7.50	34.22	28.50	8.33	35.55	28.05
7.67	19.11	16.57	7.67	22.61	18.36	7.67	26.36	21.37	7.67	29.39	23.68	7.67	33.59	28.21	8.50	34.95	27.59
7.83	18.62	16.24	7.83	22.25	18.04	7.83	26.04	21.07	7.83	28.62	23.29	7.83	32.98	27.91	8.67	34.35	27.20
8.00	18.14	15.87	8.00	21.74	17.70	8.00	25.73	20.76	8.00	28.07	22.94	8.00	32.29	27.49	8.83	33.72	26.69
8.17	17.71	15.31	8.17	21.37	17.39	8.17	25.34	20.47	8.17	27.37	22.59	8.17	31.58	27.32	9.00	32.83	26.40
8.33	17.24	14.92	8.33	20.91	17.07	8.33	24.63	20.16	8.33	26.88	22.21	8.33	31.00	26.81	9.17	32.09	26.08
8.50	16.75	14.47	8.50	20.45	16.69	8.50	24.36	19.81	8.50	26.46	21.80	8.50	30.44	26.57	9.33	31.42	25.54
8.67	16.16	13.99	8.67	20.04	16.36	8.67	23.95	19.48	8.67	25.87	21.47	8.67	29.51	25.92	9.50	30.68	24.71
8.83	15.55	13.41	8.83	19.54	15.94	8.83	23.39	19.15	8.83	25.44	21.03	8.83	29.04	25.52	9.67	29.99	24.33
9.00	14.91	12.81	9.00	19.03	15.60	9.00	23.11	18.77	9.00	24.79	20.57	9.00	28.53	24.94	9.83	29.24	23.81
9.17	14.49	12.28	9.17	18.58	15.15	9.17	22.54	18.43	9.17	24.27	20.24	9.17	28.11	24.49	10.00	28.70	23.38
			9.33	18.09	14.76	9.33	22.36	18.01	9.33	23.86	19.79	9.33	27.20	24.14			
			9.50	17.60	14.28	9.50	21.78	17.65	9.50	23.29	19.27	9.50	26.97	23.41			
			9.67	17.06	13.72	9.67	21.23	17.25	9.67	22.68	18.86	9.67	26.35	23.15			
			9.83	16.46	13.40	9.83	20.67	16.80	9.83	22.21	18.45	9.83	25.84	22.58			
			10.00	15.57	12.91	10.00	20.19	16.30	10.00	21.80	17.98	10.00	24.94	21.85			
						10.17	19.13	15.98				10.17	24.47	21.34			
						10.33	18.40	15.45				10.33	24.05	20.62			
						10.50	17.74	14.83				10.50	23.55	19.65			
												10.67	22.44	19.47			
												10.83	21.73	18.48			

Table A-4. Experimental results for hydraulic jumps on an uncoated F_c = 0.93 surface

Re = 11500			*Re* = 14000			*Re* = 16200			*Re* = 18100			*Re* = 19800			*Re* = 21400		
H/a	R_l/a	R_t/a	*H/a*	R_l/a	R_t/a	*H/a*	R_l/a	R_t/a	*H/a*	R_l/a	R_t/a	*H/a*	R_l/a	R_t/a	*H/a*	R_l/a	R_t/a
5.00	24.23	19.51	5.00	29.43	22.65	5.00	33.44	25.05	5.00	36.73	26.24	5.00	41.69	31.98	6.00	43.57	32.87
5.17	23.88	19.29	5.17	28.96	22.35	5.17	32.86	24.68	5.17	36.35	25.88	5.17	41.22	31.60	6.17	42.82	32.31
5.33	23.52	18.91	5.33	28.56	22.19	5.33	32.32	24.37	5.33	35.88	25.61	5.33	40.55	31.12	6.33	42.11	31.80
5.50	23.22	18.68	5.50	28.19	21.94	5.50	31.93	24.07	5.50	35.45	25.24	5.50	40.21	30.60	6.50	41.41	31.20
5.67	22.90	18.49	5.67	27.54	21.73	5.67	31.50	23.77	5.67	35.12	24.96	5.67	39.44	30.40	6.67	40.85	30.75
5.83	22.57	18.21	5.83	27.16	21.49	5.83	31.15	23.46	5.83	34.66	24.65	5.83	39.27	29.87	6.83	40.29	30.23
6.00	22.30	18.09	6.00	26.84	21.12	6.00	30.77	23.20	6.00	34.33	24.42	6.00	38.72	29.55	7.00	39.72	29.89
6.17	22.09	17.76	6.17	26.52	20.83	6.17	30.35	22.92	6.17	34.03	24.18	6.17	38.44	29.21	7.17	39.26	29.41
6.33	21.89	17.56	6.33	26.33	20.54	6.33	29.99	22.67	6.33	33.72	23.88	6.33	38.06	28.75	7.33	38.74	29.03
6.50	21.71	17.43	6.50	25.94	20.24	6.50	29.52	22.41	6.50	33.14	23.66	6.50	37.74	28.55	7.50	38.16	28.57
6.67	21.52	17.30	6.67	25.52	20.09	6.67	29.14	22.12	6.67	32.66	23.37	6.67	37.05	28.22	7.67	37.70	28.20
6.83	21.24	17.01	6.83	25.11	19.92	6.83	28.64	21.90	6.83	32.21	23.13	6.83	36.83	27.89	7.83	37.22	27.87
7.00	20.85	16.84	7.00	24.75	19.73	7.00	28.15	21.59	7.00	31.70	22.90	7.00	36.32	27.61	8.00	36.66	27.51
7.17	20.45	16.66	7.17	24.31	19.49	7.17	27.76	21.24	7.17	31.24	22.59	7.17	35.84	27.34	8.17	36.14	27.07
7.33	20.11	16.49	7.33	23.75	19.18	7.33	27.36	20.96	7.33	30.54	22.29	7.33	35.23	27.04	8.33	35.58	26.81
7.50	19.76	16.24	7.50	23.37	18.88	7.50	26.87	20.68	7.50	29.94	21.92	7.50	34.80	26.77	8.50	35.03	26.34
7.67	19.38	15.82	7.67	22.93	18.56	7.67	26.37	20.44	7.67	29.37	21.68	7.67	34.58	26.40	8.67	34.15	25.90
7.83	18.89	15.62	7.83	22.66	18.19	7.83	25.77	20.09	7.83	28.81	21.26	7.83	33.63	26.07	8.83	33.25	25.51
8.00	18.25	15.15	8.00	22.24	17.89	8.00	25.19	19.75	8.00	28.22	20.92	8.00	33.73	25.79	9.00	32.53	25.09
8.17	17.67	14.78	8.17	21.77	17.43	8.17	24.75	19.41	8.17	27.59	20.56	8.17	32.66	25.32	9.17	31.61	24.62
8.33	17.15	14.40	8.33	21.22	17.06	8.33	24.25	19.06	8.33	26.93	20.25	8.33	31.68	24.94	9.33	30.95	24.14
8.50	16.60	13.99	8.50	20.82	16.71	8.50	23.76	18.64	8.50	26.46	19.80	8.50	30.96	24.54	9.50	30.07	23.72
8.67	16.09	13.53	8.67	20.29	16.26	8.67	23.30	18.25	8.67	25.77	19.50	8.67	29.95	24.12	9.67	29.36	23.16
8.83	15.50	13.02	8.83	19.82	15.81	8.83	22.85	17.84	8.83	25.43	19.11	8.83	29.51	23.88	9.83	28.78	22.69
9.00	15.12	12.37	9.00	19.31	15.41	9.00	22.39	17.56	9.00	24.78	18.68	9.00	28.71	23.37	10.00	28.16	22.29
9.17	14.37	11.43	9.17	18.96	14.90	9.17	21.84	17.08	9.17	24.30	18.22	9.17	28.29	22.86			
9.33	13.23	10.73	9.33	18.44	14.39	9.33	21.32	16.59	9.33	23.86	17.78	9.33	27.44	22.34			
9.50	12.07	9.94	9.50	17.91	14.00	9.50	20.75	16.10	9.50	23.14	17.34	9.50	26.92	21.98			
			9.67	17.16	13.36	9.67	20.18	15.65	9.67	22.59	16.83	9.67	26.15	21.31			
			9.83	16.07	12.72	9.83	19.71	15.21	9.83	22.17	16.34	9.83	25.56	20.76			
			10.00	14.80	12.21	10.00	19.05	14.67	10.00	21.42	15.82	10.00	25.06	20.22			
						10.17	18.55	13.99				10.17	24.25	19.32			
						10.33	17.77	13.49				10.33	23.49	18.72			
						10.50	16.91	12.87				10.50	22.56	18.03			
												10.67	21.97	17.05			
												10.83	21.93	16.60			

Table A-5 Experimental results for hydraulic jumps on a coated $F_c = 0.5$ surface

Re = 11500			Re = 14000			Re = 16200			Re = 18100			Re = 19800			Re = 21400		
H/a	R_l/a	R_t/a	H/a	R_l/a	R_t/a	H/a	R_l/a	R_t/a	H/a	R_l/a	R_t/a	H/a	R_l/a	R_t/a	H/a	R_l/a	R_t/a
6.83	22.09	20.83	8.00	22.89	18.96	8.33	24.92	21.14	8.17	0.00	23.90	8.67	30.11	23.54	9.67	31.91	24.29
7.00	21.60	20.48	8.17	22.47	18.60	8.50	24.49	20.75	8.33	29.27	23.31	8.83	29.44	23.10	9.83	31.11	23.41
7.17	21.10	20.17	8.33	21.91	18.19	8.67	24.01	20.34	8.50	28.76	22.91	9.00	28.97	22.63	10.00	29.94	22.73
7.33	20.65	19.68	8.50	21.36	17.81	8.83	23.65	20.03	8.67	28.22	22.62	9.17	28.45	22.41	10.17	29.01	22.00
7.50	20.21	19.21	8.67	20.73	17.52	9.00	23.27	19.70	8.83	27.74	22.23	9.33	27.98	21.89	10.33	28.15	21.47
7.67	19.79	18.82	8.83	20.15	17.11	9.17	23.08	19.24	9.00	27.17	21.87	9.50	27.49	21.59	10.50	27.19	20.80
7.83	19.37	18.48	9.00	19.64	16.83	9.33	22.46	18.73	9.17	26.67	21.62	9.67	27.22	21.09	10.67	26.79	20.00
8.00	18.98	18.07	9.17	19.17	16.56	9.50	22.24	18.22	9.33	26.16	21.32	9.83	26.42	20.82	10.83	25.73	19.70
8.17	18.55	17.68	9.33	18.64	16.18	9.67	21.63	17.84	9.50	25.55	20.88	10.00	26.01	20.54	11.00	24.58	18.65
8.33	18.09	17.20	9.50	18.07	15.82	9.83	20.99	17.50	9.67	25.11	20.47	10.17	25.44	19.92	11.17	23.74	17.48
8.50	17.73	16.64	9.67	17.55	15.33	10.00	20.56	16.90	9.83	24.57	20.11	10.33	24.90	19.39			
8.67	17.25	16.05	9.83	17.18	14.64	10.17	19.95	16.51	10.00	23.97	19.81	10.50	24.52	19.03			
8.83	16.65	15.54	10.00	16.59	14.05	10.33	19.34	16.05	10.17	23.51	19.36	10.67	23.58	18.44			
9.00	16.13	15.00				10.50	18.60	15.33	10.33	22.93	18.97	10.83	22.63	18.02			
9.17	15.60	14.37				10.67	17.74	14.21	10.50	22.08	18.48	11.00	22.10	17.40			
9.33	14.98	13.58				10.83	16.75	13.46	10.67	21.78	18.03	11.17	21.22	17.11			
9.50	14.07	12.77							10.83	21.27	17.45						
									11.00	20.55	16.74						
									11.17	19.69	16.29						

Table A-6. Experimental results for hydraulic jumps on a coated $F_c = 0.8$ surface

Re = 11500			Re = 14000			Re = 16200			Re = 18100			Re = 19800			Re = 21400		
H/a	R_l/a	R_t/a	H/a	R_l/a	R_t/a	H/a	R_l/a	R_t/a	H/a	R_l/a	R_t/a	H/a	R_l/a	R_t/a	H/a	R_l/a	R_t/a
7.33	23.29	0.00	7.83	23.89	18.52	8.83	27.03	18.33	8.33	28.51	21.53	8.67	0.00	24.14	10.50	32.06	23.74
7.50	22.88	18.86	8.00	23.12	17.94	9.00	26.13	18.08	8.50	27.46	21.04	8.83	32.33	23.46	10.67	30.65	22.74
7.67	22.23	18.25	8.17	22.64	17.51	9.17	25.49	17.83	8.67	26.82	20.50	9.00	30.65	23.04	10.83	29.12	22.08
7.83	21.58	17.80	8.33	22.07	17.09	9.33	24.86	17.73	8.83	26.24	20.08	9.17	29.56	22.55	11.00	27.73	21.07
8.00	21.12	17.34	8.50	21.36	16.82	9.50	24.35	17.24	9.00	25.31	19.56	9.33	28.65	22.10	11.17	26.80	20.07
8.17	20.64	16.79	8.67	20.82	16.57	9.67	23.94	16.71	9.17	24.84	19.21	9.50	27.87	21.46	11.33	25.52	19.23
8.33	19.54	16.25	8.83	20.30	16.15	9.83	23.29	16.39	9.33	24.30	18.85	9.67	27.19	20.92	11.50	25.31	18.36
8.50	18.43	15.79	9.00	19.71	15.81	10.00	22.72	16.02	9.50	24.07	18.39	9.83	26.67	20.56	11.67	24.77	17.71
8.67	17.77	15.06	9.17	19.10	15.46	10.17	22.25	15.54	9.67	23.44	17.63	10.00	25.78	20.00	11.83	25.85	16.80
8.83	16.97	14.52	9.33	18.53	15.07	10.33	21.65	15.27	9.83	22.81	17.02	10.17	24.89	19.83	12.00	23.24	16.09
9.00	16.25	13.94	9.50	17.81	14.72	10.50	20.92	15.21	10.00	22.08	16.52	10.33	24.51	19.01			
9.17	15.23	12.82	9.67	16.97	14.44	10.67	20.25	14.99	10.17	21.54	15.90	10.50	24.26	18.37			
9.33	14.76	0.00	9.83	16.06	14.35	10.83	19.58	14.58	10.33	21.04	15.11	10.67	23.39	17.76			
			10.00	15.24	14.31	11.00	18.55	13.68									
						11.17	17.63	13.24									

Table A-7. Experimental results for hydraulic jumps on a coated $F_c = 0.93$ surface

Re = 11500			Re = 14000			Re = 16200			Re = 18100			Re = 19800			Re = 21400		
H/a	R_l/a	R_t/a	H/a	R_l/a	R_t/a	H/a	R_l/a	R_t/a	H/a	R_l/a	R_t/a	H/a	R_l/a	R_t/a	H/a	R_l/a	R_t/a
8.33	19.79	12.98	8.67	21.63	15.56	8.50	25.45	16.54	8.50	28.15	19.97	9.17	30.02	20.48	10.17	30.68	22.15
8.50	19.18	12.70	8.83	20.85	15.17	8.67	25.00	16.21	8.67	27.34	19.66	9.33	27.33	20.28	10.33	28.60	21.11
8.67	18.63	12.30	9.00	20.09	14.83	8.83	24.24	15.93	8.83	26.58	19.36	9.50	27.09	19.69	10.50	26.81	20.34
8.83	17.85	12.12	9.17	19.42	14.76	9.00	23.57	15.64	9.00	25.96	19.07	9.67	26.33	19.27	10.67	26.25	18.95
9.00	17.21	11.80	9.33	19.05	14.55	9.17	23.41	15.68	9.17	25.35	18.56	9.83	26.05	18.80	10.83	25.63	17.92
9.17	16.72	11.59	9.50	18.16	14.34	9.33	22.83	15.50	9.33	24.54	18.08	10.00	24.65	17.83	11.00	24.24	17.03
9.33	15.92	11.38	9.67	17.20	14.00	9.50	22.63	15.19	9.50	23.81	17.59	10.17	24.17	17.28	11.17	22.74	15.39
9.50	14.96	11.16	9.83	16.28	13.53	9.67	22.28	14.87	9.67	23.56	17.11	10.33	23.96	17.09			
9.67	14.02	10.74	10.00	15.61	13.38	9.83	20.92	14.80	9.83	22.91	16.36	10.50	22.31	16.05			
9.83	13.14	10.40	10.17	15.14	12.78	10.00	20.66	14.43	10.00	22.40	16.07	10.67	21.62	15.35			
10.00	12.27	9.97	10.33	14.36	12.49	10.17	20.06	13.93	10.17	22.44	15.64	10.83	21.43	15.11			
						10.33	19.52	13.33	10.33	21.75	15.11						
						10.50	18.34	12.82	10.50	21.06	14.42						
						10.67	16.84	11.89	10.67	21.07	13.71						
									10.83	19.92	13.25						

APPENDIX B. MATLAB CODE

B.1 Description

These MATLAB scripts are associated with the analysis process described in Chapter 3. The script used to analyze videos and determine jump diameter will be given, followed by a script to calibrate the images and average data from multiple experimental runs.

B.2 Video Analysis Script

```
close all; clc; clear all;


% Initial Settings
nvid = 1;                   % Number of videos for this experiment (Always 1)
sk = 0;                     % Number of frames to skip (Always 0)
frmavg = 1;                 % Number of frames combined - Must be an odd number
swid = 5;                   % Number of pixels averaged in mean derivative Criterion -
Must be an odd number
bandwid = 5;                % Pixel width of search band - Must be an odd number
rngsz = .10;                % Size of the search window used to find the next jump
location.
                            % rngsz is the fraction of the radial distance from the jet to
the jump.
```

```
                                % The search window goes rngsz*JumpRadius in either
direction from the
                                % average location of the jump in the last five frames.
        ceiling = .02;          % This defines a brightness threshold, to which all
brightness values will be
                                % truncated. When the first image is analyzed, a box is
selected,
                                % in which all brightness values are averaged. The truncation
                                % value will then be 1 + ceiling*AverageBrightness.

        TW = 5;                 % The number of previous jump location values to be
averaged to
                                % determine the center of the search window

        track = 2;              % 1: Track by threshold    2: Track by mean derivative

        C = input('Which direction is being measured? (1: Smooth or Long, 2: Trans)');

        % Read in excel sheet
        xlsname = 'datacatalog.xls';
        sprintf('Select the data you want analyzed from Column F \n(starting with "Long
Video") to Column S (Weber Number)')
        [~,~,form] = xlsread(xlsname,-1);
```

```
 fnamebase = form{2*C,end-9};
curvename = form{2*C,end-7};

% Read in video data
fname = cell(nvid,1);
movinfo = cell(nvid,1);
numfr = zeros(nvid,1);
sumnumfr = zeros(nvid,1);

for i = 1:nvid;
    fname{i} = strcat(fnamebase,'.avi');
    movinfo{i} = aviinfo(fname{i});
    numfr(i) = movinfo{i}.NumFrames;
    sumnumfr(i) = sum(numfr);
end

 framerate = form{2*C,end-8};
totalt = sumnumfr(nvid)/framerate;

hi = form{end,end-4};                    % Initial Height Measurement
hf = form{end,end-1};                    % Final Height Measurement
We = form{end-1,end};                    % Weber Number Measurment
```

```
 % Prompt for needle diameter
needle = input('What color needle did you use?  ','s');
if strcmp(needle,'Blue') || strcmp(needle,'blue')
   Djet = .000414;                                  %m
elseif strcmp(needle,'Yellow') || strcmp(needle,'yellow')
   Djet = .000614;                                  %m
elseif strcmp(needle,'Pink') || strcmp(needle,'pink')
   Djet = .000838;                                  %m
elseif strcmp(needle,'Purple') || strcmp(needle,'purple')
   Djet = .00119;                                  %m
end

 % Define Analysis Statistics
Hrate = (hf-hi)/sumnumfr(nvid)                      % Rate of change in Height

skprt = 1;                                          % If skprt > 1, frames will be skipped in the
analysis

Ajet = pi*Djet^2/4;                                 % Area of the jet

sig = .0729;                                        %Surface tension (N/m)
rho = 999;                                          %Density (kg/m^3)
nu = 1.12e-6;                                       %Kinematic Viscosity (m^2/s)
```

```
if We == 0;
    Q = VQ/tQ;
    Qmet = Q/1e6;
    ujet = Qmet/Ajet;
else
    ujet = (We*sig/(rho*Djet))^.5;
    Qmet = Ajet*Ujet;
end

 We =  rho*ujet^2*Djet/sig;                          % Weber Number
Re = Qmet/(Djet/2*nu);                               % Reynolds Number

 % Load 2nd frame of video
mov1 = aviread(fname{1},2);
image(mov1(1).cdata)
axis equal
colormap(gray)

% If video was captured by CCD camera, check if the image is skewed
if form{2*C,end-10} == 2
    skstr = input('Is the image skewed?','s');
    if strcmp(skstr,'y') || strcmp(skstr,'Y') || strcmp(skstr,'Yes') || strcmp(skstr,'yes')
        sk = 1;
```

```
    else
        sk = 0;
    end
end

% If image is skewed, straighten image
if sk == 1
    mov1 = aviread(fname{1},2);
    sz = size(mov1.cdata);
    image(mov1.cdata)
    ylim([0 99])
    [x,y] = ginput(1);
    key = round(linspace(x,sz(2),sz(1)));
end

% If video was captured with High Speed camera, adjust brightness
brtscl = 1;
if form{2*C,end-10} == 1
    brtrip = 0;

    while brtrip == 0
        if sk == 0
            mov1 = aviread(fname{1},round(numfr(1))/2);
```

```
else
    mov1sk = aviread(fname{1},round(numfr(1))/2);
    structsz = max(size(mov1sk));
    sz = size(mov1sk(1).cdata);
    mov1 = struct('cdata',zeros(sz(1)-1,sz(2)-1,sz(3)));
    for skframe = 1:structsz
       for i = 1:sz(1)-1
          sz1 = size(mov1sk(skframe).cdata(i+1,key(i+1):end,:));
          sz2 = size(mov1sk(skframe).cdata(i,1:key(i)-1,:));

          ln(i) = sz1(2) + sz2(2);
          if ln(i) == sz(2)-1
             mov1(skframe).cdata(i,:,:) =
double([mov1sk(skframe).cdata(i+1,key(i+1):end,:) mov1sk(skframe).cdata(i,1:key(i)-1,:)])/255;
          else
             mov1(skframe).cdata(i,:,:) =
double([mov1sk(skframe).cdata(i+1,key(i+1)+1:end,:) mov1sk(skframe).cdata(i,1:key(i)-
1,:)])/255;
          end
       end
    end
end
```

```
        image(imlincomb(brtscl,mov1(1).cdata));
        axis equal
        colormap(gray)
        brtstr = input('Is the brightness acceptable?','s');
        if strcmp(brtstr,'y') || strcmp(brtstr,'Y') || strcmp(brtstr,'Yes') || strcmp(brtstr,'yes')
            brtrip = 1;
        else
            brtscl = input('Enter a new scaling factor: ');
        end

    end
end

% If not specified in Excel File, determine when the flow starts, and when
% to start analysis
if isnan(form{2*C+1,end-10})
    framescan1 = input('How long would you like to preview?');
    if sk == 0
        mov1 = aviread(fname{1},1:framescan1);
    else
        mov1sk = aviread(fname{1},1:framescan1);
        structsz = max(size(mov1sk));
        sz = size(mov1sk(1).cdata);
```

```
        mov1 = struct('cdata',zeros(sz(1)-1,sz(2)-1,sz(3)));
        for skframe = 1:structsz
            for i = 1:sz(1)-1
                sz1 = size(mov1sk(skframe).cdata(i+1,key(i+1):end,:));
                sz2 = size(mov1sk(skframe).cdata(i,1:key(i)-1,:));

                ln(i) = sz1(2) + sz2(2);
                if ln(i) == sz(2)-1
                    mov1(skframe).cdata(i,:,:) =
double([mov1sk(skframe).cdata(i+1,key(i+1):end,:) mov1sk(skframe).cdata(i,1:key(i)-1,:)])/255;
                else
                    mov1(skframe).cdata(i,:,:) =
double([mov1sk(skframe).cdata(i+1,key(i+1)+1:end,:) mov1sk(skframe).cdata(i,1:key(i)-
1,:)])/255;
                end
            end
        end

        figure(1)
        for fr = 1:framescan1
            image(imlincomb(brtscl,mov1(fr).cdata))
            colormap(gray)
```

```
            text(50,50,num2str(fr),'Color',[0 1 0])
            pause
        end
        close figure 1

         fr0 = input('When does the flow begin?  ');
        % fr0 = 2;
        fr1 = input('At which frame would you like to begin analysis?  ');
    else
        fr0 = 2;
        fr1 = form{2*C+1,end-10};
    end

    % If not specified in Excel File, determine when analysis should end
    if isnan(form{2*C+1,end-8})
        if track == 2
            framescan2 = floor(numfr(1)/10);
            if sk == 0
                mov1 = aviread(fname{nvid},movinfo{nvid}.NumFrames-
framescan2:movinfo{nvid}.NumFrames);
            else
                mov1sk = aviread(fname{nvid},movinfo{nvid}.NumFrames-
framescan2:movinfo{nvid}.NumFrames);
```

```
        structsz = max(size(mov1sk));
        sz = size(mov1sk(1).cdata);
        mov1 = struct('cdata',zeros(sz(1)-1,sz(2)-1,sz(3)));
        for skframe = 1:structsz
          for i = 1:sz(1)-1
            sz1 = size(mov1sk(skframe).cdata(i+1,key(i+1):end,:));
            sz2 = size(mov1sk(skframe).cdata(i,1:key(i)-1,:));

            ln(i) = sz1(2) + sz2(2);
            if ln(i) == sz(2)-1
              mov1(skframe).cdata(i,:,:) =
double([mov1sk(skframe).cdata(i+1,key(i+1):end,:) mov1sk(skframe).cdata(i,1:key(i)-1,:)])/255;
            else
              mov1(skframe).cdata(i,:,:) =
double([mov1sk(skframe).cdata(i+1,key(i+1)+1:end,:) mov1sk(skframe).cdata(i,1:key(i)-
1,:)])/255;
            end
          end
        end

        figure(1)
        for fr = 1:framescan2
```

```
            image(imlincomb(brtscl,mov1(fr).cdata))
            colormap(gray)
            if nvid > 1
               text(50,50,num2str(fr+sumnumfr(nvid-1)+movinfo{nvid}.NumFrames-
framescan2),'Color',[0 1 0])
            else
               text(50,50,num2str(fr+movinfo{nvid}.NumFrames-framescan2),'Color',[0 1 0])
            end
            pause
         end
         close figure 1

         frb = input('When does the jump break up?  ');
      else
         frb = numfr(1);
      end
   else
      frb = form{2*C+1,end-8};
   end

   % Determine total number of frames
   frf = numfr(1);
   if nvid > 1
```

```
    numfr(1) = numfr(1)-fr1;
    numfr(nvid) = frf-sumnumfr(nvid-1);
    for i = 1:nvid
        sumnumfr(i) = sum(numfr(1:i));
    end
else
    numfr(nvid) = frf-fr1;
    sumnumfr(nvid) = numfr(nvid);
end

 % Determine downstream depth associated with each frame
Hframe = @(frame) (hf-hi)/(frf-fr0)*(frame-fr0) + hi;
uH = linspace(hi,hf,floor(sumnumfr(nvid)+fr1));

 % Initialize variables
xlmeanabs = zeros(floor(sumnumfr(nvid)/skprt),1);
xrmeanabs = xlmeanabs;
xlabs = xlmeanabs;
xrabs = xlmeanabs;
labsI = xlabs;
rabsI = labsI;
dabs = labsI;
dI = dabs;
```

```
dmean = dI;

% Initialize trip points and indices
endtrip = 0;
newpointtrip = 0;
fr = 0;

% Begin Frame Analyses
while fr < frb/skprt+1-fr1
   fr = fr + 1;
   frs = fr*skprt-(skprt-1);
   frsc(fr) = frs+fr1-1;
   % Load frames
   if frs <= numfr(1)-floor(frmavg/2)
      if sk == 0
         mov1 = aviread(fname{1},frs-ceil(frmavg/2)+fr1:frs+floor(frmavg/2)-1+fr1);
      else
         mov1sk = aviread(fname{1},frs-ceil(frmavg/2)+fr1:frs+floor(frmavg/2)-1+fr1);
         structsz = max(size(mov1sk));
         sz = size(mov1sk(1).cdata);
         mov1 = struct('cdata',zeros(sz(1)-1,sz(2)-1,sz(3)));
         for skframe = 1:structsz
            for i = 1:sz(1)-1
```

```
                    sz1 = size(mov1sk(skframe).cdata(i+1,key(i+1):end,:));
                    sz2 = size(mov1sk(skframe).cdata(i,1:key(i)-1,:));

                    ln(i) = sz1(2) + sz2(2);
                    if ln(i) == sz(2)-1
                       mov1(skframe).cdata(i,:,:) =
double([mov1sk(skframe).cdata(i+1,key(i+1):end,:) mov1sk(skframe).cdata(i,1:key(i)-1,:)])/255;
                    else
                       mov1(skframe).cdata(i,:,:) =
double([mov1sk(skframe).cdata(i+1,key(i+1)+1:end,:) mov1sk(skframe).cdata(i,1:key(i)-
1,:)])/255;
                    end
                 end
              end
           else
              if sk == 0
                 mov1 = aviread(fname{1},numfr(1)-frmavg+1:numfr(1));
              else
                 mov1sk = aviread(fname{1},numfr(1)-frmavg+1:numfr(1));
                 structsz = max(size(mov1sk));
                 sz = size(mov1sk(1).cdata);
                 mov1 = struct('cdata',zeros(sz(1)-1,sz(2)-1,sz(3)));
```

```
            for skframe = 1:structsz
                for i = 1:sz(1)-1
                    sz1 = size(mov1sk(skframe).cdata(i+1,key(i+1):end,:));
                    sz2 = size(mov1sk(skframe).cdata(i,1:key(i)-1,:));

                    ln(i) = sz1(2) + sz2(2);
                    if ln(i) == sz(2)-1
                        mov1(skframe).cdata(i,:,:) =
double([mov1sk(skframe).cdata(i+1,key(i+1):end,:) mov1sk(skframe).cdata(i,1:key(i)-1,:)])/255;
                    else
                        mov1(skframe).cdata(i,:,:) =
double([mov1sk(skframe).cdata(i+1,key(i+1)+1:end,:) mov1sk(skframe).cdata(i,1:key(i)-
1,:)])/255;
                    end
                end
            end
        end

        % Analyze First Frame, average if applicable
        % Note: If you choose to pick new points at any point in the analysis,
        % the program will return to this routine within the loop
        if fr == 1 || newpointtrip == 1;
```

```
scrsz = get(0,'ScreenSize');
figure('Position',[1 0 scrsz(3) scrsz(4)])
if frmavg == 1
   movcomb = imlincomb(brtscl/frmavg,mov1(1).cdata);
elseif frmavg == 3
   movcomb =
imlincomb(brtscl/frmavg,mov1(1).cdata,brtscl/frmavg,mov1(2).cdata,brtscl/frmavg,mov1(3).cda
ta);
elseif frmavg == 5
   movcomb =
imlincomb(brtscl/frmavg,mov1(1).cdata,brtscl/frmavg,mov1(2).cdata,brtscl/frmavg,mov1(3).cda
ta,brtscl/frmavg,mov1(4).cdata,brtscl/frmavg,mov1(5).cdata);
elseif frmavg == 7
   movcomb =
imlincomb(brtscl/frmavg,mov1(1).cdata,brtscl/frmavg,mov1(2).cdata,brtscl/frmavg,mov1(3).cda
ta,brtscl/frmavg,mov1(4).cdata,brtscl/frmavg,mov1(5).cdata,brtscl/frmavg,mov1(6).cdata,brtscl/f
rmavg,mov1(7).cdata);
elseif frmavg == 9
   movcomb =
imlincomb(brtscl/frmavg,mov1(1).cdata,brtscl/frmavg,mov1(2).cdata,brtscl/frmavg,mov1(3).cda
ta,brtscl/frmavg,mov1(4).cdata,brtscl/frmavg,mov1(5).cdata,brtscl/frmavg,mov1(6).cdata,brtscl/f
rmavg,mov1(7).cdata,brtscl/frmavg,mov1(8).cdata,brtscl/frmavg,mov1(9).cdata);
elseif frmavg == 11
```

```
        movcomb =
imlincomb(brtscl/frmavg,mov1(1).cdata,brtscl/frmavg,mov1(2).cdata,brtscl/frmavg,mov1(3).cda
ta,brtscl/frmavg,mov1(4).cdata,brtscl/frmavg,mov1(5).cdata,brtscl/frmavg,mov1(6).cdata,brtscl/f
rmavg,mov1(7).cdata,brtscl/frmavg,mov1(8).cdata,brtscl/frmavg,mov1(9).cdata,brtscl/frmavg,m
ov1(10).cdata,brtscl/frmavg,mov1(11).cdata);
        end


        imgsize = size(movcomb);


        % Show image, select Jet, Left Jump, Right Jump, and Upper Left, Lower Right of
the ceiling selecting window
        % Jet and ceiling window are only selected on the first frame, not when you repick
points
        image(movcomb)
        colormap(gray)
        if fr == 1
           [jety,jetx] = ginput(1);
        end
        [lefty,leftx] = ginput(1);
        [righty,rightx] = ginput(1);
        if fr == 1 && ceiling ~= 0
           [wetly,wetlx] = ginput(1);
           [wetry,wetrx] = ginput(1);
```

```
end
newpointtrip = 0;
close figure 1

% Convert Image to Double
movd = double(movcomb);

% Calculate brightness value at selected jump locations
leftI = mean(movd(round(leftx)-2:round(leftx)+2,round(lefty)));
rightI = mean(movd(round(rightx)-2:round(rightx)+2,round(righty)));

% Determine the size of the search window
range = round(mean([jety-lefty righty-jety])*rngsz);

% If you have chosen a light ceiling, this average the light values
% in the window you selected, and determine the maximum brightness
% value
if ceiling ~= 0
   swatch = movd(round(wetlx):round(wetrx),round(wetly):round(wetry));
   maxbrt = (1+ceiling)*mean(mean(swatch));
end
```

```
            movrow = squeeze(movd(round(jetx)-
floor(bandwid/2):round(jetx)+floor(bandwid/2),:,:));        % Band of data along the jet,
"bandwid"
            movrow1 = mean(movrow(:,:,1));                                    % Light
values across movrow averaged across bandwid
            if ceiling ~= 0
               movrow1(movrow1 > maxbrt) = maxbrt;
            end
            diffmr1 = diff(movrow1);                                    % Derivative of
movrow1
            mvavg = tsmovavg(diffmr1, 's', swid);                        % Moving
Average of diffmr1
            mvavg = [nan(1,floor(swid/2)) mvavg(swid:end) nan(1,floor(swid/2))];
            movsav(fr,:) = movrow1;
            meansav(fr,:) = mvavg;



            % Create search window for left and right jump locations
            if round(lefty) <= range
               movrowl = movrow1(1:round(lefty)+range);                    %
Threshold Criterion
               diffl = diffmr1(1:round(lefty)+range-1);                    % Derivative
Criterion
```

```
    meandl = mvavg(1:round(lefty)+range-1);                    % Mean
Derivative Criterion
  else
    movrowl = movrow1(round(lefty)-range:round(lefty)+range);
    diffl = diffmr1(round(lefty)-range:round(lefty)+range-1);
    meandl = mvavg(round(lefty)-range:round(lefty)+range-1);
  end
  if imgsize(2)- round(righty) <= range
    movrowr = movrow1(round(righty)-range:end);
    diffr = diffmr1(round(righty)-range:end);
    meandr = mvavg(round(righty)-range:end);
  else
    movrowr = movrow1(round(righty)-range:round(righty)+range);
    diffr = diffmr1(round(righty)-range:round(righty)+range-1);
    meandr = mvavg(round(righty)-range:round(righty)+range-1);
  end

  % Search (Inside out) for when the darkness threshold is broken
  rtrip = 0;
  ltrip = 0;
  for i = 2:length(movrowl)
    if movrowl(end+1-i) < leftI && ltrip == 0
      ltrip = 1;
```

```
        lImin = length(movrowl)+1-i;
        lImax = length(movrowl)+2-i;
        if movrowl(lImin) == movrowl(lImax)
            lI = mean([lImin lImax]);
        else
            lI = interp1(movrowl([lImin lImax]),[lImin lImax],leftI);
        end
    end
end
for i = 1:length(movrowr)
    if movrowr(i) < rightI && rtrip == 0
        rtrip = 1;
        rImax = i;
        rImin = i-1;
        if movrowr(rImin) == movrowr(rImax)
            rI = mean([rImin rImax]);
        else
            rI = interp1(movrowr([rImin rImax]),[rImin rImax],rightI);
        end
    end
end

lx = 1:length(diffl);
```

```
rx = 1:length(diffr);


% Find maximum derivative
xlmean = min(lx(meandl==max(meandl))+floor(swid/2));
xrmean = min(rx(meandr==min(meandr))+floor(swid/2));
xl = min(lx(diffl == max(diffl)));
xr = min(rx(diffr == min(diffr)));


% Convert transition points to global coordinates (movrow1), and
% save to a vector containing data from all frames analyzed
if round(lefty) <= range
   labsI(fr) = lI;
   xlmeanabs(fr) = xlmean;
   xlabs(fr) = xl;
else
   labsI(fr) = lI-range+round(lefty);
   xlmeanabs(fr) =xlmean-range+round(lefty);
   xlabs(fr) = xl-range+round(lefty);
end
rabsI(fr) = rI-range+round(righty);
xrmeanabs(fr) =xrmean-range+round(righty);
xrabs(fr) = xr-range+round(righty);
```

```
% Calculate jump diameter from data
dabs(fr) = xrabs(fr)-xlabs(fr);
dmean(fr) = xrmeanabs(fr)-xlmeanabs(fr);
dI(fr) = rabsI(fr) - labsI(fr);



% Calculate mean jump diameter based on all three criteria
dtot(fr) = mean([dmean(fr) dabs(fr) dI(fr)]);

% Calculate RMS of the data in the last five frames. If it varies
% excessively from the average RMS of the whole process, then
% give the option of repicking points
if fr > 5
   tadtot(fr) = mean(dtot(fr-4:fr));
   if fr > 10
      Dtadtot(fr) = tadtot(fr)-tadtot(fr-5);
   end
   if fr > 50
      DtadtotRMS(fr) = sqrt(mean(Dtadtot(fr-4:fr).^2));
      mnDtadtotRMS(fr) = mean(DtadtotRMS(10:end-10));
      if DtadtotRMS(fr) > 25*mnDtadtotRMS(fr)
         resetstr = input('The edge may be lost. Would you like to pick new points?
','s');
```

```
                    if strcmp(resetstr,'y') || strcmp(resetstr,'Y') || strcmp(resetstr,'Yes') ||
strcmp(resetstr,'yes')
                        newpointtrip = 1;
                    end
                end
            end
        end

        % Plot results of the analysis of this frame
        figure(3)
        plot(movrow1)
        hold on
        plot(diffl,'r')
        plot(xl,movrowl(floor(xl)),'x')
        plot(ones(length(movrowl))*leftI)
        plot(lI,leftI,'.r')
        plot(diffr,'r')
        plot(xr,movrowr(floor(xr)),'x')
        plot(ones(length(movrowl))*rightI)
        plot(rI,rightI,'.r')

        figure(4)
        plot(movrowr)
```

```
hold on

plot(diffr,'r')

plot(xr,movrowr(floor(xr)),'x')

plot(ones(length(movrowl))*rightI)

plot(rI,rightI,'.r')


% figure(5)

% plot(meandl)

%

% figure(6)

% plot(meandr)


figure(1)

image(mov1(1).cdata)

hold on

plot(xlmeanabs(fr),jetx,'xg')

plot(xrmeanabs(fr),jetx,'xg')

plot(jety,jetx,'or')

plot(xlabs(fr),jetx,'ob')

plot(xrabs(fr),jetx,'ob')

plot(labsI(fr),jetx,'r.')

plot(rabsI(fr),jetx,'r.')

if fr == 1
```

```
            dabs = zeros(length(mov1),1);
            dmean = dabs;
        end

        dabs(fr) = xrabs(fr)-xlabs(fr);
        dmean(fr) = xrmeanabs(fr)-xlmeanabs(fr);

        pause
        close figure 1 figure 3 figure 4
    else
    % Automatic analysis of frames on which you are not prompted to pick
    % points manually
    clc;
        % Average frames if applicable
        if frmavg == 1
            movcomb = imlincomb(brtscl/frmavg,mov1(1).cdata);
        elseif frmavg == 3
            movcomb =
imlincomb(brtscl/frmavg,mov1(1).cdata,brtscl/frmavg,mov1(2).cdata,brtscl/frmavg,mov1(3).cda
ta);
        elseif frmavg == 5
```

```
            movcomb =
imlincomb(brtscl/frmavg,mov1(1).cdata,brtscl/frmavg,mov1(2).cdata,brtscl/frmavg,mov1(3).cda
ta,brtscl/frmavg,mov1(4).cdata,brtscl/frmavg,mov1(5).cdata);
        elseif frmavg == 7
            movcomb =
imlincomb(brtscl/frmavg,mov1(1).cdata,brtscl/frmavg,mov1(2).cdata,brtscl/frmavg,mov1(3).cda
ta,brtscl/frmavg,mov1(4).cdata,brtscl/frmavg,mov1(5).cdata,brtscl/frmavg,mov1(6).cdata,brtscl/f
rmavg,mov1(7).cdata);
        elseif frmavg == 9
            movcomb =
imlincomb(brtscl/frmavg,mov1(1).cdata,brtscl/frmavg,mov1(2).cdata,brtscl/frmavg,mov1(3).cda
ta,brtscl/frmavg,mov1(4).cdata,brtscl/frmavg,mov1(5).cdata,brtscl/frmavg,mov1(6).cdata,brtscl/f
rmavg,mov1(7).cdata,brtscl/frmavg,mov1(8).cdata,brtscl/frmavg,mov1(9).cdata);
        elseif frmavg == 11
            movcomb =
imlincomb(brtscl/frmavg,mov1(1).cdata,brtscl/frmavg,mov1(2).cdata,brtscl/frmavg,mov1(3).cda
ta,brtscl/frmavg,mov1(4).cdata,brtscl/frmavg,mov1(5).cdata,brtscl/frmavg,mov1(6).cdata,brtscl/f
rmavg,mov1(7).cdata,brtscl/frmavg,mov1(8).cdata,brtscl/frmavg,mov1(9).cdata,brtscl/frmavg,m
ov1(10).cdata,brtscl/frmavg,mov1(11).cdata);
        end

        % Determine new search window center
        if fr < TW+2
```

```
        FR = 1:fr-1;
    else
        FR = fr-TW:fr-1;
    end
    if track == 1
        lefty = mean(labsI(FR));
        righty = mean(rabsI(FR));
    else
        lefty = mean(xlmeanabs(FR));
        righty = mean(xrmeanabs(FR));
    end

    movd = double(movcomb);                %Convert Image to Double

    % Determine the size of the search window
    range = round(mean([jety-lefty righty-jety])*rngsz);

    movrow = squeeze(movd(round(jetx)-
floor(bandwid/2):round(jetx)+floor(bandwid/2),:,:));        % Band of data along the jet,
"bandwid"
    movrow1 = mean(movrow(:,:,1));                                    % Light
values across movrow averaged across bandwid
```

```
% If you have chosen a light ceiling, this average the light values
% in the window you selected, and determine the maximum brightness
% value
if ceiling ~= 0
   movrow1(movrow1 > maxbrt) = maxbrt;
end



diffmr1 = diff(movrow1);                                % Derivative of
movrow1
mvavg = tsmovavg(diffmr1, 's', swid);                   % Moving Average
of diffmr1
mvavg = [nan(1,floor(swid/2)) mvavg(swid:end) nan(1,floor(swid/2))];
movsav(fr,:) = movrow1;
meansav(fr,:) = mvavg;

if round(lefty) <= range
   movrowl = movrow1(1:round(lefty)+range);             % Threshold
Criterion
   diffl = diffmr1(1:round(lefty)+range-1);             % Derivative
Criterion
   meandl = mvavg(1:round(lefty)+range-1);              % Mean
Derivative Criterion
```

```
else
    movrowl = movrow1(round(lefty)-range:round(lefty)+range);
    diffl = diffmr1(round(lefty)-range:round(lefty)+range-1);
    meandl = mvavg(round(lefty)-range:round(lefty)+range-1);
end
if imgsize(2)- round(righty) <= range
    movrowr = movrow1(round(righty)-range:end);
    diffr = diffmr1(round(righty)-range:end);
    meandr = mvavg(round(righty)-range:end);
else
    movrowr = movrow1(round(righty)-range:round(righty)+range);
    diffr = diffmr1(round(righty)-range:round(righty)+range-1);
    meandr = mvavg(round(righty)-range:round(righty)+range-1);
end

% Search (Inside out) for when the darkness threshold is broken
rtrip = 0;
ltrip = 0;
for i = 1:length(movrowl)
    if movrowl(end+1-i) < leftI && ltrip == 0
        ltrip = 1;
        lImin = length(movrowl)+1-i;
        lImax = length(movrowl)+2-i;
```

```
                % If Brightness Threshold is never crossed, offer to
                % terminate analysis
                if lImax > length(movrowl)
                    image(movcomb)
                    colormap(gray)
                    1
                    tripstr = input('An error may have occurred. Would you like to terminate
analysis? If no, pick new points','s');
                    if strcmp(tripstr,'y') || strcmp(tripstr,'Y') || strcmp(tripstr,'Yes') ||
strcmp(tripstr,'yes')
                        endtrip = 1;
                        strcat(num2str(fr),'/',num2str(frb));
                        finstr = 'n';
                        break
                    else
                        figure(9)
                        if track == 1
                            plot(dabs)
                        else
                            plot(dmean)
                        end
                        resetstr = 'y'
```

```
                    if strcmp(resetstr,'y') || strcmp(resetstr,'Y') || strcmp(resetstr,'Yes') ||
strcmp(resetstr,'yes')
                        newpointtrip = 1;
                        fro = input('At what frame would you like to start the analysis?');
                        if ~isempty(fro)
                            fr = fro;
                        end
                    end
                    close figure 9
                end
            else
                newpointtrip = 0;
            end
            if endtrip == 1 || newpointtrip == 1
                break
            end
            if movrowl(lImin) == movrowl(lImax)
                lI = mean([lImin lImax]);
            else
                lI = interp1(movrowl([lImin lImax]),[lImin lImax],leftI);
            end
        end
        if endtrip == 1 || newpointtrip == 1
```

```
            break
        end
    end
    if endtrip == 1 %|| newpointtrip == 1
        break
    end
    for i = 1:length(movrowr)
        if movrowr(i) < rightI && rtrip == 0
            rtrip = 1;
            rImax = i;
            rImin = i-1;
            if rImin == 0
                image(movcomb)
                colormap(gray)
                2
                tripstr = input('An error may have occurred. Would you like to terminate
analysis? If no, select new points','s');
                if strcmp(tripstr,'y') || strcmp(tripstr,'Y') || strcmp(tripstr,'Yes') ||
strcmp(tripstr,'yes')
                    endtrip = 1;
                    strcat(num2str(fr),'/',num2str(frb));
                    finstr = 'n';
                    break
```

```
                else
                    figure(9)
                    if track == 1
                        plot(dabs)
                    else
                        plot(dmean)
                    end
                    resetstr = 'y'
                    if strcmp(resetstr,'y') || strcmp(resetstr,'Y') || strcmp(resetstr,'Yes') ||
strcmp(resetstr,'yes')
                        newpointtrip = 1;
                        fro = input('At what frame would you like to start the analysis?');
                        if ~isempty(fro)
                            fr = fro;
                        end
                    end
                    close figure 9
                end
            else
                newpointtrip = 0;
            end
            if endtrip == 1 || newpointtrip == 1
                break
```

```
        end
        if movrowr(rImin) == movrowr(rImax)
            rI = mean([rImin rImax]);
        else
            rI = interp1(movrowr([rImin rImax]),[rImin rImax],rightI);
        end
    end
    if endtrip == 1 || newpointtrip == 1
        break
    end
end
if endtrip == 1 %|| newpointtrip == 1
    break
end

% Find maximum derivative
lx = 1:length(diffl);
rx = 1:length(diffr);

xlmean = min(lx(meandl==max(meandl))+floor(swid/2));
xrmean = min(rx(meandr==min(meandr))+floor(swid/2));
xl = min(lx(diffl == max(diffl)));
xr = min(rx(diffr == min(diffr)));
```

```
 % Convert transition points to global coordinates (movrow1), and
% save to a vector containing data from all frames analyzed
if round(lefty) <= range
    labsI(fr) = lI;
    xlmeanabs(fr) = xlmean;
    xlabs(fr) = xl;
else
    labsI(fr) = lI-range+round(lefty);
    xlmeanabs(fr) =xlmean-range+round(lefty);
    xlabs(fr) = xl-range+round(lefty);
end
rabsI(fr) = rI-range+round(righty);
xrmeanabs(fr) =xrmean-range+round(righty);
xrabs(fr) = xr-range+round(righty);

% Calculate jump diameter from data
dabs(fr) = xrabs(fr)-xlabs(fr);
dmean(fr) = xrmeanabs(fr)-xlmeanabs(fr);
dI(fr) = rabsI(fr) - labsI(fr);

dtot(fr) = mean([dmean(fr) dabs(fr) dI(fr)]);
```

```
% Calculate RMS of the data in the last five frames. If it varies
% excessively from the average RMS of the whole process, then
% give the option of repicking points
if fr > 5
   tadtot(fr) = mean(dtot(fr-4:fr));
   if fr > 10
      Dtadtot(fr) = tadtot(fr)-tadtot(fr-5);
   end
   if fr > 50
      DtadtotRMS(fr) = sqrt(mean(Dtadtot(fr-4:fr).^2));
      mnDtadtotRMS(fr) = mean(DtadtotRMS(10:end-10));
      if DtadtotRMS(fr) > 25*mnDtadtotRMS(fr)
         figure(9)
         if track == 1
            plot(dabs)
         else
            plot(dmean)
         end
         resetstr = input('Would you like to pick new points?','s')
         if strcmp(resetstr,'y') || strcmp(resetstr,'Y') || strcmp(resetstr,'Yes') ||
strcmp(resetstr,'yes')
            newpointtrip = 1;
            fro = input('At what frame would you like to start the analysis?');
```

```
            if ~isempty(fro)
                fr = fro;
            end
        end
        close figure 9
    end
  end
end

% Plot results every five frames
if mod(fr,5)==0
  figure(2)
  image(movcomb)
  colormap(gray)
  hold on
  plot(xlmeanabs(fr),jetx,'xg')
  plot(xrmeanabs(fr),jetx,'xg')
  plot(jety,jetx,'or')
  plot(xlabs(fr),jetx,'ob')
  plot(xrabs(fr),jetx,'ob')
  plot(labsI(fr),jetx,'.r')
  plot(rabsI(fr),jetx,'.r')
  text(5,5,num2str(fr),'Color',[0 1 0])
```

```
            end
        end
        if endtrip == 1
            break
        end
        if numfr(1)/skprt+1 - fr < 1
            1;
        end
    end

    %%
    % Eliminate frames in the height vector that weren't analyzed
    H = uH(ismember(1:length(uH)+fr1,frsc));
    % H = uH(20:end);
    if exist('finstr','var') && (strcmp(finstr,'y') || strcmp(finstr,'Y') || strcmp(finstr,'Yes') ||
strcmp(finstr,'yes'))
        Hend = uH(ismember(1:length(uH),frscend-fr1));
    end

    % Show Final Frame
    figure(2)
    image(movcomb)
    hold on
```

```
plot(xlmeanabs(fr-1),jetx,'xg')
plot(xrmeanabs(fr-1),jetx,'xg')
plot(jety,jetx,'or')
plot(xlabs(fr-1),jetx,'ob')
plot(xrabs(fr-1),jetx,'ob')
plot(labsI(fr-1),jetx,'.r')
plot(rabsI(fr-1),jetx,'.r')

% Calculate diameter measurements
dabs = xrabs-xlabs;
dmean = xrmeanabs-xlmeanabs;
dI = rabsI - labsI;
if exist('finstr','var') && (strcmp(finstr,'y') || strcmp(finstr,'Y') || strcmp(finstr,'Yes') ||
strcmp(finstr,'yes'))
    dend = abs(lend-rend);
end

% Create time vector (time stamp for each frame)
t = 1:fr-1;
t = t/framerate;

% Trim Diameter Measurements
dabs = dabs(1:fr-1);
```

```
dmean = dmean(1:fr-1);
dI = dI(1:fr-1);
H = H(1:fr-1);

% Plot Results
figure(3)
plot(H,dabs)
hold on
plot(H,dmean,'g')
plot(H,dI,'r')
if exist('finstr','var') && (strcmp(finstr,'y') || strcmp(finstr,'Y') || strcmp(finstr,'Yes') ||
strcmp(finstr,'yes'))
   plot(Hend,dend,'k')
end
text((max(t)-min(t))/5+min(t),(max(dI)-min(dI))/5+min(dI),strcat('Duration:
',num2str(t(end)),' s'))

% Select which criterion to use
sprintf('(1)Red: Brightness    (2)Green: Mean Differential   (3)Blue: Differential')
EdgeSelect = input('Please enter which curve you would like to use:  ');
if EdgeSelect == 2
   dI = dmean;
elseif EdgeSelect == 3
```

```
    dI = dabs;
end

% Calculate Moving Average
N = 51;                 % N must be odd
dIma = zeros(1,length(dI));

for i = 1:length(dI)
    if i < (N+1)/2
        dIma(i) = mean(dI(1:2*i-1));
    elseif i > length(dI)-(N-1)/2
        dIma(i) = mean(dI(end-(length(dI)-i)*2:end));
    else
        dIma(i) = mean(dI(i-(N-1)/2:i+(N-1)/2));
    end
end

dImaT = dIma((N+1)/2:end-(N-1)/2);          %Truncated Moving Average

% Plot final results
axis tight
set(gca,'nextplot','replacechildren');
figure(8)
```

```
plot(H,dI)
hold on
plot(H,dIma,'k')
text(5,5,strcat('Duration: ',num2str(t(end)),' s'))

% Record Results
RECORD = input('Would you like to Record this Information?  ','s');

if strcmp(RECORD,'y') || strcmp(RECORD,'Yes') || strcmp(RECORD,'yes') ||
strcmp(RECORD,'Y')
    if isnan(curvename)
        FNM = input('What would you like to call the file?  ','s');
    else
        FNM = curvename;
    end
    OUT{1,1} = We;
    OUT{2,1} = Re;
    OUT{3,1} = Djet;
    OUT{4,1} = needle;
    OUT{5,1} = framerate;
    OUT{1,2} = [t;H;dI';dIma;N*ones(1,length(t))];
    save(FNM,'OUT')
end
```

B.3 Script for Calibration and Combining Individual Experiments

```
clc; close all; clear all;
% Define colors to be used in plots
style = {'b','r','g','c','m','y','k'};

% Define file names to be used
calcon = 'CalibrationConstant';
calconl = strcat(calcon,'.mat');
xlsname = 'datacatalog.xls';


% Read in Data, Define parameters
[~,~,form] = xlsread(xlsname,-1);
formsz = size(form);
ncurves = (formsz(1)-4)/5+1;
wC = 2;                          % Calibration Pixel Uncertainty
wM = 4;                          % Measurement Pixel Uncertainty

% If calibration has already been performed, load calibration constants
if exist(calconl) ~= 0
   load(calcon)
   cal = CALOUT.cal;
   calunc = CALOUT.calunc;
```

```
    duncmax = CALOUT.duncmax;
    dunc = CALOUT.dunc;
    xrs = CALOUT.xrs;
    xls = CALOUT.xls;
    measx = CALOUT.measx;
    winsz = CALOUT.winsz;
    dx = CALOUT.dx;
end

% Load Data Repository
FNM2 = 'C:\Users\Michael\Dropbox\Research (1)\Results';
load(FNM2);
FNM2 = 'C:\Users\Michael\Dropbox\Research (1)\Resultsn';

% Determine whether both longitudinal and transverse data will be analyzed
for i = 1:formsz(1);
        if ~isnan(form{i,end})
            longtransnum = 1;
        else
            longtransnum = 0;
        end
end
if longtransnum == 2*ncurves;
```

```
    patt = 1;
else
    patt = 0;
end
if ~exist(calconl)
    cal = zeros(patt+1,ncurves);
end
Hrdcomb = cell(patt+1,1);

% Step through calibration images for curves to be analyzed
m = 0;
for C = 1:patt+1                                    %C = 1 is the set of curves in the
Longitudinal Cells of the Excel File while C = 2 is in the Transverse Cells
    Dunc{C} = [];
    for n = 1:ncurves                               %n is the experiment number being
analyzed
        % Extract File Names From Excel Sheet
        curvename{C}{n} = form{2*C+5*n-6,end};
        calname{C}{n} = form{2*C+5*n-5,end-2};
        vidtyp(C,n) = form{2*C+5*n-6,end-3};
        % Convert from pixels to mm
        if exist(calconl) == 0
            left = imread(char(calname{C}{n}),'bmp');
```

```
right = imread(char(calname{C}{n}),'bmp');
winsz = size(left);
brtrip = 0;
brtscl = 1;
% Adjust image brightness
while brtrip == 0
   image(imlincomb(brtscl,left))
   colormap(gray)
   brtstr = input('Is the brightness acceptable?','s');
   if strcmp(brtstr,'y') || strcmp(brtstr,'Y') || strcmp(brtstr,'Yes') ||
strcmp(brtstr,'yes')
      brtrip = 1;
   else
      brtscl = input('Enter a new scaling factor: ');
   end
end

% Display image and select points on the ruler
scrsz = get(0,'ScreenSize');
figure('Position',[1 0 scrsz(3) scrsz(4)])
image(imlincomb(brtscl,left))
colormap(gray)
axis off
```

```
[xl,yl] = ginput(1);
close figure 1

scrsz = get(0,'ScreenSize');
figure('Position',[1 0 scrsz(3) scrsz(4)])
image(imlincomb(brtscl,right))
colormap(gray)
axis off
[xr,yr] = ginput(1);
close figure 1

% Find out what distance was measured
measx(C,n) = input('What distance did you measure (mm)?    ')
dx = abs(xr-xl);
calunc(C,n) = 1/(xr^2-(2*xr*xl)+xl^2);

% Calculate calibration constant
if vidtyp(C,n)==1
   cal(C,n) = measx(C,n)/dx;
else
   cal(C,n) = measx(C,n)*(72/64)/dx;
end
xrs(C,n) = xr;
```

```
        xls(C,n) = xl;
    end
end

% Load Curve
Hcomb{C} = [];
for i = 1:ncurves
    x{C}{i} = load(curvename{C}{i});
    x{C}{i} = x{C}{i}.OUT;
    H{C}{i} = abs(x{C}{i}{1,2}(2,:));
    Hcomb{C} = [Hcomb{C} H{C}{i}];
end
Hrddyncomb{C} = [];
for i = 1:ncurves
    t{C}{i} = x{C}{i}{1,2}(1,:);
    D{C}{i} = x{C}{i}{1,2}(3,:)*cal(C,i);
    M{C}{i} = x{C}{i}{1,2}(4,:)*cal(C,i);
    Hrd{C}{i} = round(H{C}{i}*100)/100;
    Hrdcomb{C} = [Hrdcomb{C} Hrd{C}{i}];

    %Uncertainty Analysis
    Dunci{C}{i} = (2*(D{C}{i}*measx(C,n)*wC*(calunc(C,n))).^2 +
2*(wM*cal(C,n))^2).^.5;
```

```
Dunc{C} = [Dunc{C} Dunci{C}{i}];

% Round H values to the nearest tenth of a mm
Hrddyn{C}{i} = round(H{C}{i}*10)/10;
Hrddyncomb{C} = [Hrddyncomb{C} Hrddyn{C}{i}];

% Uncertainty Calculation
sigd{C}{i} = (2*(measx(C,n)*wM/(xrs(C,n)-xls(C,n))).^2 +
2*(x{C}{i}{1,2}(3,:)*measx(C,n)*wC/(xrs(C,n)^2-2*xrs(C,n)*xls(C,n)+xls(C,n)^2)).^2).^.5;

% Plot Individual Curves
figure(2)
m = m+1;
h{m} = plot(H{C}{i},M{C}{i},style{i},'LineWidth',2)
hold on

ylabel('Jump Diameter')
xlabel('Jump Height')

figure(1)
plot(H{C}{i},D{C}{i})
hold on
ylabel('Jump Diameter')
```

```
        xlabel('Jump Height')
    end
    Duncmax(C) = max(Dunc{C});
end

% Save Calibration Data
CALOUT.cal = cal;
CALOUT.calunc = calunc;
CALOUT.duncmax = Duncmax;
CALOUT.dunc = Dunc;
CALOUT.xrs = xrs;
CALOUT.xls = xls;
CALOUT.measx = measx;
CALOUT.winsz = winsz;
CALOUT.dx = dx;
if exist(calconl) == 0
    save(calcon,'CALOUT')
else
    load(calcon)
    cal = CALOUT.cal;
    calunc = CALOUT.calunc;
    duncmax = CALOUT.duncmax;
    dunc = CALOUT.dunc;
```

```
    xrs = CALOUT.xrs;
    xls = CALOUT.xls;
    measx = CALOUT.measx;
    winsz = CALOUT.winsz;
    dx = CALOUT.dx;
  end
  %%
  for C = 1:patt+1
    % Create H bins at intervals of 0.1 mm into which all of the data will be sorted
    Hmin(C) = min(Hrdcomb{C});
    Hmax(C) = max(Hrdcomb{C});
    Hvec{C} = Hmin(C):.01:Hmax(C);
    Hmindyn(C) = min(Hrddyncomb{C});
    Hmaxdyn(C) = max(Hrddyncomb{C});

    Hvecdyn{C} = Hmindyn(C):.1:Hmaxdyn(C);

    % If one of the curves appears to be an outlier, throw it out
    sprintf('1:b 2:r 3:g 4:c 5:m 6:y 7:k')
    if C == 1
      Nex(C) = input('How many longitudinal/smooth curves would you like to throw
out?');
    else
```

```
    Nex(C) = input('How many transverse curves would you like to throw out?');
end
nex = cell(patt+1,1);
if Nex(C) > 0
    for n = 1:Nex(C)
        nex{C}(n) = input('Please state which curves you would like to throw out: ');
    end
end

% Sort all of the data into bins based on the H value
for d = 1:length(Hvec{C})
    Hb{C} = Hvec{C}(d);
    trip = 0;
    Hbin{C}{d} = [];
    tbin{C}{d} = [];
    Dbin{C}{d} = [];
    Mbin{C}{d} = [];
    Bindex{C}{d} = [];
    for i = 1:ncurves
        if ismember(i,nex{C})
        else
            Hrdbini{C}{i} = [];
            tbini{C}{i} = [];
```

```
        Dbini{C}{i} = [];
        Mbini{C}{i} = [];
        Bindexi{C}{i} = [];
        for w = 1:length(Hrd{C}{i})
           if Hrd{C}{i}(w) == Hb{C}
              Hrdbini{C}{i} = [Hrdbini{C}{i} Hrd{C}{i}(w)];
              tbini{C}{i} = [tbini{C}{i} t{C}{i}(w)];
              Dbini{C}{i} = [Dbini{C}{i} D{C}{i}(w)];
              Mbini{C}{i} = [Mbini{C}{i} M{C}{i}(w)];
              Bindexi{C}{i} = [Bindexi{C}{i} i];
           end

        end
        Hbin{C}{d} = [Hbin{C}{d} Hrdbini{C}{i}];
        tbin{C}{d} = [tbin{C}{d} tbini{C}{i}];
        Dbin{C}{d} = [Dbin{C}{d} Dbini{C}{i}];
        Mbin{C}{d} = [Mbin{C}{d} Mbini{C}{i}];
        Bindex{C}{d} = [Bindex{C}{d} Bindexi{C}{i}];
     end
  end
  Dmean{C}(d) = mean(Dbin{C}{d});
  Mmean{C}(d) = mean(Mbin{C}{d});
  statsz(C,d) = length(Hbin{C}{d});
```

```
end


for d = 1:length(Hvecdyn{C})
    Hbdyn{C} = Hvecdyn{C}(d);
    trip = 0;
    Hbindyn{C}{d} = [];
    tbindyn{C}{d} = [];
    Dbindyn{C}{d} = [];
    Mbindyn{C}{d} = [];
    Bindexdyn{C}{d} = [];
    for i = 1:ncurves
        if ~ismember(i,nex{C})
            Hrdbindyni{C}{i} = [];
            tbindyni{C}{i} = [];
            Dbindyni{C}{i} = [];
            Mbindyni{C}{i} = [];
            Bindexdyni{C}{i} = [];
            if C == 2
                1;
            end
            for w = 1:length(Hrddyn{C}{i})
                if round(100*Hrddyn{C}{i}(w))/100 == round(100*Hbdyn{C})/100
                    Hrdbindyni{C}{i} = [Hrdbindyni{C}{i} Hrddyn{C}{i}(w)];
```

```
                tbindyni{C}{i} = [tbindyni{C}{i} t{C}{i}(w)];
                Dbindyni{C}{i} = [Dbindyni{C}{i} D{C}{i}(w)];
                Mbindyni{C}{i} = [Mbindyni{C}{i} M{C}{i}(w)];
                Bindexdyni{C}{i} = [Bindexdyni{C}{i} i];
            end
        end
        Hbindyn{C}{d} = [Hbindyn{C}{d} Hrdbindyni{C}{i}];
        tbindyn{C}{d} = [tbindyn{C}{d} tbindyni{C}{i}];
        Dbindyn{C}{d} = [Dbindyn{C}{d} Dbindyni{C}{i}];
        Mbindyn{C}{d} = [Mbindyn{C}{d} Mbindyni{C}{i}];
        Bindexdyn{C}{d} = [Bindexdyn{C}{d} Bindexdyni{C}{i}];
    end
end
Dmeandyn{C}(d) = mean(Dbindyn{C}{d});
Mmeandyn{C}(d) = mean(Mbindyn{C}{d});
szdyn(C,d) = length(Hbindyn{C}{d});
Dsampuncdyn(C,d) = (sum((Mbindyn{C}{d}-
Mmeandyn{C}(d)).^2)/(nbindyn(C,d)-1))^.5/sqrt(nbindyn(C,d));
Duncdyn{C}(d) = (Dsampuncdyn(C,d)^2+Duncmax(C)^2)^.5;
end

Di = 1;
while Di < length(Hvec{C})
```

```
            if isnan(Dmean{C}(Di))
                Hvec{C} = [Hvec{C}(1:Di-1) Hvec{C}(Di+1:length(Hvec{C}))];
                Dmean{C} = [Dmean{C}(1:Di-1) Dmean{C}(Di+1:length(Dmean{C}))];
                Mmean{C} = [Mmean{C}(1:Di-1) Mmean{C}(Di+1:length(Mmean{C}))];
                Di = Di-1;
            end
            Di = Di+1;
        end
            Di = 1;
        while Di < length(Hvecdyn{C})
            if isnan(Dmeandyn{C}(Di))
                Hvecdyn{C} = [Hvecdyn{C}(1:Di-1) Hvecdyn{C}(Di+1:length(Hvecdyn{C}))];
                Dmeandyn{C} = [Dmeandyn{C}(1:Di-1)
Dmeandyn{C}(Di+1:length(Dmeandyn{C}))];
                Mmeandyn{C} = [Mmeandyn{C}(1:Di-1)
Mmeandyn{C}(Di+1:length(Mmeandyn{C}))];
                Duncdyn{C} = [Duncdyn{C}(1:Di-1) Duncdyn{C}(Di+1:length(Duncdyn{C}))];
                Di = Di-1;
            end
            Di = Di+1;
        end

        % Specify the maximum and minimum values of H to be averaged
```

```
L = input('What lower limit of data would you like to keep?  ');

U = input('What upper limit of data would you like to keep?  ');


% Trim off the data beyond the specified minimum and maxiumim H values

Dmean{C} = Dmean{C}(Hvec{C} >= L);

Mmean{C} = Mmean{C}(Hvec{C} >= L);

Hvec{C} = Hvec{C}(Hvec{C} >= L);


Dmean{C} = Dmean{C}(Hvec{C} <= U);

Mmean{C} = Mmean{C}(Hvec{C} <= U);

Hvec{C} = Hvec{C}(Hvec{C} <= U);


Dmeandyn{C} = Dmeandyn{C}(Hvecdyn{C} >= L);

Mmeandyn{C} = Mmeandyn{C}(Hvecdyn{C} >= L);

Hvecdyn{C} = Hvecdyn{C}(Hvecdyn{C} >= L);

Duncdyn{C} = Duncdyn{C}(Hvecdyn{C} >= L);


Dmeandyn{C} = Dmeandyn{C}(Hvecdyn{C} <= U);

Mmeandyn{C} = Mmeandyn{C}(Hvecdyn{C} <= U);

Hvecdyn{C} = Hvecdyn{C}(Hvecdyn{C} <= U);

Duncdyn{C} = Duncdyn{C}(Hvecdyn{C} <= U);


% Prepare information to be saved in the file and repository
```

```
We = [];
for i = 1:ncurves
   We = [We x{1}{i}{1,1}];
end
Re = x{C}{1}{2,1};
Djet = x{C}{1}{3,1};
Color = x{C}{1}{4,1};
Frate = x{C}{1}{5,1};
if ncurves == 4
   Leg2 = {strcat('1: We = ',num2str(We(1))) strcat('2: We = ',num2str(We(2)))
strcat('3: We = ',num2str(We(3))) strcat('4: We = ',num2str(We(4)))};
elseif ncurves == 3
   Leg2 = {strcat('1: We = ',num2str(We(1))) strcat('2: We = ',num2str(We(2)))
strcat('3: We = ',num2str(We(3)))};
elseif ncurves == 2
   Leg2 = {strcat('1: We = ',num2str(We(1))) strcat('2: We = ',num2str(We(2)))};
else
   Leg2 = {strcat('1: We = ',num2str(We(1)))};
end

% Plot and Print Results
figure(2)
hold on
```

```
    % for i = 1:ncurves
    %     plot(Hrd{C}{i},D{C}{i})
    % end
    plot(Hvec{C},Dmean{C},'k')
    plot(Hvec{C},Mmean{C},'g')
    plot(Hvecdyn{C},Dmeandyn{C},'r')
    ylabel('Jump Diameter')
    xlabel('Jump Height')
    legend(Leg2)
    set(gcf,'PaperPosition',[1 1 5 4])
    print('-dtiff','-r400','figure1.tif')

    figure(4)
    hold on
    % for i = 1:ncurves
    %     plot(Hrd{C}{i},D{C}{i})
    % end
    plot(Hvecdyn{C},Dmeandyn{C},'k')
    ylabel('Jump Diameter')
    xlabel('Jump Height')
    set(gcf,'PaperPosition',[1 1 5 4])
    print('-dtiff','-r400','figure2.tif')
end
```

```
if patt+1 > 1
    [Hintersect,ia,ib] = intersect(Hvecdyn{1},Hvecdyn{2});
    DlDt = Dmeandyn{1}(ia)./Dmeandyn{2}(ib);
end
%%

% Compile OUT File
for C = 1:patt+1
    OUT{1,2} = 'Number of Files:';
    OUT{1,3} = ncurves;
    OUT{2,2} = 'Weber Number:';
    OUT{2,3} = We;
    OUT{3,2} = 'Reynolds Number:';
    OUT{3,3} = Re;
    OUT{4,2} = 'Color';
    OUT{4,3} = Color;
    OUT{5,2} = 'Jet Diameter';
    OUT{5,3} = Djet;
    OUT{6,2} = 'Window Size';
    OUT{6,3} = winsz;
    OUT{7,2} = 'Physical Length';
    OUT{7,3} = measx;
    OUT{8,2} = 'Pixel Length';
```

```
        OUT{8,3} = dx;
        OUT{9,2} = 'Frame Rate (fps)';
        OUT{9,3} = Frate;

        for i = 1:ncurves
           OUT{i,1} = [Hrd{C}{i};D{C}{i}];
        end
        OUT{ncurves+1,1} = [Hvecdyn{C};Dmeandyn{C}];
        OUT{ncurves+2,1} = Duncdyn;
        OUT{ncurves+3,1} = [Dmeandyn{C}-
Duncdyn{C};Dmeandyn{C};Dmeandyn{C}+Duncdyn{C}];


        %
        if patt == 1
           if C == 1
              dir = 'long';
           else
              dir = 'trans';
           end
        end
        PATT = input('What is the surface condition?','s');
```

```
Wernd = round(mean(We)/100)*100;
if strcmp(PATT,'SmoothU') || strcmp(PATT,'smoothU')
   a = 1;
elseif strcmp(PATT,'50U')
   a = 2;
elseif strcmp(PATT,'80U')
   a = 3;
elseif strcmp(PATT,'90U')
   a = 4;
elseif strcmp(PATT,'50C')
   a = 5;
elseif strcmp(PATT,'80C')
   a = 6;
elseif strcmp(PATT,'90C')
   a = 7;
elseif strcmp(PATT,'SmoothC') || strcmp(PATT,'smoothC')
   a = 8;
elseif strcmp(PATT,'PostU') || strcmp(PATT,'postU')
   a = 9;
elseif strcmp(PATT,'PostC') || strcmp(PATT,'postC')
   a = 10;
end
```

```
if strcmp(Color,'blue') || strcmp(Color,'Blue')
    b = 1;
    if Wernd == 600
        c = 1;
    elseif Wernd == 900
        c = 2;
    elseif Wernd == 1200
        c = 3;
    elseif Wernd == 1500;
        c = 4;
    elseif Wernd == 1800;
        c = 5;
    end
elseif strcmp(Color,'purple') || strcmp(Color,'Purple')
    b = 2;
    if Wernd == 600
        c = 1;
    elseif Wernd == 900
        c = 2;
    elseif Wernd == 1200
        c = 3;
    elseif Wernd == 1500
        c = 4;
```

```
    elseif Wernd == 1800;
        c = 5;
    elseif Wernd == 2100;
        c = 6;
    end
end

DATA{a,b,c,C} = OUT;

% Determine the filename
if patt == 0
    FNM = strcat('We',num2str(Wernd),'_',Color,'_',PATT,'n');
else
    FNM = strcat('We',num2str(Wernd),'_',Color,'_',PATT,dir,'n');
end

% Save Files
save(FNM,'OUT');
save(FNM2,'DATA');
end
```